אוניברסיטת תל אביב

הפקולטה למדעים מדויקים ע"ש ריימונד ובברלי סאקלר

בית הספר לפיסיקה ואסטרונומיה

המחלקה לחומר מעובה

שילוב מהוד אופטי עם ספקטרומטר פורייה

חיבור זה מוגש כחלק מהדרישות לקבלת תואר 'מוסמך למדעים' באוניברסיטת תל אביב

על ידי

ערגה ליפשיץ

עבודה זו הוכנה בהנחיתו של

ד"ר חיים סוכובסקי

מאי 2018

Tel Aviv University

The Raymond and Beverly Sackler Faculty of Exact Sciences

School of Physics and Astronomy

Multipass FT-IR Spectrometer- Compact High Spectral Resolution

Thesis submitted in partial fulfillment of the requirements for M.Sc. at Tel-Aviv University

by

Erga Lifshitz

This work was carried out under the supervision of

Dr. Haim Suchowski

May 2018

Acknowledgements

I wish to express my deepest gratitude to my teacher and supervisor, Dr. Haim Suchowski, for his guidance and support during the course of this work.
I would like to express my very great appreciation to Dr. Assaf Levanon for guiding me in the technical aspects of this project.
I would like to thank the femto-nano group, for their friendship and support.
I would like to extend my special thanks to Dr. Sharly Fleischer's group and Prof. Shimshon Bar-Ad's group, for allowing me to use their equipment.
Finally, I am in debited to my family and partner, for their patience and support during the project.

Contents

תקציר

בעבודה זו אנו מציגים גישה חדשה לשיפור הרזולוציה הספקטרלית של ספקטרומטר פורייה (FT-IR) מבלי להגדיל את מימדיו. פיתחנו אלגוריתם חדש המשלב אינטרפרוגרמות שונות, שנדגמו בהפרשי מרחקים אופטיים שונים (OPD), אשר מייצר מהן אינטרפרוגרמה רציפה.

באופן זה הצלחנו להאריך את האינטרפרוגרמה המקורית ועל-ידי כך לשפר את הרזולוציה הספקטרלית של הספקטרומטר, מבלי להגדיל אותו. הדגמנו את הפתרון באמצעות שילוב מהוד אופטי מסוג תא הריוט עם FT-IR.

FT-IR הוא ספקטרומטר פורייה המבוסס על אינטרפרומטר מייקלסון בעל זרוע סורקת המייצרת אינטפרוגרמה ביחס לזרוע ייחוס. התקנו את המהוד האופטי מסוג תא הריוט בזרוע הייחוס, וביצענו שילוב אינטרפרוגרמות באמצעות אלגוריתם ההדבקה שפיתחנו.

תא הריוט הוא מהוד אופטי המבוסס על מראות קעורות ובעל אופני דרך מובהקים שאינם תלויים באופן ליניארי בגודל התא. במסגרת המחקר ביצענו גם חקירה תיאורטית, נומרית וניסויית של תא הריוט, כדי להבין האם וכיצד הוא יכול לשמש כזרוע ייחוס ל-FT-IR.

מצאנו משוואה תיאורטית המתארת את הקשר בין הדרך האופטית הנעשית בתא לבין גודל התא, ובדקנו אותה באמצעות סימולציה וניסוי. בנוסף, מצאנו כי תא הריוט משמר את גודל הקרן ואת המיקום שלה ביחס למערכת אופטית חיצונית, אבל לא משמר משרעת ופאזה.

הסימולציה והניסוי בוצעו באמצעות בניית מערכת הכוללת תא הריוט המשולב ב-FT-IR שבו מומשו אלגוריתם ההדבקה והמשוואה התיאורטית שפיתחנו . הניסויים הראשוניים של ההריוט FT-IR בוצעו עם מקור הליום-ניאון ומקור של 780 ננו-מטר של חברת טופטיקה. תוצאות הסימולציה הראו כי הרזולוציה הספקטרלית של המערכת (הריוט FT-IR) עוקבת אחר קו מגמה זהה ל-FT-IR רגיל. תוצאות הניסוי מלמדות שהריוט FT-IR יכול לשמש כחלופה ל-FT-IR סטנדרטי.

Abstract

We present a new approach to enhance the spectral resolution of a FT-IR spectrometer without increasing it's length. We developed a new algorithm for combining interferograms, sampled at different optical path differences (OPD's), to form a continues interferogram. Thus, effectively extend the length of the original interferogram. The multipass FT-IR is a FT-IR spectrometer based on a Michelson interferometer with one moving arm and one reference arm made of a multipass cell. This FT-IR employs our algorithm for combining the FT-IR interferograms, collected relative to a set of multipass cell modes. We demonstrated the multipass FT-IR with a Herriott cell as a multipass cell. The Herriott cell is a curved mirror resonator that has distinct OPD modes that non linearly depend on the size of the cell. We studied the Herriott cell theoretically, numerically and experimentally in order to understand whether it can serve as a set of references for the FT-IR. We found a theoretical formula that describe the relation between the OPD done in the cell and the cell size and compared it with a numerical simulation and experiment. Additionally, we found that the Herriott cell conserve a beam's size and alignment with relation to an outside optical system, but not amplitude and phase. We studied a proof-of-concept system of a Herriott FT-IR numerically and experimentally in order to test the combination algorithm and find it's spectral resolution limit. The proof of concept simulation results shows that the Herriott FT-IR's spectral resolution follows the same trend as a standard FT-IR. The preliminary experimental research of the Herriott FT-IR was conducted with a Helium-Neon source and a Toptica 780 nm source. The results imply that the Herriott FT-IR can be an alternative to the standard FT-IR.

Abbreviations

OPD	**O**ptical **P**ath **D**ifference
MOPD	**M**aximal **O**ptical **P**ath **D**ifference
FWHM	**F**ull **W**idth **H**alf **M**aximum
FT-IR	**F**ourier **T**ransform **I**nfra **R**ed
HeNe	**He**lium **Ne**on

Introduction

Optical spectroscopy is a widely used thecnique for non-invasive characterisation of materials and phenomena, via the study of the interaction between light and matter. Spectroscopic techniques are used in many fields of science. For example: imaging and characterizetion of biological tissues [1–3], monitoring biological processes [4], characterizetion of molecules and polymers [5], detection of ingredients in drugs, mesureing atmospheric compositions for envairomental studys [6], characterization of nano-structures [7, 8], topological phases [9], and electronic structure [10] in physics.

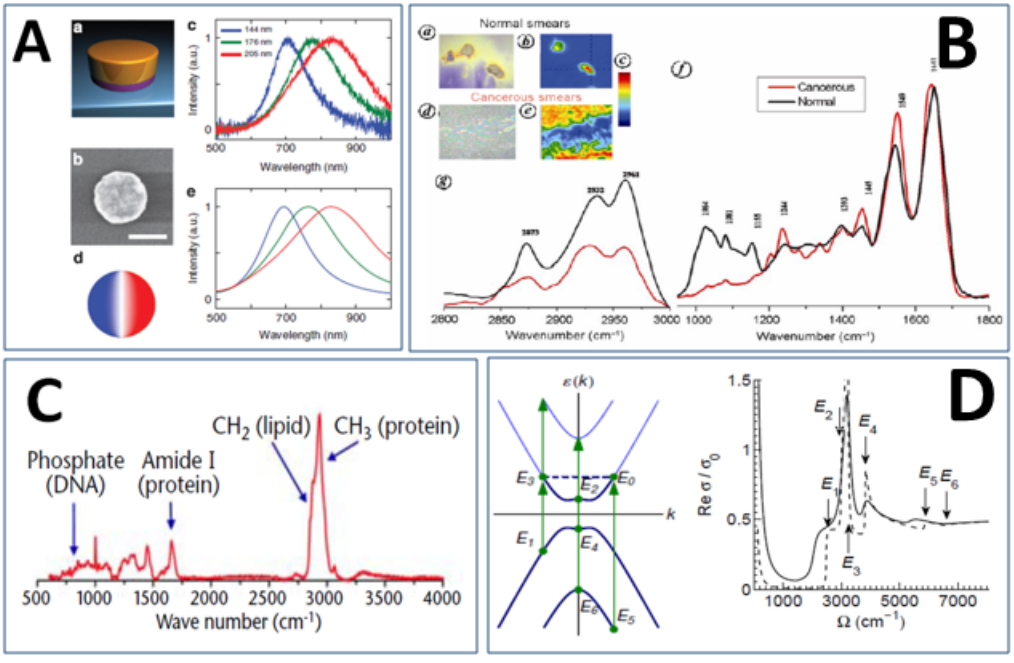

FIGURE 1: Examples for spectroscopic measurements. Figure A [8] shows characterization of a gold nano-disk. Figure B [2] shows a comparison of normal and cancerous cells in a FT-IR spectrum and a microscope. Figure C [1] shows the molecular information contained in Raman spectrum of dried HeLa cells. Figure D [10] shows the Band structure of a graphene bilayer and the corresponding conductivity for wavenumber.

Most spectroscopic techniques belong to one of two categories: dispersive and interferometric spectrometers [11]. Dispersive spectrometers receive spectrum by separating the spectral frequencies of light. Usually, these spectrometers angularly divide light via a

dispersive optical element such as a prism or a grating. The light is then projected on a screen or through a slit, where the wavelength is matched to a specific position in which the intensity of the light is registered.

Interferometric spectrometers receive spectrum by analysing an interference pattern either by spatial separation like the fabry-perot spectrometer or Fourier transformation like the FT-IR. The Fourier Transform Infra-Red (FT-IR) is one of the most common interferometric spectrometers. In a standard FT-IR spectrometer, an interference signal of a Michelson interferometer is sampled as a function of a changing optical path difference (OPD) also known as interferogram. The interferogram is then Fourier transformed from space domain to frequency domain in order to get the spectrum. The resolution of this spectrometer is proportional to the inverse of its largest optical path difference. Therefore, in order to obtain a high spectral resolution FT-IR, one must have a large sized FT-IR spectrometer. Or else, have a small sized FT-IR with low spectral resolution. And this is the FT-IR's resolution-size trade-off.

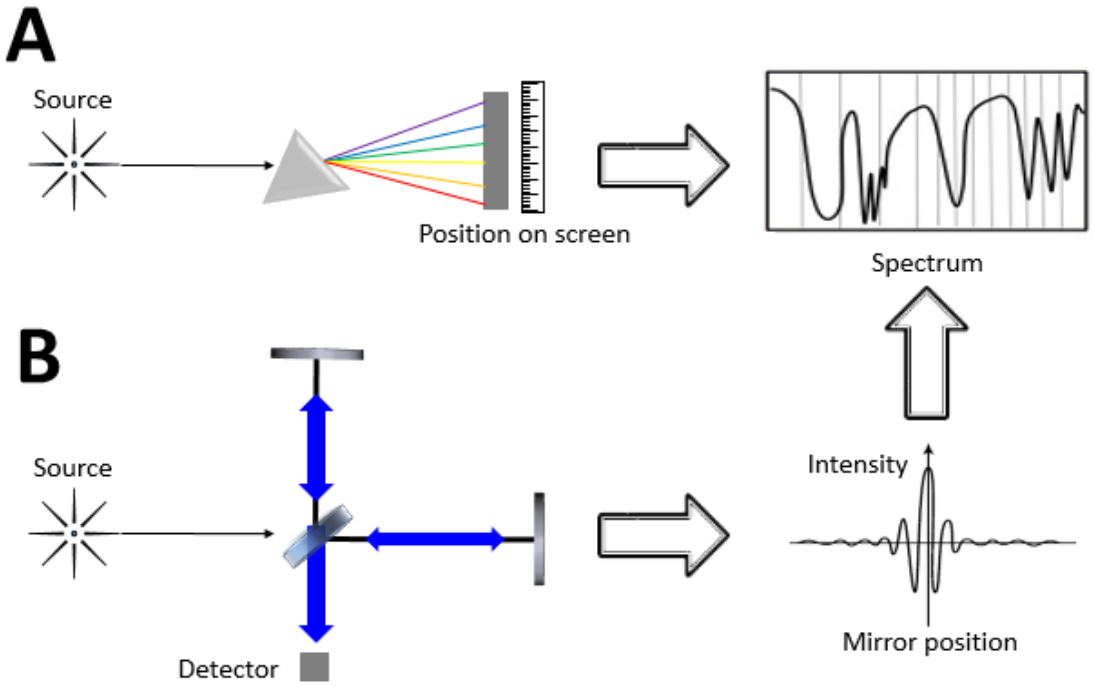

FIGURE 2: Schematic representation of the two spectrometer types. Figure A show a dispersive spectrometer with a prism as the dispersive element. Figure B shows a FT-IR based on a Michelson interferometer as an example for an interferometric spectrometer. The right side of the figure shows the spectrum acquisition process for both spectrometers: the spectrum of the dispersive spectrometer is determined by the position of light on the screen and for the FT-IR spectrometer, the spectrum is calculated according to the interferogram

In this thesis we tried to provide a solution for the resolution-size trade-off of the FT-IR spectrometer. To do so, we embedded a curved mirror resonator (a.k.a "Herriott cell") in the fixed (reference) arm of the interferometer. The Herriott cell can provide long OPD

folded in space. Thus, by tuning the Herriott cell's OPD, the fixed interferometer arm can provide multiple references for the moving arm. Therefore, making high spectral resolution amenable to spatially constrained systems.

The Herriott cell has distinct optical path modes that have a one to one, non linear relation to the cell length. The research of the Herriott cell so far focused on the shape and position of the Herriott cell modes and the Herriott cell was mainly applied as a long optical path generator in a single mode fashion [12]. We also investigated the effects of a Herriott cell on a Gaussian beam and whether it can be used in an optical system in a multi-mode fashion. To do so, we've studied the Herriott cell theoretically, numerically and experimentally. We have found that the Herriott cell conserve a Gaussian beam's size and can be tuned to conserve an optical system alignment, but beam output of different Herriott cell modes differ in amplitude. Additionally, our theoretical formula for the Herriott cell mode-OPD and simulation based on Herriott's mode shape are compatible with the experimental Herriott cell.

Our research of the FT-IR focused on two main fronts: connecting a Herriott cell in a multi-mode fashion to a standard FT-IR optical system, and the effects on the FT-IR spectrum. To do so, the Herriott FT-IR was researched for the purpose of finding out how to correctly combine different FT-IR signals and what is the resolution limit of the Herriott FT-IR. We have designed a unique signal processing algorithm for combining the Herriott FT-IR interferograms and correcting amplitude and phase distortions generated by the Herriott cell. In order to test the Herriott FT-IR resolution limit, we built a proof-of-concept system comparing the spectrum of monochromatic light measured in a single mode Herriott FT-IR for reference and a multi-mode Herriott FT-IR with the same maximal OPD. The proof of concept simulation results showed that the resolution limit of the Herriott FT-IR is similar to the standard FT-IR resolution limit. Furtheremore, the resolution of combining the Herriott FT-IR interferograms is equal to the reference resolution. The experimental results with Helium-Neon source showed weak similarity to the simulation results. Although, due to the spectral width of the source the results are not unambiguous. The experimental results with the Toptica 780 nm source was inconclusive due to mechanical noise setting and upper limit on the spectral resolution much higher then the difference between the OPD changes.

The results imply that a Herriott FT-IR can be a solution for the size-resolution trade-off of the FT-IR spectrometer, and many research facilities with spatial constraints can benefit from a compact, high resolution FT-IR spectrometer.

Chapter 1. *Background*

1.1. *Beam profiles and optical interference*

A general form of an Electromagnetic field can be written as [13]

$$\vec{E} = E_0 e^{i\phi}$$

where the amplitude E_0 and phase ϕ are constants.

Plane wave

A plane wave is an EM wave whose wave front uniformly propagates in time and space [13] . The complex phase of a plane wave propagating in the $\hat{z}$ direction is:

$$\phi = kz - \omega t \tag{1.1}$$

where $k = \frac{2\pi}{\lambda} = 2\pi\sigma$ is the wavenumber and ω is the frequency. Therefore the electric field of a plane wave can be written as:

$$\vec{E}_{in}(\vec{r}, t) = E_0 e^{i(2\pi\vec{\sigma}\vec{r} - \omega t)} + C.C \tag{1.2}$$

Gaussian beam

A Gaussian wave is an EM wave whose wave front present a Gaussian amplitude and phase [14], see figure 1.1. This beam is a solution of the paraxial Helmholtz equation, for a wave propagating in the $\hat{z}$ direction:

$$\vec{E}_{in}(r, z, t) = E_0 \frac{w_0}{W(z)} e^{\frac{-r^2}{W^2(z)}} e^{-i\left(2\pi\vec{\sigma}\left(z + \frac{r^2}{2R(z)} - \psi(z)\right) - \omega t\right)} \tag{1.3}$$

Therefore the complex phase of a Gaussian beam propagating in the $\hat{z}$ direction will be:

$$\phi = 2\pi\vec{\sigma}\left(z + \frac{r^2}{2R(z)} - \psi(z)\right) - \omega t \tag{1.4}$$

Where $r^2 = x^2 + y^2$ is the radial distance from the center of the beam, $W(z)$ is the beam radius at distance z from the beam focus ,$w_0 = W(0)$ is the waist radius - the minimal radius size of the beam at the focus, $R(z)$ is the radius of curvature of the beam at distance z from the beam focus and $\psi(z)$ is the Gouy phase.

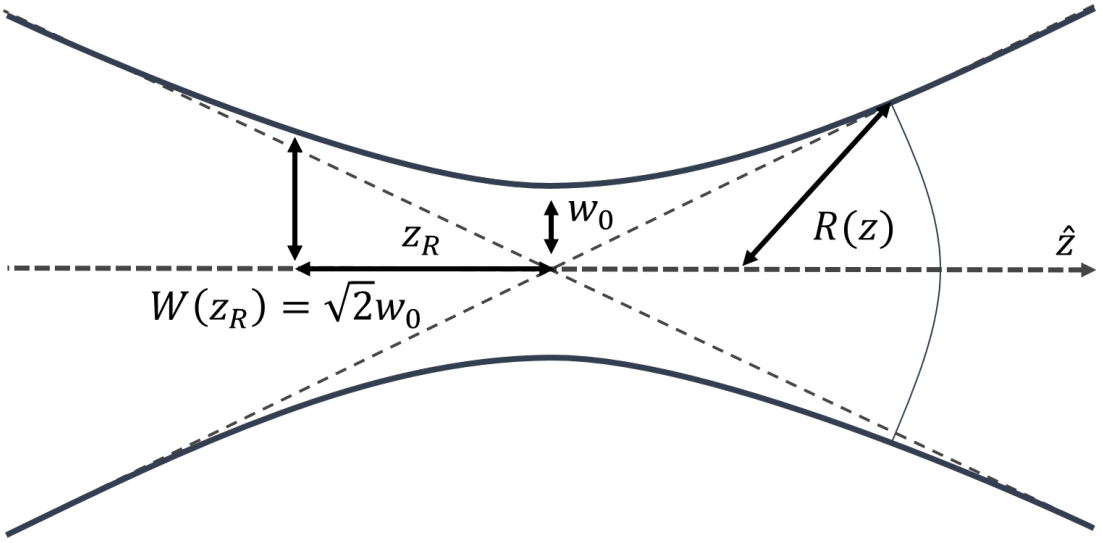

FIGURE 1.1: Gaussian beam propagating at direction $\hat{z}$ with w_0 at the origin

By defining a constant known as the beam Rayleigh range and marking the distance z_R from the focus in which $W(z_R) = \sqrt{2}w_0$ the mathematical terms of the beam z dependent parameters are generated:

$$\begin{aligned}
&z_R = \frac{\pi w_0^2}{\lambda} \\
&R(z) = z + \frac{z_R^2}{z} \\
&W(z) = w_0\sqrt{1 + \frac{z_R^2}{z^2}} \\
&q(z) = z + iz_R = \frac{1}{R} - \frac{i\lambda}{\pi w^2(z)} \quad \text{complex beam parameter}
\end{aligned} \tag{1.5}$$

Ray Transfer Method

The ray transfer method or ABCD matrix method [13, 14] uses the assumption of circularly symmetric rays and optical components to trace EM waves through optical systems. The ray can be described by its distance y, and angle θ with respect to the optical axis $\hat{z}$.

$$\begin{pmatrix} y \\ \theta \end{pmatrix}$$

This method describes an input ray entering an optical system and output ray exiting the system in a linear relation under small angle approximation ($sin\theta \simeq \theta$):

$$\begin{aligned} y_2 =& At_1 + B\theta_1 \\ \theta_2 =& Ct_1 + D\theta_1 \end{aligned} \tag{1.6}$$

The set of equations in 1.6 can be written in a matrix form:

$$\begin{pmatrix} y_2 \\ \theta_2 \end{pmatrix} = \begin{pmatrix} A & B \\ C & D \end{pmatrix} \begin{pmatrix} y_1 \\ \theta_1 \end{pmatrix} \tag{1.7}$$

It is convenient to represent each optical component with a matrix and then represent the system as the multiplication results of its parts. Each component matrix can be found by the set of equations in 1.6 or by:

$$\begin{aligned} A &= \left.\frac{y_2}{y_1}\right|_{\theta_1=0} & B &= \left.\frac{y_2}{\theta_1}\right|_{y_1=0} \\ C &= \left.\frac{\theta_2}{y_1}\right|_{\theta_1=0} & D &= \left.\frac{\theta_2}{\theta_1}\right|_{y_1=0} \end{aligned} \tag{1.8}$$

For example, two basic components in an optical system: free space propagation and a thin lens (or a curved mirror) [14].

$$T_{prop} = \begin{pmatrix} 1 & d \\ 0 & 1 \end{pmatrix} \qquad T_{lens} = \begin{pmatrix} 1 & 0 \\ -\frac{1}{f} & 1 \end{pmatrix} \tag{1.9}$$

where d is the distance of propagation and f is the focal length of the lens (or curved mirror).

Handling a Gaussian beam is made easier to implement in the matrix method when considering the complex beam parameter defined by equation 1.5. When defining the Gaussian ray as $\begin{pmatrix} q \\ 1 \end{pmatrix}$ [14, 15], the output ray will receive the form:

$$q_2 = \frac{Aq_1 + B}{Cq_1 + D} \tag{1.10}$$

and from 1.5 and the remaining beam parameters can be calculated.

Optical Interference

Optical interference is the result of superposition of two EM waves. Generally this can be described using the intensity pattern [13, 16]

$$I(\vec{r}, t) = \left| \sum \vec{E}(\vec{r}, t) \right|^2 \tag{1.11}$$

The superposition of two general EM waves of the same frequency and polarization can be written as:

$$E_{superposition}((\vec{r}, t)) = E_1 e^{-i\phi_1(\vec{r})} + E_2 e^{-i\phi_2(\vec{r})}$$

Which is applied to the equation 1.11 to produce the intensity:

$$I(\vec{r}, t) = I_1 + I_2 + 2\sqrt{I_1 I_2} cos[\Delta\phi(\vec{r})] \tag{1.12}$$

$$\text{where} \quad \Delta\phi(\vec{r}) = |\phi_1(\vec{r}) - \phi_2(\vec{r})| \quad \text{and} \quad I_1, I_2 = |E_1|^2, |E_2|^2 \quad \text{respectivly}$$

From this equation the condition for constructive and destructive interference can be derived:

$$\begin{cases} \Delta\phi(\vec{r}) = 2\pi n & \text{constructive interference} \\ \Delta\phi(\vec{r}) = 2\pi(n+1) & \text{destructive interference} \end{cases} \tag{1.13}$$

where n in an integer

Interference of Equal Inclination

In the following section, we will briefly describe the geometry of interference fringes for two beams of equal Inclination. Let us consider the specific case of two identical beams that differ only by their propagation on the $\hat{z}$ axis interfering.

Plane Wave Interference

Beams that originated from a point source have a phase of the form $\Delta\phi = kz$. Interference of equal inclination for these beams will produce non-localized fringes according to the conditions presented in the equation 1.13. However, in reality, all sources have a finite size diameter referred to as an extended source. For an extended source interference, assuming the interfering beams are of equal inclination in space, the interference pattern will present Haidinger fringes of concentric circular form[13].
Assuming the beams divergence is small i.e. $\theta = \theta_1 \simeq \theta_2$, the OPD resulting of beam divergence at point P is $\delta = |R_1 - R_2| = 2\Delta D cos(\theta)$. By applying this to equation 1.13 the condition for a bright fringe of n^{th} order at a polar angle θ_n can be received:

$$2\Delta D cos(\theta_n) = n\lambda \tag{1.14}$$

Assuming small-angle approximation produces

$$\begin{cases} cos\theta_n \approx 1 - \frac{\theta_n^2}{2} \\ \theta_n \simeq \frac{r_n}{R_0} \end{cases} \Rightarrow cos\theta_n = 1 - \frac{r_n^2}{2R_0^2}$$

substituting into equation (1.14), produces a circle equation:

$$n\lambda = 2\Delta D \left(1 - \frac{r_n^2}{2R_0^2}\right)$$

whereby the radius of a bright fringe is:

$$r_n = R_0\sqrt{\frac{n\lambda}{\Delta D}} \tag{1.15}$$

Gaussian Beams Interference

For a Gaussian beam, the result is similar, however the phase treatment is different. Let us consider two Gaussian beams that differ only by ΔD, the OPD on the z axis is projected on a screen at the X-Y plane. The z difference produces a difference in the beams radius of curvature whereby the complex phase of each beam can be written as [17]:

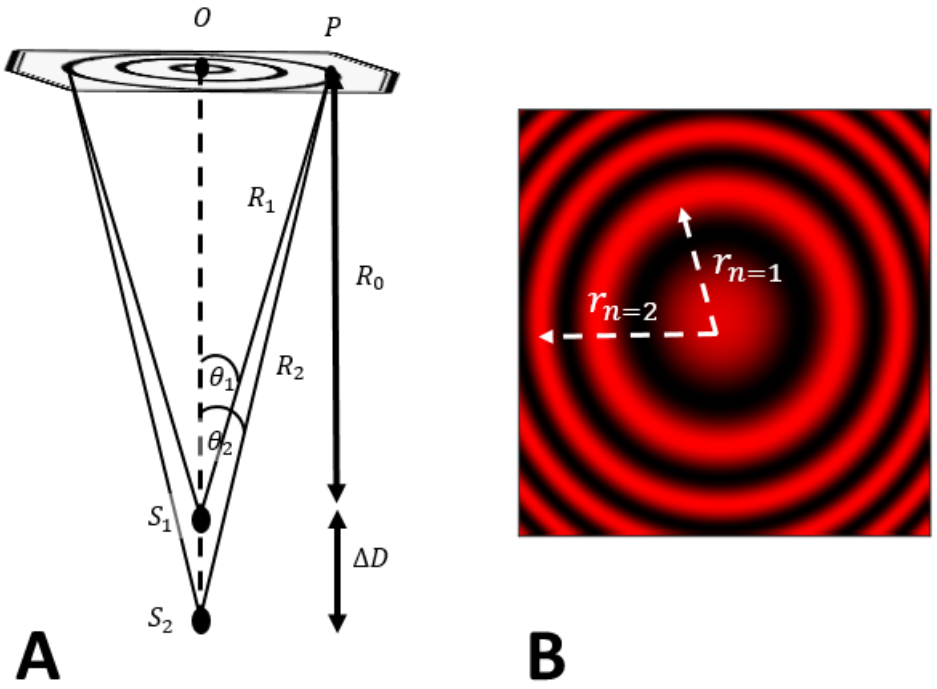

FIGURE 1.2: An illustration of extended source interference of equal inclination. In figure 1.2.A a simplified scheme of the extended sources S_1, S_2 divergence and interference. For a plane wave R_0, R_1, R_2 are the OPD of S_1 at point O, at point P and the OPD of S_2 from point P respectively . for a Gaussian beam R_1, R_2 represent the radius of curvature at $z = R_0$ and $z = R_0 + \Delta D$ respectively. In figure 1.2.B a numeric simulation of the interference pattern of two Gaussian beams, circular fringe pattern is presented as described by equation 1.16 .

$$\begin{cases} \phi_1 = \frac{kr^2}{2R_1} + kD_1 \\ \phi_2 = \frac{kr^2}{2R_2} + kD_2 \end{cases} \Rightarrow \Delta\phi = k\left(\frac{r^2}{2}\left|\frac{1}{R_1} - \frac{1}{R_2}\right| + \Delta D\right)$$

When applying the condition of constructive interference $\Delta\phi = 2\pi n$ produces:

$$\frac{2\pi}{\lambda}\left(\frac{r^2}{2}\left|\frac{R_2 - R_1}{R_1 R_2}\right| + \Delta D\right) = 2\pi n$$

Which is a circle equation, for a constant ΔD the fringe radius received is:

$$r_n = \sqrt{\frac{2R_1R_2(\lambda n + \Delta D)}{|R_1 - R_2|}} \tag{1.16}$$

1.2. *FT-IR Spectrometer*

FT-IR spectrometer is a common method of spectroscopy based on the Michelson interferometer. In this section we will review the mathematical principal behind the FT-IR spectrometer and the theoretical limitations of this method. The spectrum produced by the FT-IR spectrometer , $\tilde{S}(\sigma)$, is the result of Fourier transforming an interferogram $I(\Delta D)$. The interferogram is produced by changing the length of one of the Michelson interferometer's arms and registering the interference signal.

Fourier Transform

A Fourier transform is a linear transform between two inverse domains. For any function $f(x)$, the Fourier transform can be denoted $F(\sigma)$, where the product of x and σ is dimensionless. The Fourier transform and the inverse Fourier transform are defined as:

$$\begin{cases} F(\sigma) = \int_{-\infty}^{\infty} f(x) e^{-2\pi\sigma x} dx \\ f(x) = \int_{-\infty}^{\infty} F(\sigma) e^{2\pi\sigma x} d\sigma \end{cases} \tag{1.17}$$

In this thesis, the relevant transformation is between space, usually represented as variable x or z, and k-space usually represented by wavenumber $\sigma = \frac{k}{2\pi}$ or k. Fourier transform also translates between multiplication in space to convolution in k-space.
Consider a function $h(x)$, a multiplication of functions $f(x), g(x)$ under Fourier transformation this translates into:

$$\begin{cases} h(x) = f(x) \bullet g(x) \\ H(\sigma) = F(\sigma) \circledast G(\sigma) = \int_{-\infty}^{\infty} F(\sigma) G(\sigma' - \sigma) d\sigma \end{cases} \tag{1.18}$$

Cross-Correlation

A useful tool for signal comperison is the cross-covariens or cross-corroletion function. Let us consider two signals $f_1(x), f_2(x)$, the cross-correlation function of these signals is [18]

$$\rho(x) = \int_{-\infty}^{\infty} f_1(y) f_2(y + x) dy \tag{1.19}$$

If there is a spatial shift d between the functions- $f_1(x) = f_2(x + d)$ then the maximal value of $\rho(x)$ will be at $x = d$.

Michelson Interferometer

In a Michelson interferometer a single beam is dividede in two by a beam-splitter. The resulting beams transfer through different arms and re-converge at a second beam-splitter (commonly the same one) as shown in figure 1.3 [13, 16].

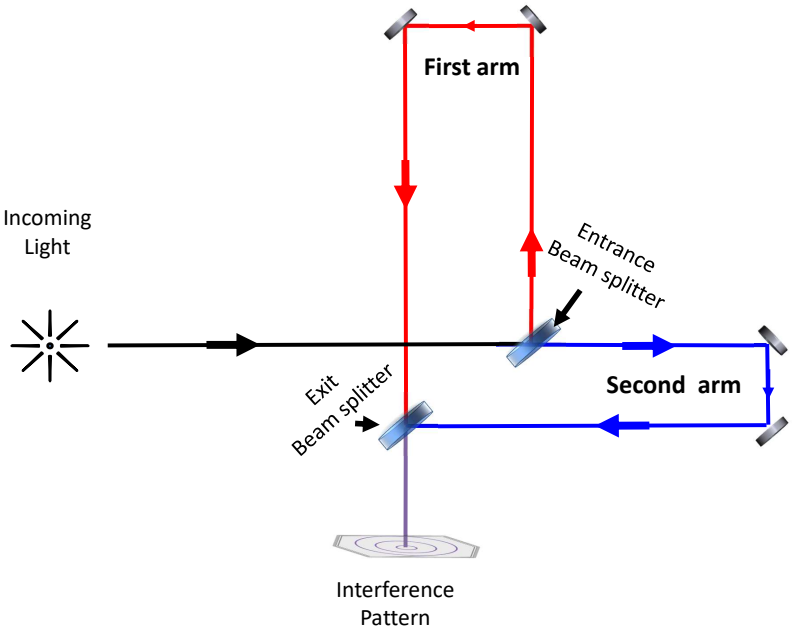

FIGURE 1.3: A Michelson interferometer

Consider a monochromatic light of wavenumber σ_0 and intensity $2S(\sigma_0)$ travelling through a Michelson interferometer. Since the interference pattern of the Michelson interferometer is an interference of equal inclination it can be described by replacing $\Delta\phi\vec{r}$ with $2\pi\sigma_0 x$ in equation 1.12 where x is the OPD. The interference pattern I of a changing OPD x is called the interferogram and can be wriiten as:

$$I_{\sigma_0}(x) = S(\sigma_0)[1 + cos(2\pi\sigma_0 x)]$$

An interference pattern of a broadband source will be the superposition of $I_{\sigma_0}(x)$

$$I_0(x) = \int_0^\infty S(\sigma)[1 + cos(2\pi\sigma x)]d\sigma$$

Rearranging this expression - subtracting the mean value and present as exponents - produces:

$$I(x) = I_0(x) - I_0\bar{(x)} = \int_0^\infty S(\sigma)cos(2\pi\sigma x)d\sigma$$

$$I(x) = \int_{-\infty}^{\infty} S(\sigma)e^{-2\pi\sigma x}d\sigma \tag{1.20}$$

Equation 1.20 is similar to the Fourier transform in 1.17. Therefore, the spectrum - $S(\sigma)$ - can be extracted by inverting the connection [16]:

$$S(\sigma) = \int_{-\infty}^{\infty} I(x)e^{2\pi\sigma x}dx \tag{1.21}$$

Which is the mathematical justification for using the Michelson interferometer as a spectrometer.

Resolution control: A Theory of a perfect instrument

The relation between the spectrum and the interferogram in 1.21 is true only for an infinitely long interferogram, i.e. $-\infty \leq x \leq \infty$. However, in a real interferometer a finite arbitrary section $x_0 - L \leq x \leq x_0 + L$ of maximal OPD L is sampled [16].
This is equivalent to a rectangular function $\Pi\left(\frac{x}{2L}\right)$ of length $2L$ located at x_0 multiplied by an infinitely long interferogram. The resulting spectrum, as implied in equation 1.18 is a convolution of the desired spectrum $S(\sigma)$ and the Fourier transform of a rectangular function $\theta(\sigma)$:

$$\begin{cases} I_{observed}(x) = I(x) \bullet \Pi\left(\frac{x-x_0}{2L}\right) \\ S_{observed}(\sigma) = S(\sigma) \circledast \theta(\sigma) \end{cases} \tag{1.22}$$

$\theta(\sigma)$ can be calculated and analysed:

$$\theta(\sigma) = \int_{-\infty}^{\infty} \Pi\left(\frac{x - x_0}{2L})\right) e^{2\pi\sigma x}dx = \frac{sin(2L\sigma)}{\sigma} = 2Lsinc(2L\sigma) \tag{1.23}$$

The resolution width $\delta\sigma$ and its relation to the full width half maximum (FWHM) of a *sinc* function is:

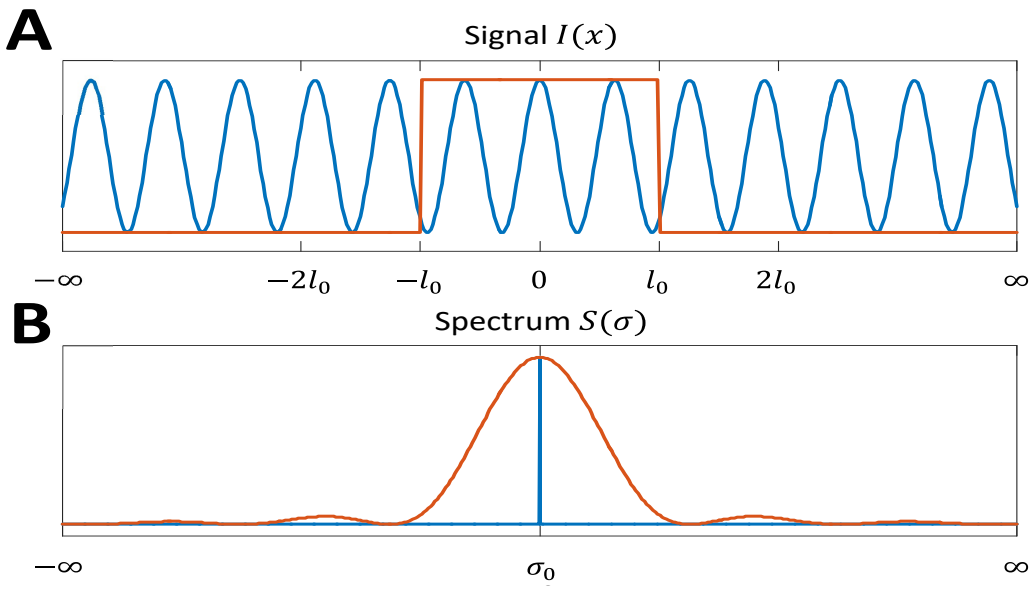

FIGURE 1.4: The interferogram and spectrum of a monochromatic light of wavenumber σ_0. Figure 1.4.A presents the theoretical infinitely long interferogram $I(x) = cos(2\pi\sigma_0)$ in blue and the rectangular function $\Pi(\frac{x}{2l_0})$ defining the sampled section in red. Figure 1.4.B presents the theoretical spectrum of a monochromatic light $\delta(\sigma - \sigma_0)$ (a delta function at σ_0) in blue and Fourier transform of the rectangular function $\Pi(\frac{x}{2l_0})$ in red. This example highlights the limit that a finite length sampling impose on the spectral resolution of the Fourier transform.

$$FWHM = 1.207\delta\sigma = 1.207\left(\frac{1}{2L}\right) \tag{1.24}$$

Equation 1.24 provides the resolution limit of a finite length interferogram which a theoretical line of infinitesimal width that translates into a sinc that has a finite sized width $\delta\sigma$.

1.3. *Herriott Cell*

The Herriott cell [19, 20] is a curved mirror resonator with distinct optical path modes which can be controlled with various degrees of freedom in the system. Herriott cells are built of two curved mirrors placed opposite each other. In our research we focused on a cell with a hole in the center of one of the mirrors in which a light beam entered and exited the cell, see figure **??**. The number of repetitions in the cell are mainly controlled by the following parameters: ζ, f, d. Where ζ the angle of the entering beam relative to the $\hat{z}$ axis, f the focal length of the curved mirrors and d the size of the cell - the distance between the mirrors.

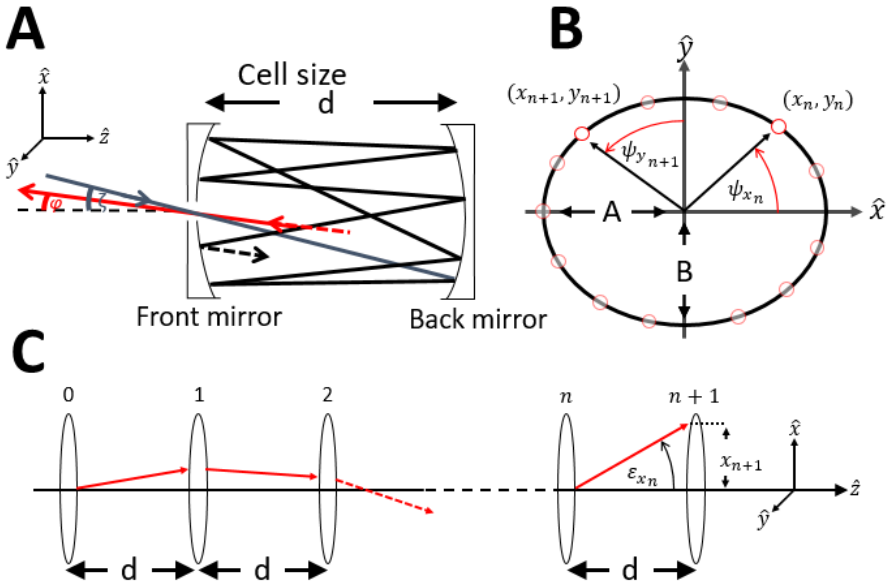

FIGURE 1.5: An illustration of a Herriott cell. Figure **??**.A presents a cross section of the cell in the x-z plane, illustrating the input (blue) and output (red) beams at angles ζ, φ relative to the $\hat{z}$ axis and the round trip of the beam inside the cell at an unknown general mode at cell size d. Figure **??**.B present a projection of the beam spot location in the x-y plane laying on an ellipse. Figure **??**.C present an array of n thin lenses equally spaced at distance d from one another, representing an optically equivalent system to the Herriott cell presented at figure **??**.A.

Ellipse Shape Calculation and Mode Selection Rules

A cavity system of two opposing equal curved mirrors is equivalent to a system composed of equally spaced thin lenses of the same focal length f as shown in figure 1.5.C. The beam in the section between lens n and $(n+1)$ is described by coordinates (x_n, y_n) and the corresponding slopes (x'_n, y'_n). The condition for a beam's exit from the cell can be

demanded as:

$$(x_N, y_N) \simeq (x_0, y_0)e \tag{1.25}$$

where N is an even integer.
Herriott [19] found that the beam location on the nth lens can be written as:

$$\begin{aligned} x_n &= Asin(n\theta + \alpha) \\ y_n &= Bsin(n\theta + \beta) \end{aligned} \tag{1.26}$$

by defining :

$$\begin{gathered} cos\theta = 1 - \frac{d}{2f}, \quad tan\alpha = \frac{\sqrt{\frac{4f}{d} - 1}}{1 + 2f\frac{x_0'}{x_0}}, \quad tan\beta = \frac{\sqrt{\frac{4f}{d} - 1}}{1 + 2f\frac{y_0'}{y_0}}. \\ A = \sqrt{\frac{4f}{4f - d}\left(x_0^2 + dx_0x_0' + fd(x_0')^2\right)}, \quad B = \sqrt{\frac{4f}{4f - d}\left(y_0^2 + dy_0y_0' + fd(y_0')^2\right)} \end{gathered} \tag{1.27}$$

In figure 1.5.B this form is translated into an ellipse of semi major and minor axis A,B and $n\theta + \alpha = \psi_{x_n}$, $n\theta + \beta = \psi_{y_n}$

And it is easy to see that the exiting condition in 1.25 is met when

$$2\sigma\theta = 2\pi\mu \tag{1.28}$$

where $\sigma = N/2$ is the number of round trips in the cell, it can also be easily recognized by the number of beam spots on the back mirror.

The cell's modes can be defined by the fraction $\frac{f}{d}$

ν	8	3	13	4	5	6
$\frac{f}{d}$	0.9	1	1.2	1.7	2.6	4.4

TABLE 1.1: Some of Herriott cell modes as found in in the lab using a He-Ne laser

1.4. *The Role of Spectral Dependent Phase*

In this section we will establish the physical basis for a discussion on the phase accumulated from the mirrors of the optical system.

Reflected Light from a Surface with Complex Refraction index

According to Fresnel's equation [13], the amplitude reflectance r of light reflected at an interface between two media in normal incidence is

$$r_{||} = \frac{E_r}{E_i} = -\frac{n_1 - n_0}{n_1 + n_0} \tag{1.29}$$

where E_r, E_i are the amplitudes of the reflected and incident EM fields and n_0, n_1 are the refractive indices of the media.

Exact calculation of the reflectance of light from metal coated mirrors requires consideration of the complex refractive index of the metal [21]. Substituting the real refraction index of one of the media to a complex refractive index $n_1 \rightarrow n_1 - ik_1$ generates a complex amplitude reflectance

$$r = \frac{n_0^2 - (n_1^2 + k_1^2) + 2in_0k_1}{(n_1 + n_0)^2 + k_1^2} = \tilde{r}e^{i\beta} \tag{1.30}$$

Where $\tilde{r}$ is the real part of the reflectance and the phase change between the reflected and incident light is β

$$\begin{cases} \beta = \pi - \rho \\ \rho = tan^{-1}(\frac{2n_0k_1}{n_1^2+k_1^2-n_0^2}) \\ 0 \leq \rho \leq \frac{\pi}{2} \end{cases} \tag{1.31}$$

Evaluation of Metallic Refraction Index

Evaluation of the complex refractive index can be done using Drude model [22]

$$n^2(\omega) = \varepsilon(\infty) - \frac{\omega_p^2}{\omega^2 + i\omega\Gamma_d} \tag{1.32}$$

where ω is the EM field frequency ,$\varepsilon(\infty)$ is the high frequency contribution, ω_p is the plasma frequency and Γ_d is damping factor. These constants can be calculated or extracted experimentally.

1.5. *Pulse Autocorrelation through a Nonlinear Medium*

In this section we will present the physical basis for the calibration of the Herriott cell's relative optical path to an adjacent optical system. The calibration is done by using a nonlinear crystal to trace the correlation signal between two short pulses traversing through the system.

Second Order Nonlinear Process

Nonlinear Processes occur in media with polarization $\vec{P}$ that have a non-linear relation to the electromagnetic field $\vec{E}$ [23]. In particular, for second order nonlinear media, the polarization is proportional to $|\vec{E}|^2$.

$$\vec{P}(t) = \chi^{(1)}\vec{E}(t) + \chi^{(2)}\vec{E}^2(t) \tag{1.33}$$

where $\chi^{(1)}, \chi^{(2)}$ are the first and second order susceptibility. Since the EM wave is influenced by the polarization according to the wave equation in medium:

$$-\nabla^2\vec{E}^2 + \frac{1}{c^2}\vec{E} = -\frac{4\pi}{c^2}\frac{\partial^2\vec{P}}{\partial t^2}$$

The intensity of the nonlinear polarization component will determine the EM wave frequency of the wave coming out of the medium.

Let us consider an EM wave with two distinct frequencies ω_1, ω_2 propagating in a non linear medium:

$$\vec{E}(t) = E_1 e^{-i\omega_1 t} + E_2 e^{-i\omega_2 t} + C.C$$

. The second order contribution to the polarization is:

$$\vec{P}^{(2)}(t) = \chi^{(2)}\vec{E}^2(t) = \sum_n P(\omega_n)e^{-i\omega_n t}$$

$$P(\omega_n) = \begin{cases} P(\omega_{SHG^1} = 2\omega_1) = \chi^{(2)} E_1^2 \\ P(\omega_{SHG^2} = 2\omega_2) = \chi^{(2)} E_2^2 \\ P(\omega_{SFG} = \omega_1 + \omega_2) = \chi^{(2)} E_1 E_2 \\ P(\omega_{DFG} = \omega_1 - \omega_2) = \chi^{(2)} E_1 E_2^* \\ P(\omega_{OR} = 0) = \chi^{(2)} (E_1 E_1^* + E_2 E_2^*) \end{cases} \tag{1.34}$$

The different second order processes are: Second Harmonic Generation - SHG, Sum Frequency Generation - SFG, Difference Frequency Generation - DFG and Optical Rectification - OR. The intensities of the processes are determined by phase matching conditions:

$$\Delta\vec{k} = \begin{cases} 2k_{1,2} & SHG \\ \vec{k}_1 \pm \vec{k}_2 & SFG/DFG \end{cases} = 0 \tag{1.35}$$

And are proportional to the input fields intensities:

$$I_{NL} \propto I_1 I_2 \tag{1.36}$$

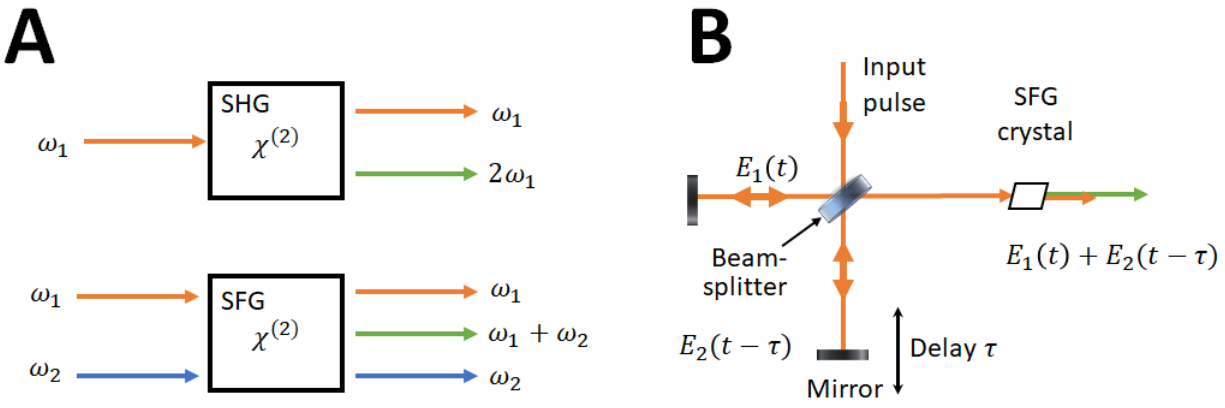

FIGURE 1.6: Figure A presents the geometry of second harmonic generation (SHG) and sum frequency generation (SFG). Figure B present the experimental set up for interferometric autocorrelation using a SFG crystal

Interferometric Autocorrelation

Interferometric autocorrelation is a pulse characterization method that uses an interferometric set-up and a nonlinear crystal to detect the pulse's phase [24]. On this method, a pulse beam is put into a Michelson interferometer and set into a nonlinear crystal after convergence(see figure). The autocorrelation intensity at time τ is defined by:

$$I_{AC}(\tau) = \int_{-\infty}^{\infty} I(t)I(t-\tau)dt \tag{1.37}$$

Let us consider the case that the pulse is split according to frequency so that the pulse in one arm of the interferometer is oscillating with frequency ω_1: , and the pulse in second arm is oscillating with frequency ω_2:

$$\vec{E}_1(t) = \vec{A}_1(t)e^{-i\omega_1(t)}$$
$$\vec{E}_2(t-\tau) = \vec{A}_2(t-\tau)e^{-i\omega_2(t-\tau)}$$

Then the EM wave in the crystal is:

$$\vec{E}_{total} = \vec{E}_1(t) + \vec{E}_2(t-\tau)$$

and the autocorrelation intensity is:

$$I_{AC}(\tau) = \int_{-\infty}^{\infty} |[\vec{E}_1(t) + \vec{E}_2(t-\tau)]^2|^2 dt$$

Let us assume that the nonlinear crystal support the phase matching conditions for up-conversation (SHG,SFG), hence, the intensity terms for DFG and OR are eliminated and the autocorrelation intensity receives the form:

$$I_{AC}(\tau) = \int_{-\infty}^{\infty} \overset{SHG^1}{I_1^2(t)} + \overset{SHG^2}{I_2^2(t-\tau)} + \overset{SFG}{I_1(t)I_2(t-\tau)}dt \tag{1.38}$$

Therefore, the expected spectral measurement should yield $2\omega_1, 2\omega_2$ at all time delays and $\omega_1 + \omega_2$ only for time delay $\tau = 0$.

Chapter 2. *Analysis of Herriott Cell*

The description of the Herriott cell given in section 1.3 is centred around the internal proprieties of the Herriott cell modes. A full characterization of Herriott cells must include a description of how a beam of light responds to the Herriott cell as a part of an optical system. In this chapter we will place the Herriott cell in an optical system and explore the change in a Gaussian beam's optical path: optical path difference and alignment with respect to the rest of the system and the output beam internal properties: size, amplitude and phase. To do so, we have designed an experimental set-up and a simulation in the form of figure 2.1 and compared them. The simulation use ray tracing method (see section 1.1) for evaluating the affect of each optical component in the system. The Herriott cell modes are calculated using Herriott's formulas and reduced to an ABCD matrix. We Have found that the Herriott cell has a non-linear one-to-one relation between the cell size d and the optical path difference L and it conserve alignment and beam size for all modes at any wavelength. The amplitude and phase of the beam however, in not conserved but easily calibrated with regard to the Herriott cell mode and mode order.

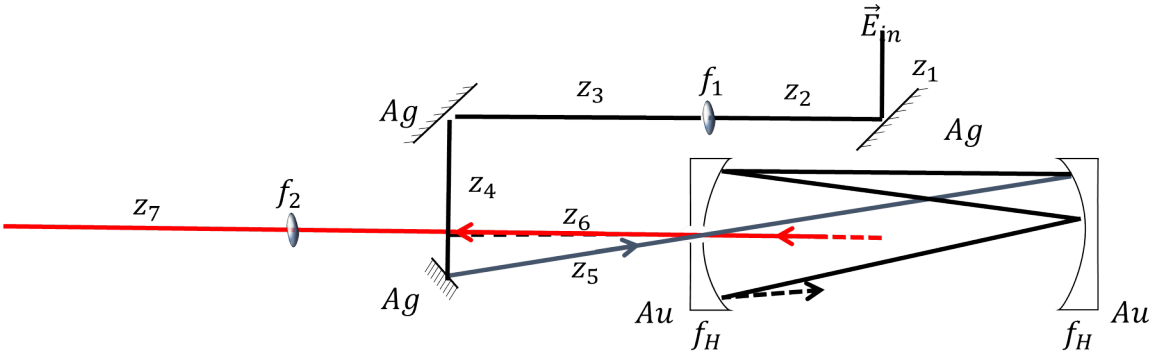

FIGURE 2.1: A graphic representation of the optical elements taken into account in the simulation and experiment: lenses (f_1, f_2, f_H), complex reflection from mirrors (silver and gold), travel through free space ($z_{1..6}$) and Herriott cell.

.

2.1. *Optical Path Properties*

The Herriott cell optical path properties are independent of the input beam. The initial conditions and cell type determine the characterization of the cell in terms of mode shape, OPD and alignment.

Mode Shape

The shape of the Herriott cell mode is described by Herriott in equation 1.26. In this research we found that the modes not only differ in the number of iterations in the cell (σ), but also in size and shape. The shape of the mode is defined by the position of the beam spots on the mirrors and is distinct to each mode. We can also identify stable and unstable modes by conservation of the stable mode shape. The beam spots of unstable modes speared out of the beam spots of stable modes (see figure 2.2). We have noticed that the stable modes tend to maintain longer spans of the cell's size than the unstable ones, an observation we will return to further on.

Alignment

A beam alignment with respect to an optical system containing a Herriott cell is defined by it's location on the $x-y$ plane and it's angle φ with respect to the optical axis z. By this definition the output alignment of mode σ is

$$(x_{2\sigma}, y_{2\sigma}), \quad sin(\varphi_\sigma) = \frac{\sqrt{x_{2\sigma}^2 + y_{2\sigma}^2}}{d_{2\sigma}} \tag{2.1}$$

where $(x_{2\sigma}, y_{2\sigma})$ are defined by 1.26 and 1.27 and we define d_n as

$$\begin{aligned} d_n =& \sqrt{d^2 + \Delta x_n^2 + \Delta y_n^2} \\ \Delta x_n = x_n - x_{n-1} \quad &, \quad \Delta y_n = y_n - y_{n-1} \end{aligned} \tag{2.2}$$

It is easy to see that the trivial output alignment $(x_{2\sigma}, y_{2\sigma}) = (0,0), \quad sin(\varphi_\sigma) = 0$ can only exist if the initial conditions are $(x_0, y_0) = (0,0), \quad sin(\zeta) = 0$ for $\sigma = 1$ and completely misses the point of using the Herriott cell. In our research we found that the alignment of the system can vary between modes and also within modes. We have found that within the stable modes exists a repartition of the same alignment. This is very useful as a quantitative way of distinguishing stable and unstable modes. Furthermore we use the alignment for choosing a specific mode form in a stable mode.

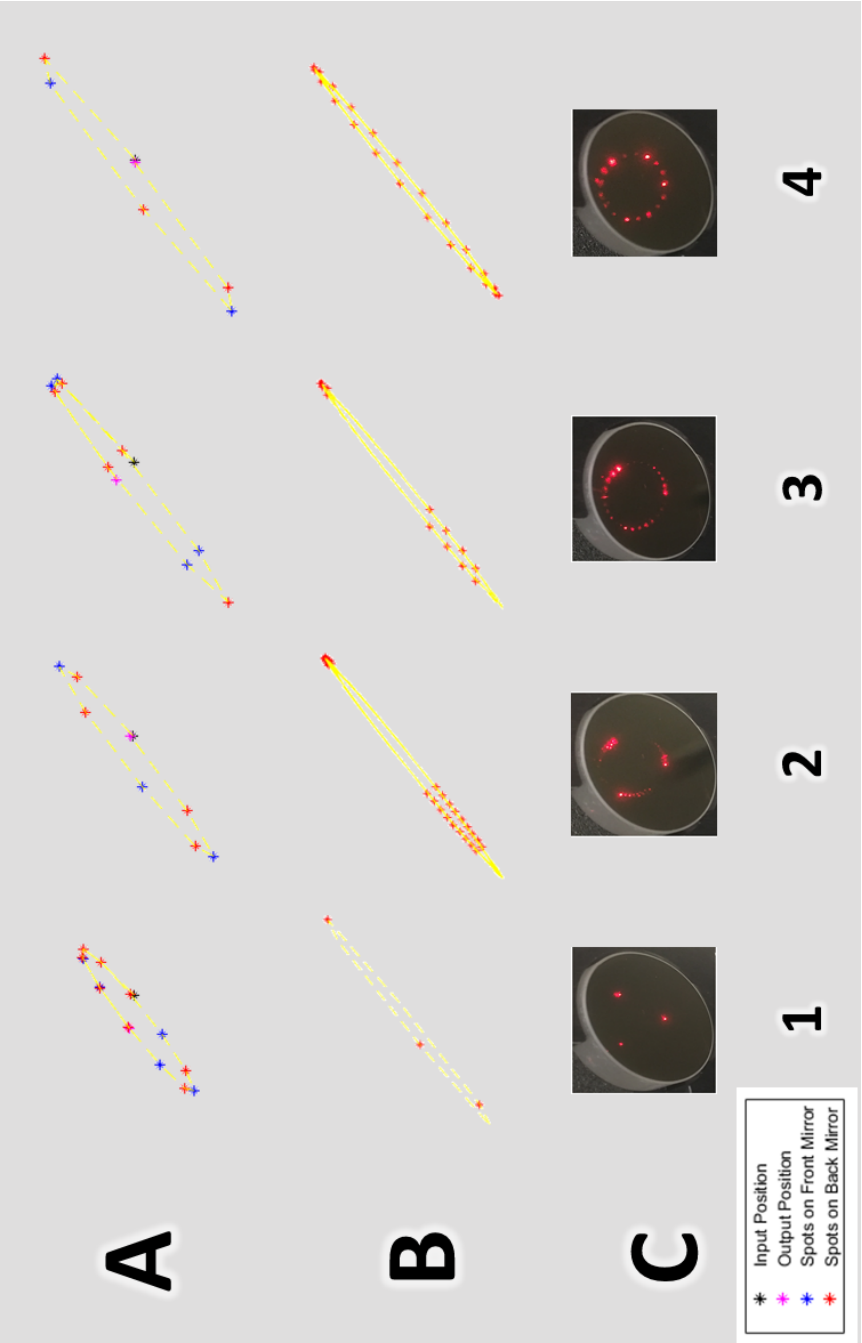

FIGURE 2.2: Characterization of the Herriott cell mode shapes from numerical calculation and experimental observations of the Herriott cell. In A, numerical calculation of mode shapes for stable modes that differ in the cell size alone. The input position - (x_0, y_0) - is constant for all modes and marked with a black starlet, the output position - $(x_{2\sigma}, y_{2\sigma})$ - is marked in magenta, the blue and red starlets mark the (x_n, y_n) location of the beam. Ellipses 1-4 correlate to mode numbers $\sigma = 8, 4, 5, 3$ at cell sizes $d = 64, 116, 155, 198mm$.In B, numerical calculation of mode shapes for the transition from one stable mode (ellipse 1) to another stable mode (ellipse 4) on the $x - y$ plane of the back mirror. Ellipses 2 and 3 present unstable modes in between. In C, experimental observations of the same process as in B. figures B and C illustrate how the unstable modes are spread around the stable mode spots until the mode transition where the mode spots position completely change.

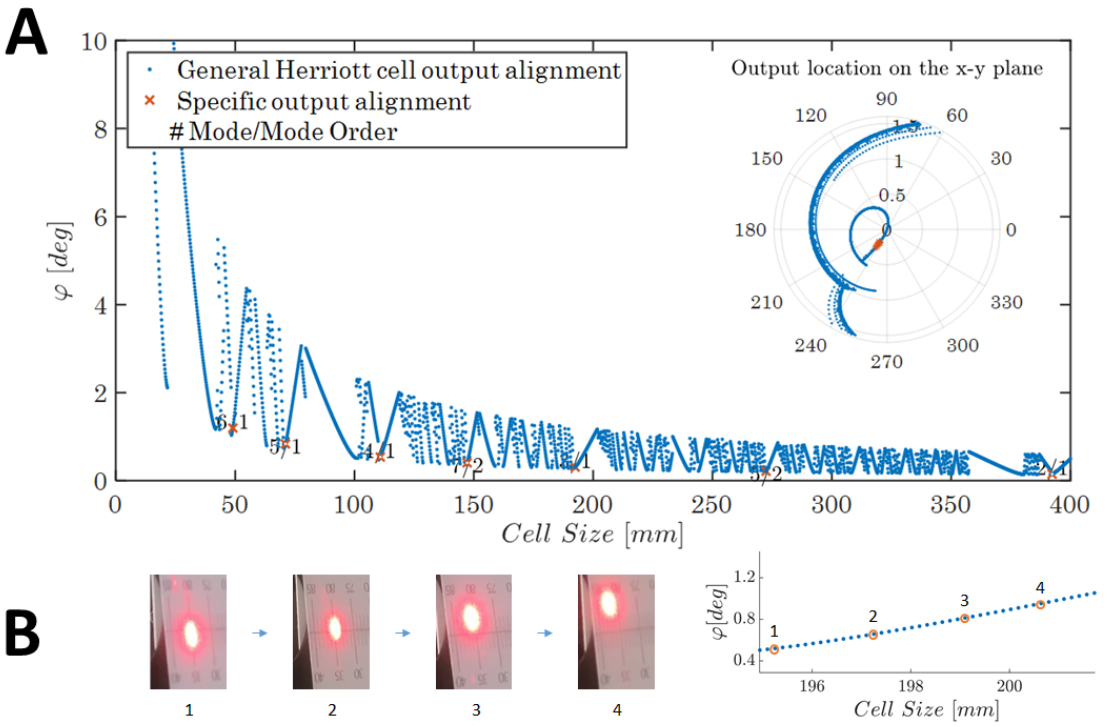

FIGURE 2.3: Properties and effects of the Herriott cell output alignment. In A, results of numerical calculation of all possible alignments of a Herriott cell, presented in blue, and a specific alignment, presented in red with a display of the corresponding mode number (σ) and mode order (μ). The large figure plots the angle φ with respect to the Herriott cell size and the small figure on the top right plots the beam output location on the $x-y$ plane. In B, experimental observations of a Herriott cell output beam projected on a screen. The difference between the pictures is fine tuning of a specific mode, as demonstrated in the figure on the bottom right.

Optical Path Difference

The optical path difference a beam gains in the Herriott cell is dependent of the cell's mode and size. Herriott's equations, 1.26-1.28, help us determine the cell's modes and trace the beam location at each iteration at each mode. Summing the distance d_n gained over all iterations can give us the optical path difference.

$$L(\sigma, d) = \sum_{n=1}^{2\sigma} d_n \tag{2.3}$$

Assuming that The cell's size is much grater then the cell's mirrors i.e $\frac{\Delta x_n}{d}, \frac{\Delta y_n}{d} << 1$ and that the initial conditions support the relations $\alpha \simeq 2\beta$ and $A \approx B$ we can receive an equation on L:

$$L(\sigma, d) = 2d\sigma + \frac{4\sigma A^2}{d} sin^2\left(\frac{\theta}{2}\right) = 2d\sigma + \frac{\sigma A^2}{d}\left(3 + \frac{d}{f} - \frac{d^2}{4f^2}\right) \tag{2.4}$$

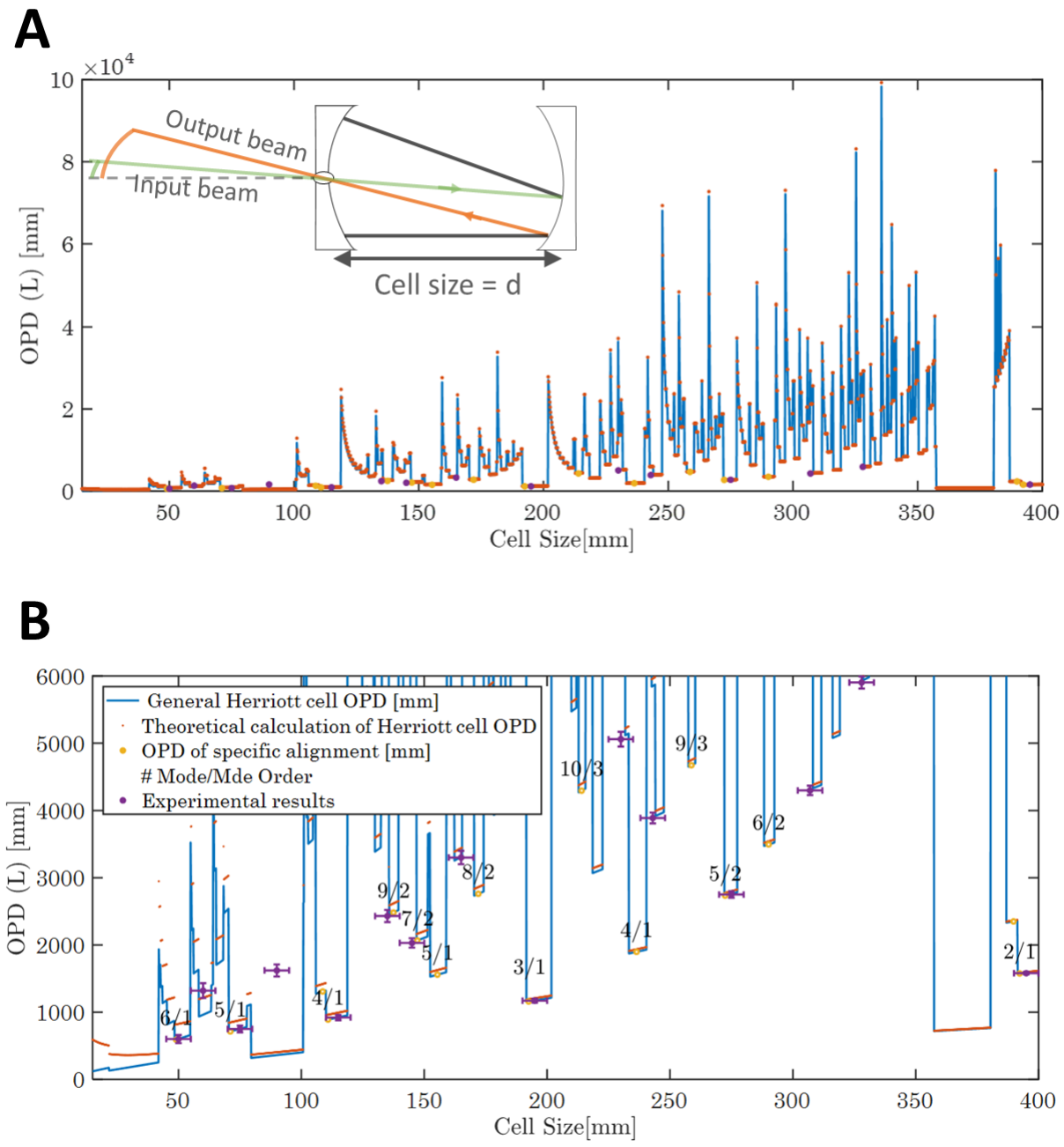

FIGURE 2.4: Typical characterization of a Herriott cell as optical path done inside the cell - L - with regard to the cell's size - d. Figure A present all possible optical paths for a set of given initial conditions : $(x_0, y_0), (x'_0, y'_0, f)$ (1.3). The red markers represent the theoretical (equation 2.4) calculation and the blue lines represent the numerical simulation.Herriott cell modes that meet a specific alignment condition are presented as yellow markers with mode number (σ) and mode order (μ) captions for the numerical calculations and purple markers for the experimental observations. Figure B is a zoom on figure A, restricted for optical paths $0 \leq L \leq 6000\ mm$. This figure shows the similarity between the theoretical, numerical and experimental calculations and measurements. Furthermore, the error bars of the experimental measurements are visible in this figure due to the axis scale. Thus, show that the alignment condition chosen for the simulation is close to the alignment condition of the experiment.

Initial conditions alone can not determine the exact output of a Herriott cell. A specific set of modes can only be determined by exit conditions, in our case we choose to conserve

optical alignment i.e. exit position on the $x-y$ plane and the angle relative the the z axis (φ). Figure 2.4 shows that our formula, simulation and experimental results for the Herriott cell are consistent. Therefore, we conclude that the Herriott cell formula and simulation are good representations for the Herriott cell.

2.2. *Output Beam Properties*

The Herriott cell output beam properties dependent greatly on the input beam. The initial conditions and cell type determine the characterization of the cell in terms of mode shape, OPD and alignment.

Beam Size per Mode

The size of the Herriott cell output beam does not change significantly from the input beam with negligent variance. In experiment we were unable to distinguish the sizes of the input and output beams but in simulation we were able to get a quantitative assessment. Calculating The output beam size for each stable mode produce a mean beam size $\overline{W}_{out} \simeq W_{in}$ with standard deviation of $\Delta W \simeq 0.5\%$. For example, the output of an input beam of size $W_{in} = 2$ mm has a mean size $\overline{W}_{out} = 1.933$ mm with standard deviation $\Delta W \simeq 0.036$ mm.

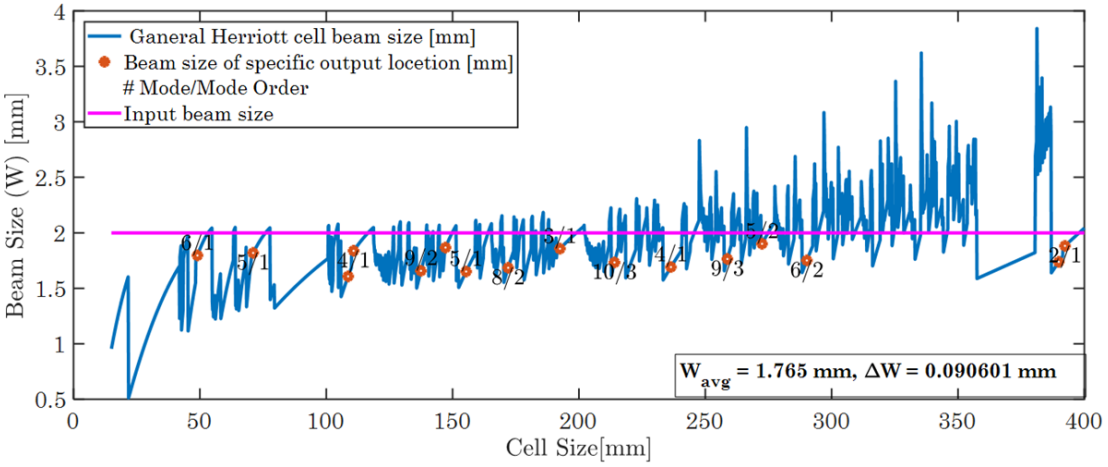

FIGURE 2.5: Representation of a typical size for a Herriott cell output beam. Calculations for a general Herriott cell - all output alignments are allowed - are presented as blue. Herriott cell modes that meet a specific alignment condition are presented as red with detailed mode number (σ) and mode order (μ). The size of the input beam is represented by the magenta line.

Beam Amplitude

The amplitude of the output beam is determined by two main factors, the waist to width relation of the beam and the reflection from the mirrors. A beam with intensity $I = I_0 \propto A_0^2$ reflected 2σ times from a mirror with reflection r will have intensity $I = r^{2\sigma} I_0$ and the EM amplitude will be $A = r^{\sigma} A_0$.

$$A = \frac{\omega_0}{W} r^{\sigma} \tag{2.5}$$

A Gaussian beam changes its waist when interacting with a lens or a curved mirror. Since a beam is going through multiple reflections from curved mirrors in the Herriott cell we expect the beam waist and amplitude to vary with the Herriott cell modes. In order to achieve clear understanding of the changes in the beam amplitude with respect to the Herriott cell modes we divided the research in two. The first part we wanted to understand the change in the waist/width relation with the modes with perfect reflection $r = 1$. The seconde part we wanted to confirm that the change in amplitude coresponds to equation 2.5 with constant imperfect reflection $0 < r <= 1$

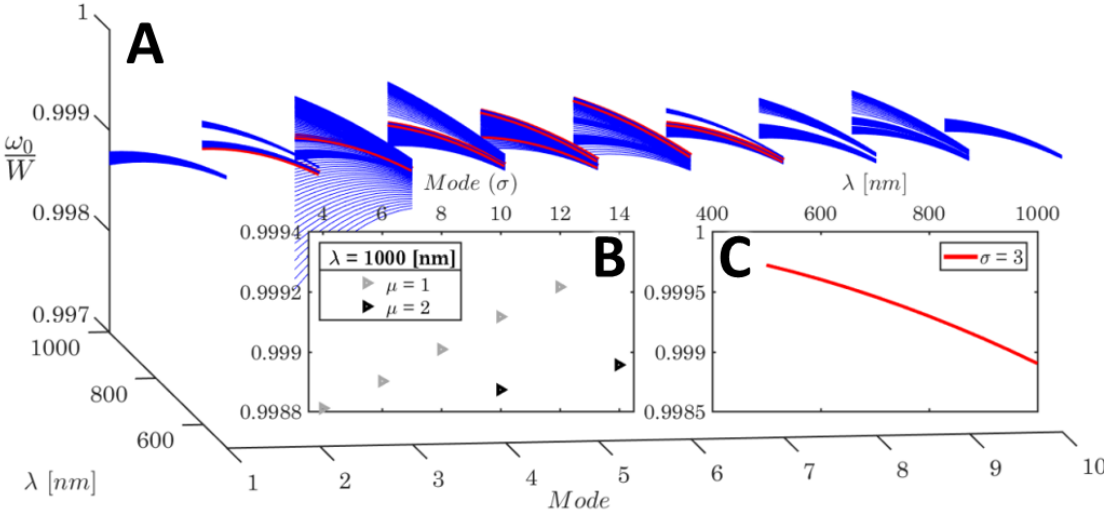

FIGURE 2.6: Typical Herriott cell output beam profile for Herriott cell with perfectly reflective mirrors ($r = 1$). Figure A is a three dimensional plot of the output beam $\frac{\omega_0}{W}$ relation with respect to the beam wavelength λ and the mode number σ. Blue lines represent all Herriott cell possible outputs and red lines represent a Herriott cell output of a specific alignment requirement. Figure B is a two dimensional cross section of figure A for a specific wavelength $\lambda = 1000nm$. Modes of order $\mu = 1$ are presented in gray triangles and modes of order 2 in black. Figure C is a cross section of figure A for a specific mode $\sigma = 3$. Figures B and C are typical representations of the wavelength and mode cross sections of figure A and demonstrate the ω_0/W dependency with respect to the Herriott cell modes and beam wavelengths.

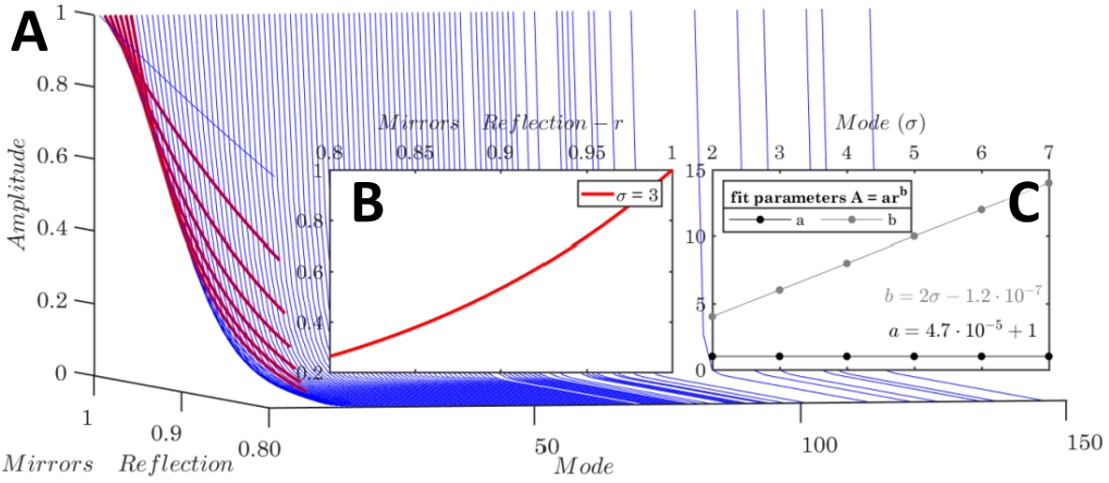

FIGURE 2.7: Typical Herriott cell output beam amplitude for Herriott cell for a specific wavelength $\lambda = 1000nm$. Figure A is a three dimensional plot of the output beam amplitude with respect to the mirrors r and the mode number σ. Blue lines represent all Herriott cell possible outputs and red lines represent a Herriott cell output of a specific alignment requirement. Figure B is a cross section of figure A for a specific mode $\sigma = 3$. Figure B is a typical representation of the amplitude dependency of the mirrors reflection for a given Herriott cell mode $A(\sigma, r) = ar(\sigma)^b$. Figure C present a summary of the fit parameters a, b with respect to the Herriott cell mode. A linear fit of these parameters confirms the assumption that $a = \frac{\omega_0}{W}$ and $b = 2\sigma$.

Beam Absolute Phase

A beam reflected from a mirror accumulate a phase. A flat dielectric mirror generate a phase of π. But a metalic mirror, similar to the mirrors we use for the Herriott cell, generate different phases for beams of different wavelength. We want to understand how much phase does a polychromatic Gaussian beam accumulate in the Herriott cell. In the simulation we used Drude model to evaluate the complex refractive index of the mirrors and the conclusions of section 1.4 to evaluate the the cumulative phase of a output beam from a Herriott cell. The Drude model parameters we used where taken from Ref.[25]. The beam does not only accumulate phase from the interaction with the mirrors but also from the distance it passes through the cell. In order to separate the pure mirror phase we define the phase as:

$$\chi(\sigma, \lambda) = \phi(\sigma, \lambda) - \frac{2\pi L(\sigma, d)}{\lambda} \tag{2.6}$$

The simulation generated a phase that don't follow a distinct trend. However, for most wavelengths, it's absolute value averages around π :

$$|\chi(\sigma, \lambda)| \simeq \pi$$

. That can be rectified by adding an extra planer mirror to the Herriott cell set-up, thus setting the phase to

$$|\chi(\sigma,\lambda)| \simeq 2\pi$$

.

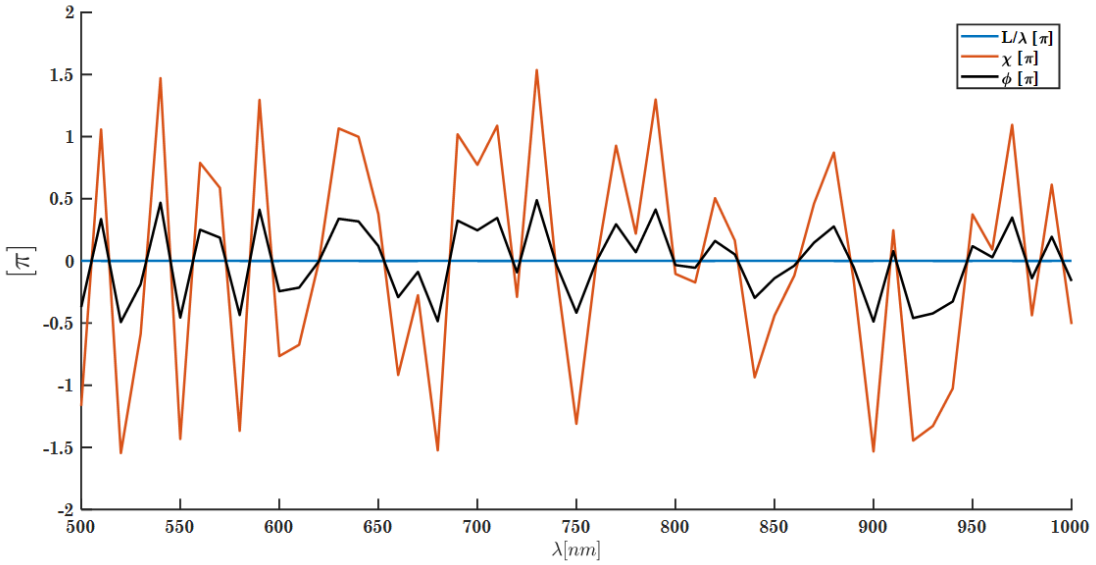

FIGURE 2.8: The phases generated in the Herriott cell at mode number $\sigma = 3$ with respect to the wavelength of the input beam. The phase generated from the optical path done in the cell is represented in blue. For simplicity, the phase presented is the reminder of $\frac{2*\pi L(\sigma,d)}{\lambda}$, it is significantly smaller then the other phases. The phase generated by the mirror's reflection $\chi(\sigma,\lambda)$ is presented in red. The total phase of EM field out of the Herriott cell $\phi(\sigma,\lambda)$ is presented in black .All phases are represented in units of π

Chapter 3. *Herriott FTIR*

In our research of the Herriott cell we found that it can be implemented as a long varying delay line for an optical system. An optical system that can greatly benefit from a long varying delay line is a FTIR spectrometer system. Embedding a Herriott cell inside the stationary arm of the FTIR and operating it in a multi-mode fashion can push the theoretical resolution limit of the FTIR while maintaining small footprint. That means that if we use the convention of naming the modes with index H so that the mode's OPD is sorted from low to high[1] :

$$L_{H+1} > L_H > d_H \tag{3.1}$$

The Herriott FTIR total OPD should be:

$$\vec{D}_{total} = \sum_{H=1}^{H_{max}} (L_H + \vec{D}) \tag{3.2}$$

Where $\vec{D}$ is the OPD of the delay arm and d_H is the cell size for mode H.

In this chapter we will try to understand how can a Herriott cell be integrated into a FTIR set-up and can a combination of steps substitute a continuous scan. Our investigation includes algorithms for calibration and combination of the Herriott cell modes and steps and analysis of the effects the Herriott cell have on the spectrum of a FTIR signal in monochromatic and polychromatic mode. We also present preliminary experimental results of proof of concept measurements in a Herriott FTIR in monochromatic light for testing the aforementioned algorithms and spectral analysis.

The proof of concept experiment is a measurement of a monochromatic light with a Herriott FTIR. The spectral function of a monochromatic light is a delta function. Therefore, the FWHM of the spectral line we will measure for a monochromatic light will be the minimal resolution of the instrument. Thus, the monochromatic light is chosen over polychromatic for the proof-of-concept simulation and experiment. Additionally,

[1] We don't use the mode number σ or cell size d_σ for naming the Herriott cell modes because they have a non-linear relation between those parameters and the mode OPD L_σ.

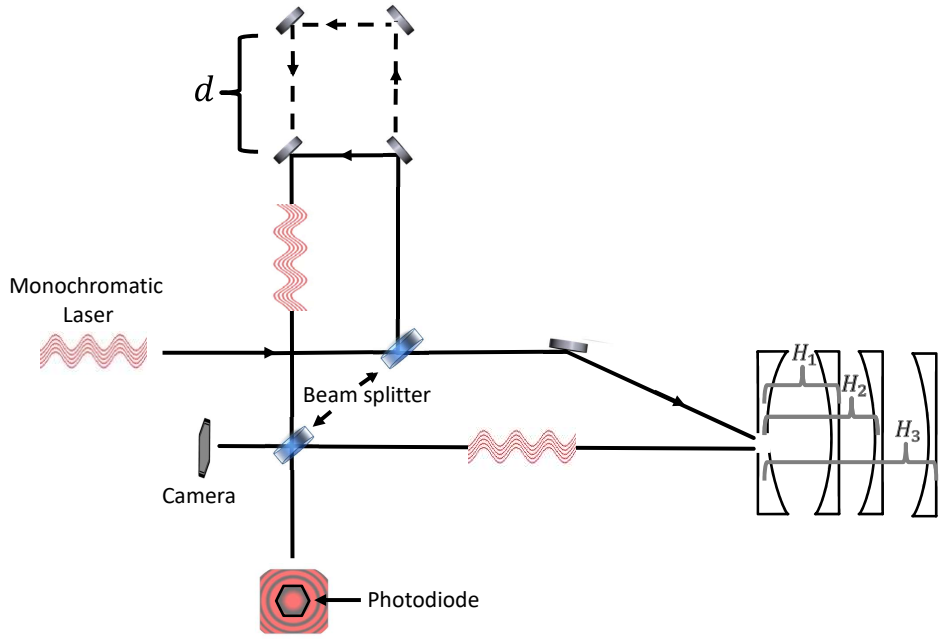

FIGURE 3.1: An illustration of the Herriott FTIR optical system for the proof of concept experiment.

testing the step combination algorithm requires a reference step. The reference step is a FTIR measurement with a single Herriott mode as a stationary arm and a full scan of the delay arm - $\vec{D}$. The main experiment is a partial scan of the delay arm $\vec{d}$ for different Herriott cell modes, so that the sum of all the Herriott FTIR steps is equal to the reference step.

$$\vec{D} = \sum_{H=1}^{H_{max}} (L_H + \vec{d}) \tag{3.3}$$

Under experimental constraints, we have chosen three Herriott cell modes for the proof-of-concept experiment.

3.1. *Herriott FTIR Unique Signal Processing*

The objective of a FTIR measurement is to obtain spectrum by Fourier transforming an interferogram. In this section, we will review the main challenges for receiving a spectrum from a Herriott FTIR and the way we cope with them in our signal processing algorithm.

The task of combining the Herriott FTIR step interferograms to a continuous interferogram without compromising its integrity is in the center of the Herriott FTIR concept. The challenges for combining steps are due to the cumulative effect of Herriott cell modes on the spectrum and step signal. The integrity of the interferogram is conserved if it maintains:

1. **A continuously changing Amplitude**.
   However, as we discussed in the previous chapter, the amplitude of the Herriott cell output beam is dependent of the mode. Thus, each Herriott FTIR step has a different amplitude around a different mean value.

2. **A constant sampling frequency**.
   However, the starting points of the steps are the OPDs of the Herriott cell modes. But, the difference between two Herriott cell mode OPDs $\Delta L = |L_2 - L_1|$ might not be consistent with the sampling frequency of the delay arm δd.

   $$\Delta L \neq N\delta d \tag{3.4}$$

   Where N is an integer.

3. **A continuously changing phase**.
   However, the phase accumulated in the Herriott cell is dependent of the mode. Therefore, the phase of the total interferogram does not change continuously.

   $$\chi_k = k(L + \phi_\sigma) \tag{3.5}$$

   Where χ_k is the phase accumulated in the Herriott cell for wavenumber k, L is the OPD of the Herriott cell mode σ and ϕ_σ is the mode dependent phase.

4. **A consistent spectrum distribution under Fourier transform**.
   However, the Herriott cell creates distortion in the spectral distribution.

In order to address these challenges we suggest a unique signal processing algorithm for the Herriott FTIR spectrometer.

The Herriott FT-IR signal processing algorithm is composed of three main sections:

1. **Global processing**
   Preparation of the steps for combination by setting the signal amplitude to one and mean value to zero and sorting the steps by OPD.

2. **Step combination algorithm**

   The main idea of the step combination algorithm is to use the overlapping OPD sections of two adjacent steps as a reference signal for the continuity of the sampling frequency and phase of the total interferogram. This stage is a cyclical process that gradually match the sampling and phase of the steps to the smallest OPD step. At each iteration the two smallest OPD steps are compared, the smallest OPD is named the first and it's adjacent the second.

   Sampling frequency conservation

   The first stage of the correction process is matching the sampling start positions by interpolating the second step's signal to a desired OPD that fulfil the requirement $\Delta L = N\delta d$. To so so, we find the first data point at the first step OPD -x_1- that correspond to the starting point of the second step OPD -x_2:

   $$x_1 - x_2 = \delta x \leq \delta d \tag{3.6}$$

   Then we shift the second step OPD to the first step OPD and interpolate the interferogram of the second step -$I_2(x)$- to match the new OPD using Shape-Preserving Piecewise Cubic Interpolation (PCHIP)[26].

   Phase conservation

   The second stage of the correction process is finding the phase shift between the steps and shifting the second step to match the first step. Since the spectrum is unknown, it is impossible to predict or calibrate the phase shift of the EM filed for each step. tHowever, the mode dependent phase can be treated as a constant spatial phase shift for each mode. Cross-correlation or cross-covariance of signals can find a constant time delay between two signals that overlap in time or space [27, 28]. Cross-Correlation of two signals $f(t), g(t)$ is defined as:

   $$(f \star g)(\tau) = \int_{-\infty}^{\infty} f^*(t)g(t+\tau)dt \tag{3.7}$$

   The Herriott FTIR steps are all identical signals that differ in space by the Herriott mode OPD L and phase ϕ_σ. For the combination of the steps we want to conserve the mode OPD and eliminate the mode phase. To do so, we choose the Herriott cell modes that have a small overlapping section between them so that:

   $$L_{H+1} = L_H + D - \delta \tag{3.8}$$

   Where D is the length of the delay arm and δ is the length of the overlapping section. At the overlapping section, the interferograms of both steps $\tilde{I}$ suppose to

be identical up to the mode phase difference $\Delta\phi_\sigma$:

$$\tilde{I}_{H+1} = \tilde{I}_H e^{-i\vec{k}\Delta\phi_{H,H+1}} \tag{3.9}$$

Where an interferogram at the overlapping section is marked as $\tilde{I}$.

The phase conservation part of the step combination algorithm finds the relative phase between two adjacent steps $\tilde{I}_{H+1}, \tilde{I}_H$ by finding the maximal value of the cross-correlation function $\rho_{H,H+1}$ (equation 1.19). The second step is then shifted to match the first step by adjusting it's OPD:

$$L_{H+1} \to L_{H+1} + \Delta\phi_{H,H+1} \tag{3.10}$$

Finally, the steps are combined to form a new longer step for the next iteration where it will be the first.

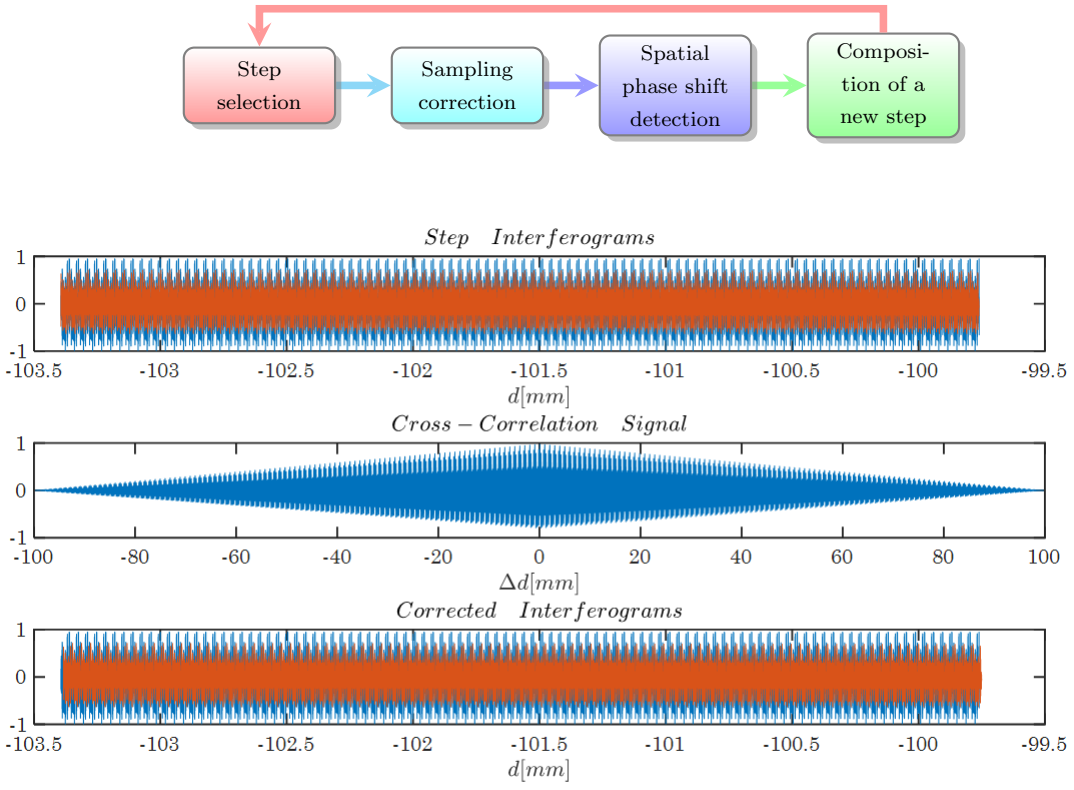

FIGURE 3.2: Example for phase conservation between two adjacent steps. The top figure present the overlapping OPD sections of both steps: the first step in blue and the second in red. The middle figure show the cross-correlation of the signals according to equation 3.7. The bottom figure present the first step and the shifted second step at the overlapping OPD section.

3. **Spectrum correction**

Initial spectrum can be calculated from the combined steps. However, it will be

distorted by the Herriott cell modes. Spectrum correction is done by multiplying the spectrum with the inverse spectral amplitude of the modes received by calibration .

$$\tilde{S}(k) = S(k)\tilde{A}^{-1}(k) \tag{3.11}$$

3.2. *Herriott Cell Calibration*

FTIR spectrometer requires regular scanning resolution. In order to operate a Herriott cell in a multi-mode fashion within the FTIR, the relative OPD of the Herriott cell should be consistent with the scanning arm resolution, therefore the Herriott cell must be calibrated inside the Herriott FTIR set-up. The calibration process of the Herriott cell is based on short pulse autocorrelation. In this process the input light is a short pulse Gaussian beam centred around wavelength $\bar{\lambda}$. After the beam is split, it passes through two different wavelength filters. One arm is low pass filtered - only wavelengths shorter then the center wavelength are passed on, and the second arm is high pass filtered - only wavelengths longer then the center wavelength are passed on. When the beams are recombined at the second beam-splitter they go through a BBO crystal cut to SHG of $\bar{\lambda}$ and measured with a spectrometer (see figure 3.3). The spectrum measured at the spectrometer is expected to contain both fundamental and SHG of both arms for any OPD, and the SFG of the beams only for $OPD \simeq 0$. The alignment of the system plays a crucial role in the calibration process since the specific mode formation of the Herriott cell is uniquely related to the output alignment. In order to repetitively control the mode selection of the cell a camera is positioned at the second recombination of the beams. Later on, the camera is used to confirm the mode selection and system alignment while operating the Herriott FTIR mesurments.

The proposed calibration process is able to calibrate modes only for $L <= d_{max}$, overcoming this obstacle requires temporary additional length to the delay arm. Our solution is to split the calibration sequence to sets of calibration iterations. At each calibration iteration the delay arm is maximize, then a fixed arm of length $D = d_{max}$ is added to the delay arm. Every extension is zeroed by a second pulse-autocorrelation in order to validate the real $d = 0$ of the delay arm as presented at the flow chart.

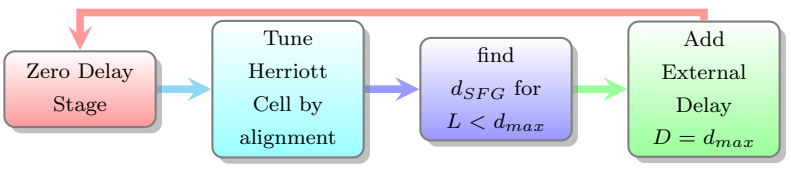

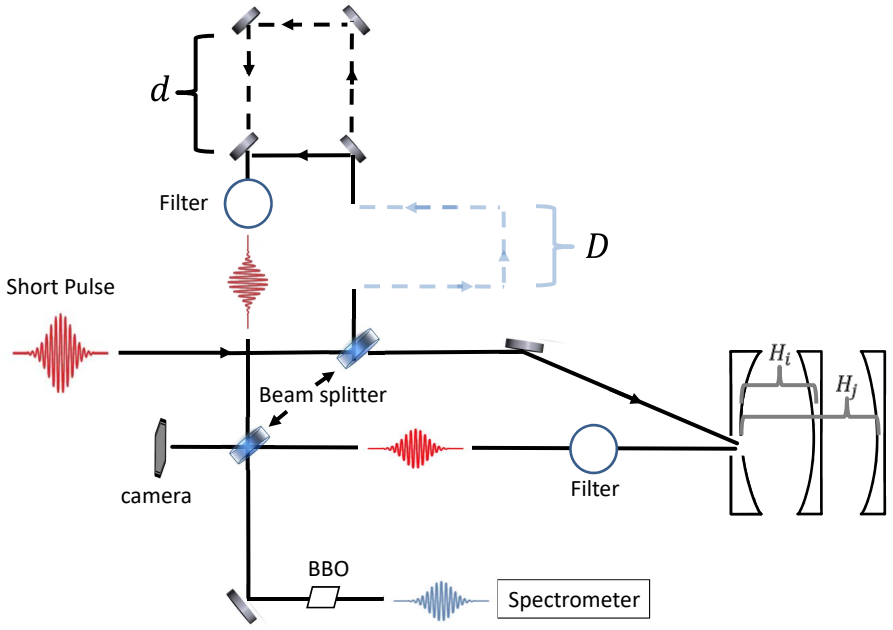

FIGURE 3.3: An illustration of the Herriott cell calibration set-up within the Herriott FTIR optical system

$Mode(\sigma)$	Cell Size [mm]	OPD [mm]
7	35	127.7281 ± 0.1708
6	50	221.5103 ± 0.1871
5	75	342.2696 ± 0.1794

TABLE 3.1: Herriott FTIR calibration results

The OPD of a mode was determined by fitting the SFG signal to a Gaussian distribution in space

$$I = I_0 e^{-\frac{(d-L)^2}{2\Delta L^2}} \tag{3.12}$$

where the center L is the OPD value of the mode and the FWHM ΔL is the measurement error.

The process was done several times for each mode and was shown to be repeatable up to the measurement error. An example of the results for one of the proof of concept mesurments is a three mode Herriott FTIR as presented in table 3.1, the rest of the results are in appendix E.

3.3. *Herriott FTIR Simulation Results*

The Herriott FTIR simulation is a tool we designed to predict the experimental results of a Herriott FTIR spectrometer for the purpose of testing the step combination process and to lay the groundwork for the analysis of the experimental data. Therefore, similar to the Herriott cell simulation, the Herriott FTIR simulation take into account all of the optical system parameters.

Simulation Validity Test

The validity of the simulation must be tested before it can be used for any conclusions and predictions. The simulation was tested for:

1. Maintenance of the theoretical resolution limit for FTIR without a Herriott cell for a monochromatic light.

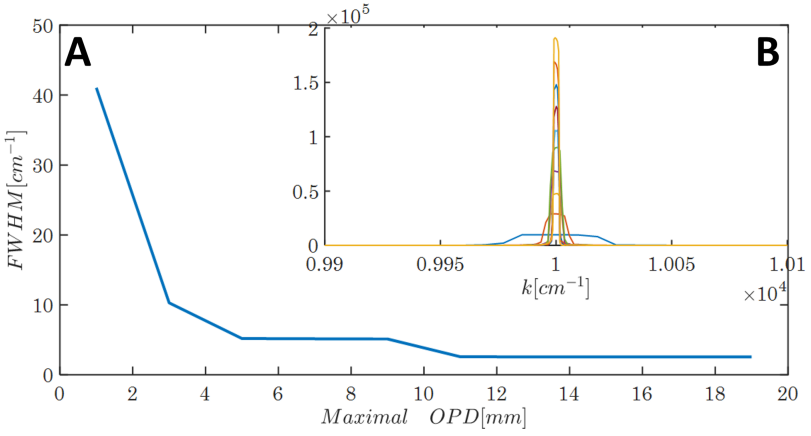

FIGURE 3.4: Summery of FTIR without Herriott simulation for a Gaussian beam with wavelength of $\lambda = 1000nm$ for maximal OPD of 1-20 mm. Figure B present the spectrum around the central frequency $k_0 = 1000cm^{-1}$. Figure A present the FWHM of the spectrum for each maximal OPD scan of the FTIR.

2. Re-contraction of a polychromatic light with prefect mirrors ($r = 1$).

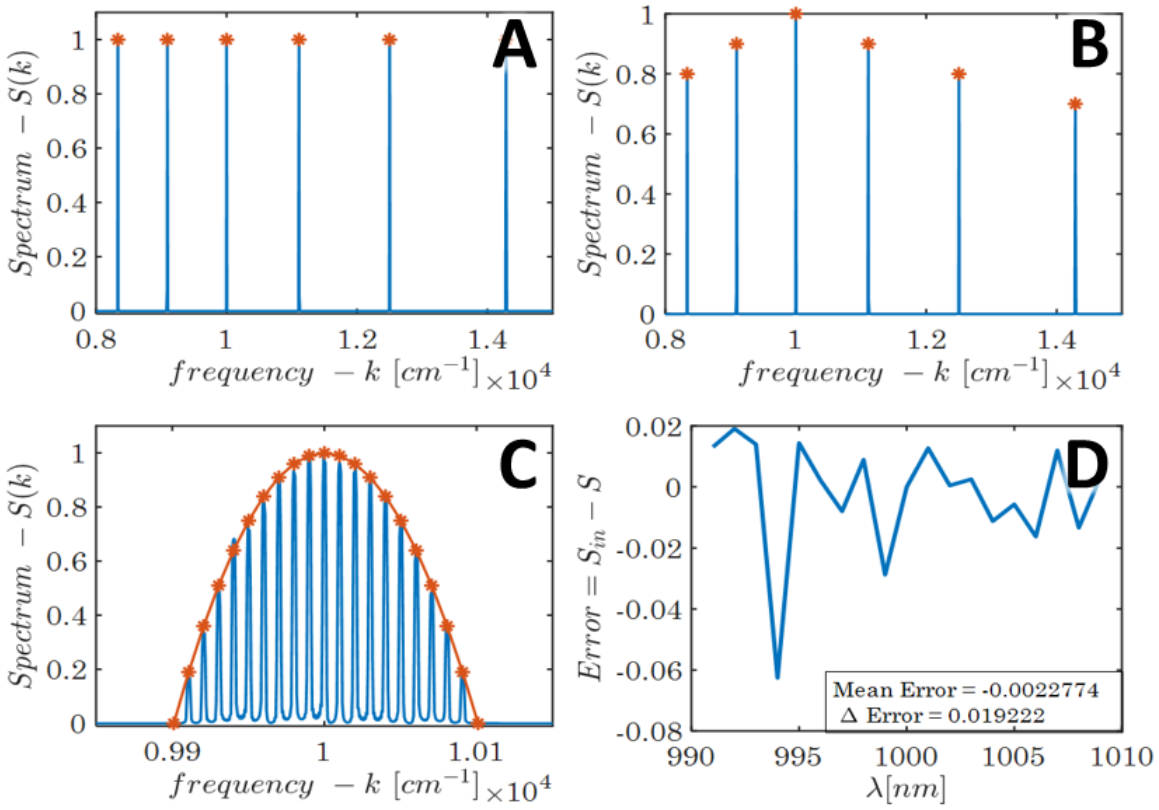

FIGURE 3.5: Summery of the Re-contraction test of the FTIR simuletion for poly chromatic light. Figure A present reconstruction of polychromatic light with constant amplitude $S(k) = 1$. Polychromatic light with wavelength dependent amplitude $S(k)$ is presented in figure B (wide frequency rang: $700 - 1200nm$) and figure C (narrow frequency rang: $990 - 1010nm$). The difference between the input and output amplitudes is presented as variable $Error = S_{in}(k) - S(k)$ in figure D.

Figures 3.4 and 3.5 demonstrate that the FTIR simulation is a good representation of a FTIR optical system, by showing that it reasonably reconstruct the spectrum of an input polychromatic light and is consistent with the theoretical resolution limit.

Herriott Cell effects on a FTIR spectrum

In the previous chapter, we investigated the effects of a Herriott cell on a Gaussian beam. The characterization of Herriott cell effects on a FTIR spectrum is done gradually with rising complexity. The spectrum is examined after global processing alone, in order to highlight the contribution of the Herriott cell modes to the spectrum. The Herriott cell is inserted to the FTIR simulation in three stages:

1. perfect reflection - $r = 1$
2. real, wavelength dependent, reflection $r = r(\lambda) \in \mathbb{R}$.
3. complex, wavelength dependent, reflection $r = r(\lambda) \in \mathbb{C}$.

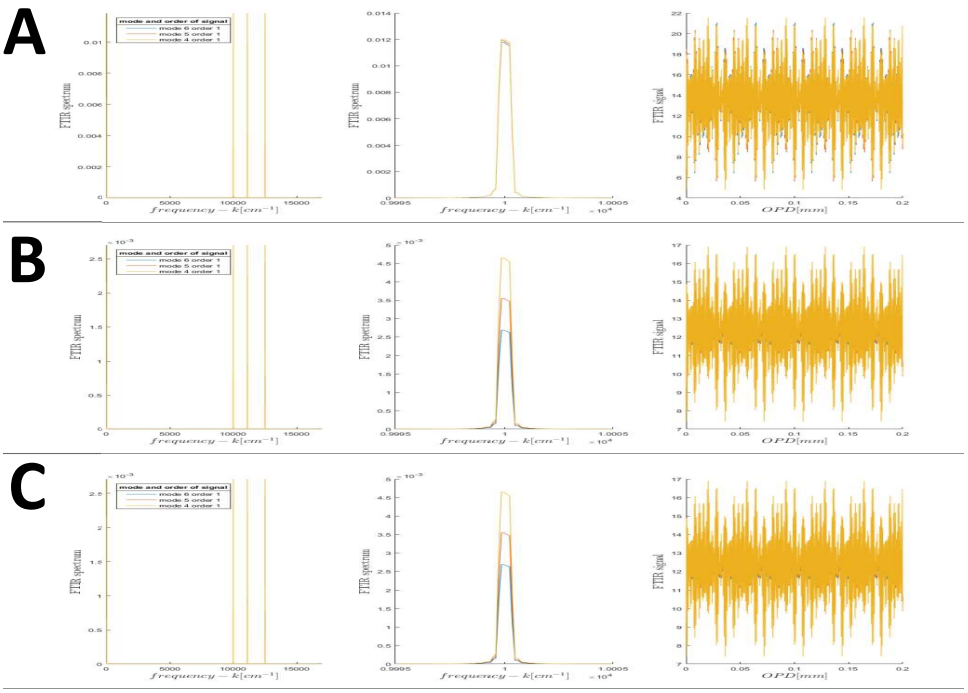

FIGURE 3.6: FTIR simulation with a Herriott cell at the stationary arm. Figures A,B and C compare the raw FTIR spectrum of three 50 mm scan steps for monochromatic light with wavelength $\lambda = 1000nm$. Figure A is a demonstration of FTIR with perfect mirrors $r = 1$. Figure B is a demonstration of FTIR with dielectric mirrors $r = r(\lambda) \in \mathbb{R}$, where the values for $r(\lambda)$ are the real part of a gold mirror reflection. Figure C is a demonstration of FTIR with gold mirrors $r = r(\lambda) \in \mathbb{C}$, where the values for $r(\lambda)$ are calculated form 1.4.

Figure 3.6 shows the main difference between a FTIR spectrometer and a Herriott FTIR spectrometer. Multiple reflection of the Herriott cell mirrors change the amplitude of the step spectrum, this might cause distortion in the spectrum at the step combination stage.

Step Combination Test

The step combination process was tested for a proof of concept Herriott FTIR set-up, three steps where chosen: $\sigma = 6, 5, 4$ for a $180mm$ scan length. With accordance to the experimental set-up, all flat mirrors are coated in silver and the Herriott cell mirrors are coated in gold. After subtraction of the OPD overlap sections between the steps, the maximal OPD of the Herriott FTIR is 480 mm. Therefore, a reference FTIR of the same maximal OPD was simulated for comparison in order to test the effects of the step combination process on the Herriott FTIR spectrum. Figure 3.7 shows the similarity of the Herriott FTIR resolution-MOPD relation to the standard FTIR resolution-MOPD relation for monochromatic light. Therefore, we conclude that the step combination process dose not add significant diversions to the effective interferogram and is equal to a continuous interferogram.

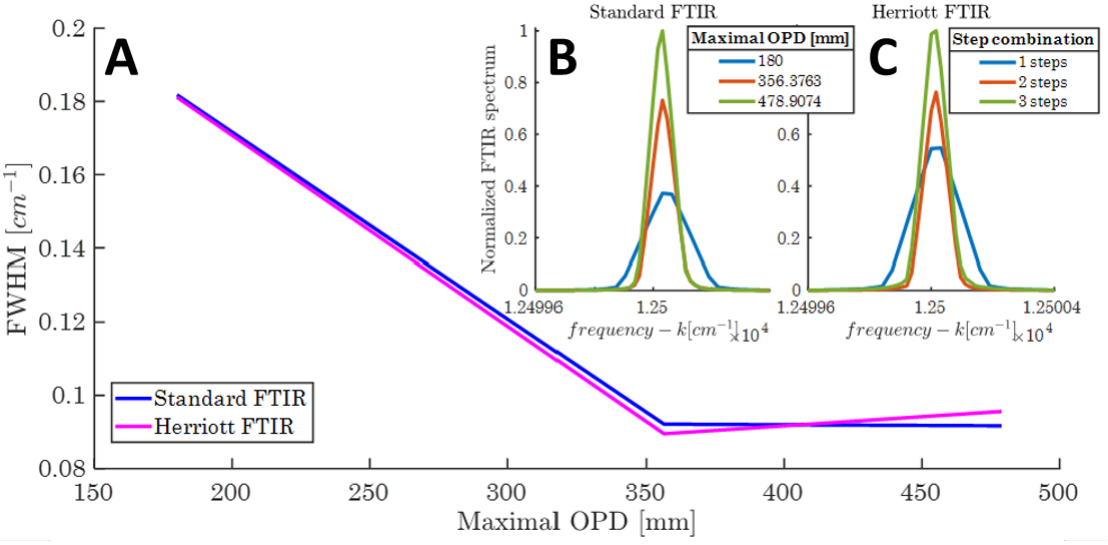

FIGURE 3.7: Summery of the proof-of-concept simulation for monochromatic light. Comparison of the FTIR spectrum for different maximal OPDs is presented at the top figures. The Herriott FTIR spectrum (figure C) is presented by number of steps combinations: a single step in blue, two steps in red and all three steps in green. The reference FTIR (figure B) is cut to match the Herriott FTIR step combination's maximal OPD. The FWHM relation to the maximal OPD of the simulations is presented at figure A: The reference is plotted in blue and the Herriott FTIR in magenta.

Amplitude Calibration

The spectrum correction process demesnes amplitude calibration for the combined steps spectrum. Polychromatic light with a constant amplitude was inserted to the proof of concept simulation in order to understand the the effects the Herriott cell combined modes have on the FTIR spectrum.The amplitude calibration for the simulated wavelengths is the result of comparing the spectral amplitude distribution of the Herriott FTIR spectrum to the reference spectrum. An example of the simulation is presented in figure 3.8 for $\lambda = 800, 900, 1000nm$.

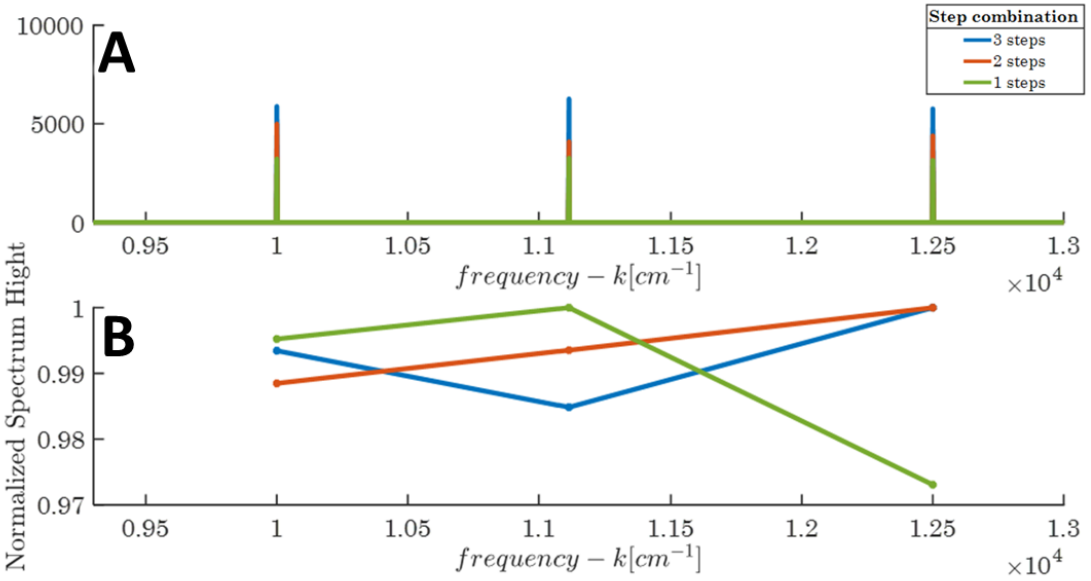

FIGURE 3.8: Spectral amplitude comparison of spectral lines $(k = 1.25 \cdot 10^4, 1.11 \cdot 10^4, 1 \cdot 10^4 cm^{-1})$ corresponding to $\lambda = 800, 900, 1000nm$ for Herriott FTIR simulation with different step combinations to input amplitude $A(k) = 1$. The spectral lines for each step combination are presented at figure A and the normalized peaks per step are presented at figure B. In these figures, one step spectrum is in green, two steps in red and three steps in blue.

3.4. *Herriott FTIR Preliminary Experimental Results*

We have conducted two experiments in a Herriott FT-IR proof-of-concept set-up in order to confirm the simulation results. A monochromatic light was chosen for the experiment because its spectrum is a delta function. Therefore, the FWHM of the FT-IR spectrum should be the resolution limit of the instrument.

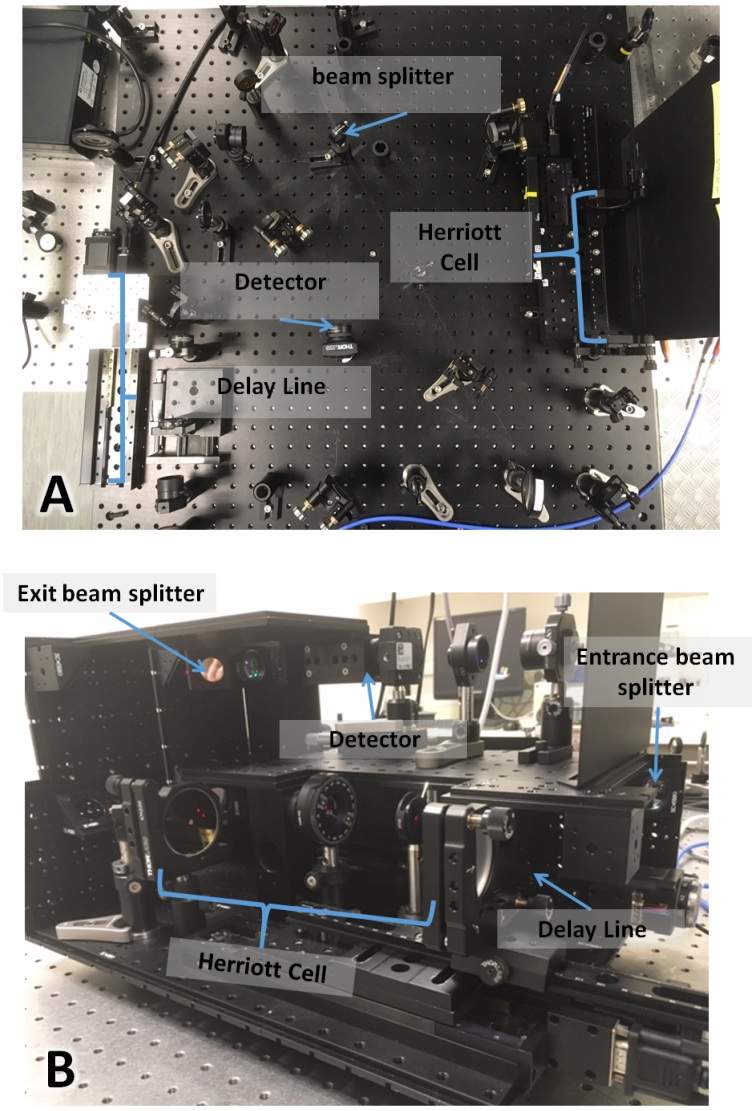

FIGURE 3.9: Pictures of the experimental set-ups, the set-up for (A) the HeNe experiment and (B) the 780 nm experiment

HeNe

The first experiment was a preliminary test for the proof-of-concept simulation. It was conducted with a HeNe laser with a $\lambda = 632.9nm$ central spectral line with width of approximately $\Delta\lambda = 1nm$. The Herriott cell modes chosen for the experiment are $\sigma = 7, 5, 4$ with scans of $120mm$ for step. The results are similar to the simulation results but the sp The Herriott FT-IR spectrum was not clean enough to deduce a clear resolution limit for the instrument, mostly due to insufficient measurements. A rough estimation of the resolution limit was made using the envelope of the spectral line and fitting it into a Gaussian function. The FWHM of the Gaussian fits show some similarity to the simulation results. These results also indicated that the spectral width of the HeNe laser is not narrow enough to be considered as a delta function comparing to the resolution limit.

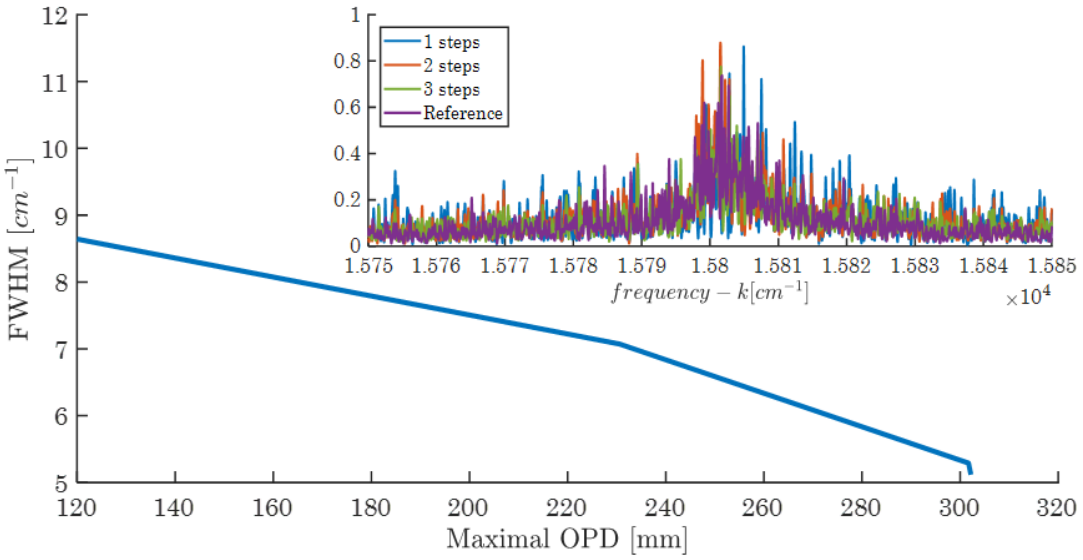

FIGURE 3.10: Summary of Herriott FTIR proof-of-concept experiment with HeNe laser. The Herriott FT-IR step combination results are presented on the top right figure. The spectrum is presented in 1,2 and 3 steps combination and a reference step. The Gaussian fits for the spectrum envelops are also presented in the figure. The large figure plot the FWHM relation to the maximal OPD of the steps and the reference.

780 nm

The second experiment was conducted with a 780 nm laser source with spectral width of $\delta\lambda \simeq 10^{-9}nm$ and a mechanically upgraded se-up. The Herriott cell modes chosen for the experiment are $\sigma = 7, 6, 5$ (table 3.1) with scans of $180mm$ for step. Although enough measurements were conducted in order to deduce clear spectrum, the resolution limit of the instrument can not be observed due to an upper bound on the spectral resolution. We assume that the restriction on the resolution is due to mechanical noise and more experiments are to be conducted in the future. Figure 3.11.B demonstrates the upper bound on the Herriott FTIR spectral resolution in this experiment. Presenting the normalized spectrum of all of the step combinations and the reference measurement, shows that the hight and width of all of the spectral lines are identical.Therefore, these results do not comply to the FTIR size-resolution relation.

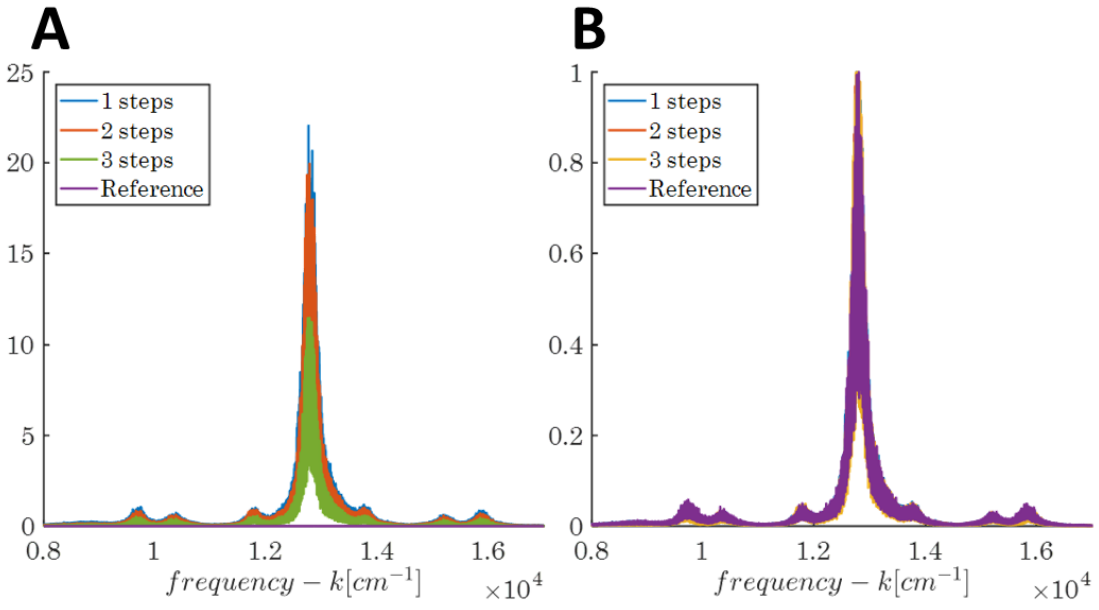

FIGURE 3.11: Summary of Herriott FTIR proof-of-concept experiment with HeNe laser. The Herriott FT-IR step combination results are presented on the top right figure. The spectrum is presented in 1,2 and 3 steps combination and a reference step. The Gaussian fits for the spectrum envelops are also presented in the figure.

Summery and further outlook

This work presented a characterization of the Herriott cell and it's implementation as a part of FT-IR spectrometer.

The main conclusion from the Herriott cell characterization research, is that the Herriott cell can be used in a multi-mode fashion within an optical system. This conclusion is derived from four main characteristics we found for the Herriott cell. First, the Herriott cell conserve a Gaussian beam's size. Second, a set of Herriott cell modes can always be chosen to conserve the alignment of an optical system. Third, the unconserved beam properties - phase and amplitude- can be calibrated to fit an optical system connected to a Herriott cell. Last, the OPD done by the Herriott cell can be reduced to an simple equation that depend on the mode number, cell size and initial conditions alone. This equation was confirmed by a numerical simulation and experiment. Additionally, We designed a calibration algorithm that successfully finds the OPD done by the Herriott cell with relation to an external optical system. Our results on the Herriott cell complete Herriott's work [19, 20] to full characterization of the resonator: The cell by itself and the interaction of a Herriott cell with an external optical system.

The numerical simulation of the Herriott FT-IR predicts that a well calibrated Herriott cell can be used as an extension for a FT-IR system. The simulation for monochromatic proof-of-concept Herriott FT-IR successfully reconstructs spectrum and show that our step combination process does not significantly alter the theoretical size-resolution relation of a Fourier transform based spectroscopy. Our polychromatic calibration simulation emphasizes the need for amplitude calibration for polychromatic Herriott FT-IR spectrometer.

Our preliminary experimental results of a monochromatic proof-of-concept FT-IR are inconclusive. The interferograms and reconstructed spectrum of the HeNe experiment have a low signal to noise ratio and cannot be used for an significant conclusion. However, rough analysis of the experiment implies that the theoretical size-resolution relation of a FT-IR spectrometer is conserved. Additionally, the reconstructed spectrum have a spectral width of $\approx 10^{-1}nm$. Therefore, the spectral width of the HeNe ($\approx 1nm$) is not

narrow enough to fully observe the resolution limit of the Herriott FTIR. The second experiment was conducted with a laser source that has a much narrower spectral width. The $780nm$ laser experiment did not confirm the result of the simulation and HeNe experiment. The spectral width of the reconstructed spectrum was $\approx 5nm$, significantly wider then the spectral width of the previous experiment and the source ($\approx 10^{-9}nm$). Therefore, we conclude that the results are still not conclusive. We suspect that the high signal to noise ratio (SNR) that we experienced was due to mechanical noise setting an upper limit on the instrument's resolution and distorted the results.

In the future, we plan to recreate the experiment with technical improvements, in order to achieve clear results. Additionally we want to test the calibration for polychromatic Herriott FTIR i.e gain amplitude calibration for white light. Furthermore the conclusions of the Herriott FT-IR can open the possibility for connecting other multi-pass cells with FT-IR system on the condition they, too, conserve beam size and alignment. Currently, we examine the White cell as an alternative to the Herriott cell as a multi-pass cell in a FT-IR reference arm. To do so, we have designed a new comparison and proof-of-concept experiment for the Herriott/White FT-IR's with a polychromatic source. In this experiment, we will replace the reference arm of a FT-IR' base set-up with three OPD's produced by Herriott cell modes and a White cell modes. The control experiment will include a repetition of the experiment with three standard references and a repetition of this experiment with a monochromatic source.

Appendix A. *Interferometric Autocorrelation Intensity for SFG*

This appendix present the full derivation of the autocorrelation Intensity for an interferometric autocorrelation of a pulse split into two frequency components and re-converge collinearity at a nonlinear crystal with up-convertion phase matching conditions as presented at section 1.5. The pulses are oscillating at two different frequencies : ω_1, ω_2 and are delayed at τ in time.

$$\begin{aligned} \vec{E}_1(t) &= \vec{A}_1(t)e^{-i\omega_1 t} + C.C \\ \vec{E}_2(t-\tau) &= \vec{A}_2(t-\tau)e^{-i\omega_2(t-\tau)} + C.C \end{aligned} \tag{A.1}$$

The EM wave in the crystal is:

$$\vec{E}_{total} = \vec{E}_1(t) + \vec{E}_2(t-\tau) + C.C \tag{A.2}$$

and the autocorrelation intensity is:

$$I_{AC}(\tau) = \int_{-\infty}^{\infty} |[\vec{E}_1(t) + \vec{E}_2(t-\tau)]^2|^2 dt \tag{A.3}$$

Let us simplify the terms in the integral of the autocorrelation intensity:

$$\begin{aligned} |[\vec{E}_1(t) + \vec{E}_2(t-\tau)]^2|^2 =& [E_1^2 + E_2^2 + 2E_1E_2][E_1^{*2} + E_2^{*2} + 2E_1^*E_2^*] \\ &= |E_1^2|^2 + |E_2^2|^2 + 4|E_1|^2|E_2|^2 \\ &+ E_1^2E_2^{*2} + 2E_1^2E_1^*E_2^* \\ &+ E_2^2E_1^{*2} + 2E_2^2E_1^*E_2^* \\ &+ 2E_1E_2E_1^{*2} + 2E_1E_2E_2^{*2} \end{aligned} \tag{A.4}$$

Inserting A.1 into A.4 reviles the frequency of each term:

$$|E_1^2|^2 \sim \quad I^2(2\omega_1^2) \tag{A.5}$$

$$|E_2^2|^2 \sim \quad I^2(2\omega_2^2) \tag{A.6}$$

$$|E_1|^2|E_2|^2 \sim I_1 I_2 \sim \quad I(\omega_1 + \omega_2) \tag{A.7}$$

$$E_1^2 E_2^{*2} = (E_2^2 E_1^{*2})^* = A_1^2 e^{-i2\omega_1 t} A_2^{*2}(t) e^{i2\omega_2 t} \sim \quad I(2(\omega_1 - \omega_2)) \tag{A.8}$$

$$E_1^2 E_1^* E_2^* = (E_1 E_2 E_1^{*2})^* = A_1^2 A_1 A_2^* e^{-i(\omega_1 - \omega_2)t} \sim \quad I(2\omega_1) I(\omega_1 - \omega_2) \tag{A.9}$$

$$E_2^2 E_1^* E_2^* = (E_1 E_2 E_2^{*2})^* = A_2^2 A_1^* A_2 e^{i(\omega_1 - \omega_2)t} \sim \quad I(2\omega_2) I(\omega_1 - \omega_2) \tag{A.10}$$

Since the phase matching conditions do not support DFG, terms A.8-A.10 are eliminated, and the autocorrelation intensity at $\tau = 0$ is:

$$I_{AC} = \int_{-\infty}^{\infty} I_1^2(t) + I_2^2(t) + I_1(t) I_2(t) dt \tag{A.11}$$

Adding time delay τ between the pulses produce equation 1.38

$$I_{AC}(\tau) = \int_{-\infty}^{\infty} \overset{SHG^1}{I_1^2(t)} + \overset{SHG^2}{I_2^2(t-\tau)} + I_1(t) \overset{SFG}{I_2(t-\tau)} dt$$

Herriott Cell Mode Shape

In this appendix we present some pictures of the Herriott cell's modes from our experiment with a HeNe laser. As discussed in section 2.1, the Herriott cell modes are controlled by the size of the cell and differ in the number of transverses in the cell and can be counted on the face of the back mirror. Figure A.1 present a Herriott cell in mode number $\sigma = 3$ with a description of the Herriott cell components. Figures A.2- A.4 show other Herriott cell modes from the same set-up at different cell sizes. Figures A.5-A.6 show the mode shapes on the back mirror face at different modes with no particular order.

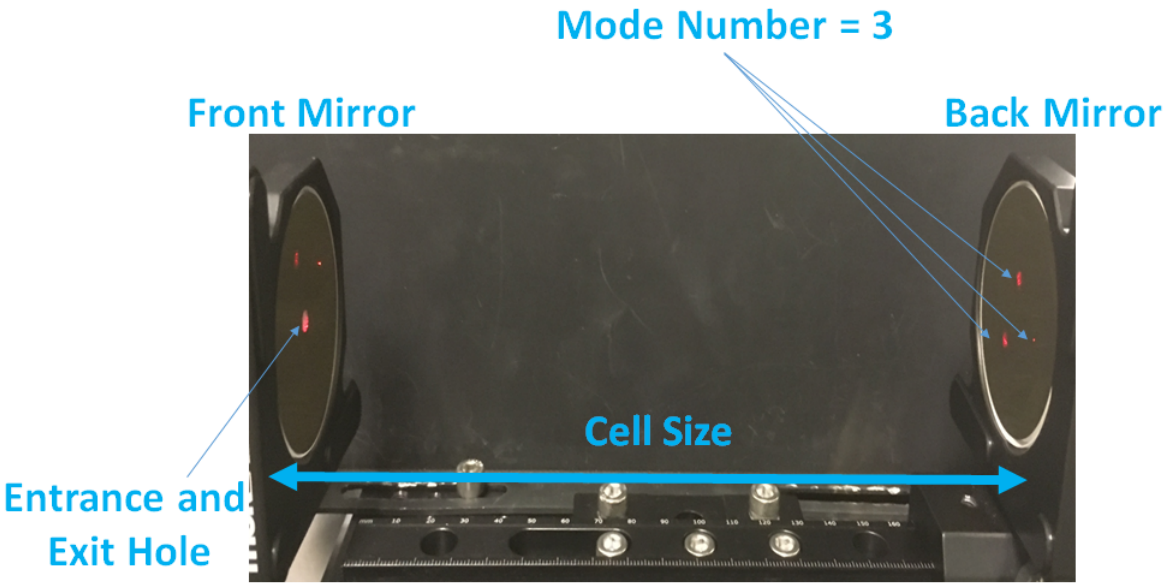

FIGURE A.1

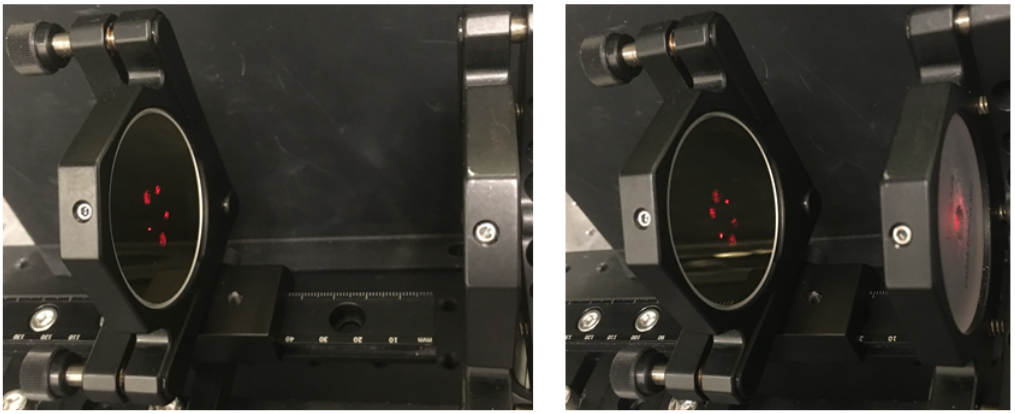

FIGURE A.2

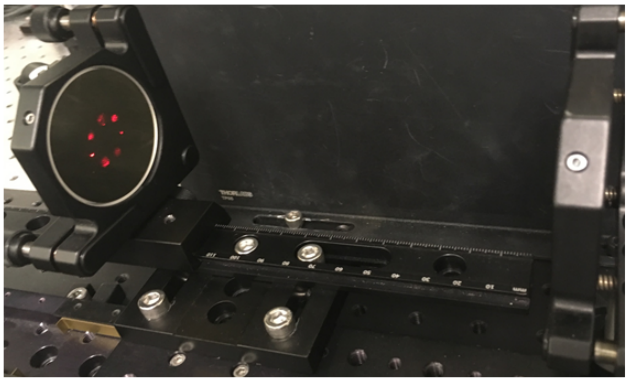

FIGURE A.3

FIGURE A.4

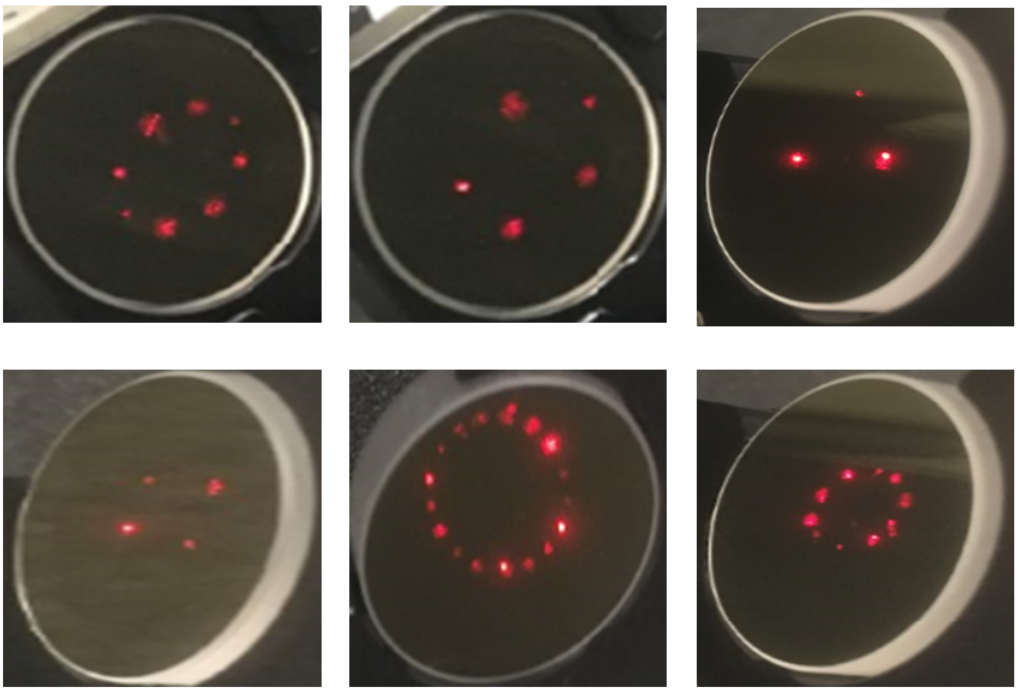

FIGURE A.5

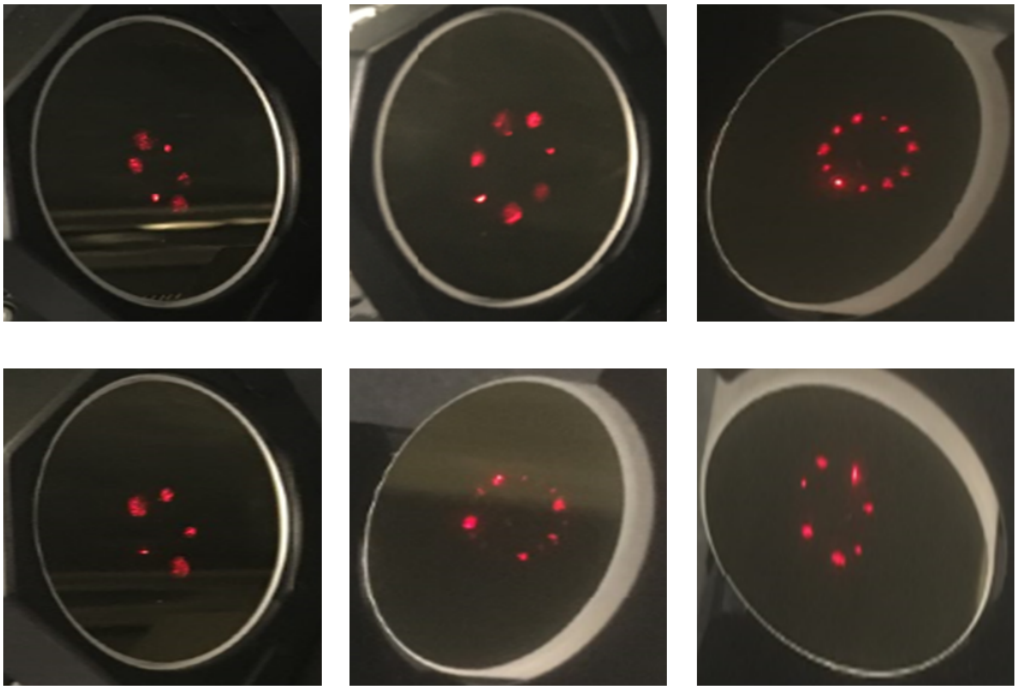

FIGURE A.6

Appendix B. *Herriott cell Formula*

Herriott provided the ellipses exact shape A, B and location (x_n, y_n) at each iteration n for mode σ at cell size d for a symmetric Herriott cell with curved mirrors of focal length f. In this work we are also interested in the total optical path preformed in the cell L or OPD, i.e L as a function of σ, d and initial conditions f, x_0, x'_0.

The optical path performed in the cell at each iteration is a three dimensional norm:

$$d_n = \sqrt{d^2 + \Delta x_n^2 + \Delta y_n^2} \tag{B.1}$$

$$\begin{cases} \Delta x_n = x_n - x_{n-1} \\ \Delta y_n = y_n - y_{n-1} \end{cases} \tag{B.2}$$

Where $n = 0$ case is the start condition for the cell.

The total optical path performed in the cell at a specific mode is

$$L_\sigma = \sum_{n=1}^{2\sigma} d_n \tag{B.3}$$

Simplifying this equation require some assumptions, the relevant assumptions for the type of Herriott cell we will use for the Herriott FTIR are:

1. The cell's size is much grater then the cell's mirrors i.e $\frac{\Delta x_n}{d}, \frac{\Delta y_n}{d} << 1$
2. The initial conditions support the relation $\alpha \simeq 2\beta$
3. The initial conditions support the relation $A \approx B$

Using assumption 1 and taking leading order of Taylor series we can simplify B.1:

$$\begin{aligned} d_n &= \sqrt{d^2 + \Delta x_n^2 + \Delta y_n^2} \\ &= d\sqrt{1 + \frac{\Delta x_n^2 + \Delta y_n^2}{d^2}} \\ &\simeq d\left(1 + \frac{1}{2}\frac{\Delta x_n^2 + \Delta y_n^2}{d^2}\right) \end{aligned} \tag{B.4}$$

Simplify the term $\Delta x_n^2 + \Delta y_n^2$ by using assumptions 2:

$$\begin{cases} \Delta x_n^2 = [Asin(n\theta + \alpha) - Asin((n-1)\theta + \alpha)]^2 \\ \Delta y_n^2 = [Bsin(n\theta + \frac{1}{2}\alpha) - Bsin((n-1)\theta + \frac{1}{2}\alpha)]^2 \end{cases} \tag{B.5}$$

Using the identity: $sin\theta - sin\varphi = 2cos\left(\frac{\theta+\varphi}{2}\right) sin\left(\frac{\theta-\varphi}{2}\right)$

We can simplify B.5:

$$\begin{aligned} \Delta x_n^2 &= [(n\theta + \alpha) - Asin\left((n-1)\theta + \alpha\right)]^2 \\ &= 4A^2 sin^2\left(\frac{\theta(n-1) - \theta n}{2}\right) cos^2\left(\alpha + \frac{\theta(n-1) + \theta n}{2}\right) \\ &= 4A^2 sin^2\left(\frac{\theta}{2}\right) cos^2\left(\alpha + \theta n - \frac{\theta}{2}\right) \\ \Delta y_n^2 &= 4B^2 sin^2\left(\frac{\theta}{2}\right) cos^2\left(\frac{1}{2}\alpha + \theta n - \frac{\theta}{2}\right) \end{aligned} \tag{B.6}$$

Summing over all iterations at mode σ

$$\begin{aligned} \sum_{n=1}^{2\sigma} cos^2\left(\alpha + \theta n - \frac{\theta}{2}\right) &= \sigma + \frac{1}{4sin\theta}\left[sin(2(\alpha - \frac{\theta}{2}) + 4\sigma\theta + \theta) - sin(2(\alpha - \frac{\theta}{2}) + \theta)\right] \\ &= \sigma + \frac{1}{4sin\theta}\left[sin(2\alpha + 4\sigma\theta) - sin(2\alpha)\right] \end{aligned}$$

but the condition for mode existence is $2\sigma\theta = 2\pi\mu$ so

$$[sin(2\alpha + 4\sigma\theta) - sin(2\alpha)] = [sin(2\alpha) - sin(2\alpha)] = 0$$

and

$$\sum_{n=1}^{2\sigma} cos^2\left(\alpha + \theta n - \frac{\theta}{2}\right) = \sum_{n=1}^{2\sigma} cos^2\left(\frac{1}{2}\alpha + \theta n - \frac{\theta}{2}\right) = \sigma \tag{B.7}$$

Returning to B.3 with B.4,B.6,B.7 we get

$$\begin{aligned} L_\sigma &= \sum_{n=1}^{2\sigma} d_n = \sum_{n=1}^{2\sigma} d\left(1 + \frac{1}{2}\frac{\Delta x_n^2 + \Delta y_n^2}{d^2}\right) \\ &= 2d\sigma + \frac{1}{2d}\sum_{n=1}^{2\sigma} \Delta x_n^2 + \Delta y_n^2 \\ &= 2d\sigma + \frac{1}{2d}\left[4A^2 sin^2\left(\frac{\theta}{2}\right)\sigma + 4B^2 sin^2\left(\frac{\theta}{2}\right)\sigma\right] \\ &= 2d\sigma + \frac{2\sigma(A^2+B^2)}{d} sin^2\left(\frac{\theta}{2}\right) \end{aligned}$$

Assuming $A \approx B$, we get

$$L_\sigma = 2d\sigma + \frac{4\sigma A^2}{d} sin^2\left(\frac{\theta}{2}\right) \tag{B.8}$$

We can also use $sin(cos^{-1}(x)) = \sqrt{1-x^2}$ and $cos(\theta) = 1 - \frac{d}{2f}$ to receive:

$$L(\sigma, d) = 2d\sigma + \frac{\sigma A^2}{d}\left(3 + \frac{d}{f} - \frac{d^2}{4f^2}\right) \tag{B.9}$$

Appendix C. *Herritt Cell Output Beam Amplitude*

Section **??** (Herriott cell: beam amplitude) present the conclusions of our simulation research on the Herriott cell output beam amplitude and profile. Here we present the supporting background for those conclusions:

Waist to width ratio

The amplitude of a Gaussian beam is dependent of the ratio between the waist of the beam -ω_0 - and the width of the beam -W. Since the waist of the Gaussian beam is dependent of the wavelength, a simulation of the Herriott cell was conducted for different wavelengths $\lambda = [500, 550..1000]nm$ and the waist to width ratio was compared between different wavelengths at different Herriott cell modes (figure 2.6). In order to understand the amplitude dependency of the output beam with the wavelength and mode we fitted the amplitude (or waist to width ration of the beam) for:

1. the mode for every beam wavelength
   Figures (C.2-C.6) present the amplitude cross section for mode at multiple wavelengths. Figure C.2 on the right show all mode cross sections of $\frac{\omega_0}{W}$ for different wavelengths. The rest of the figures (C.2 (left)-C.5) present $\frac{\omega_0}{W}$ fits for wavelength, $\frac{\omega_0}{W} = a\lambda^2 + b\lambda + c$. Description of the fitted equation are presented on the fits and a summery of the fit parameters a and b are presented on figure C.6.

2. the wavelength of the beam for every mode
   Figures (C.7-C.13) present the amplitude cross section for wavelength at multiple modes. Figure C.7 on the right show all mode cross sections of $\frac{\omega_0}{W}$ for different modes. The rest of the figures (C.7 (left)-C.12) present $\frac{\omega_0}{W}$ fits for modes of order 1, $\frac{\omega_0}{W} = a\lambda + b$. Description of the fitted equation are presented on the fits and a summery of the fit parameters a and b are presented on figure C.13.

Mirrors Reflection

The amplitude of the Herriott cell output beam is effected by the reflection of the

output mirrors. Theoretically, for any mode σ for a Herriott cell with mirrors that have reflection r the amplitude is $A = A_0 r^{2\sigma}$ where A_0 is the waist to width relation from the previous section. The following figures present a simulation analysis of an output beam with wavelength $\lambda = 1000\ nm$ from a Herriott cell with a specific set of initial conditions. Figures (C.15-C.18) present the amplitude cross section for wavelength at multiple modes. Figures (C.7-C.10 (left)) present fits of $A = ar^b$ for different modes. Description of the fitted equation are presented on the fits and a summery of the fit parameters a and b are presented on figure C.10. A linear fit of parameter b with respect to the Herriott cell modes support the connection in equation 2.5.

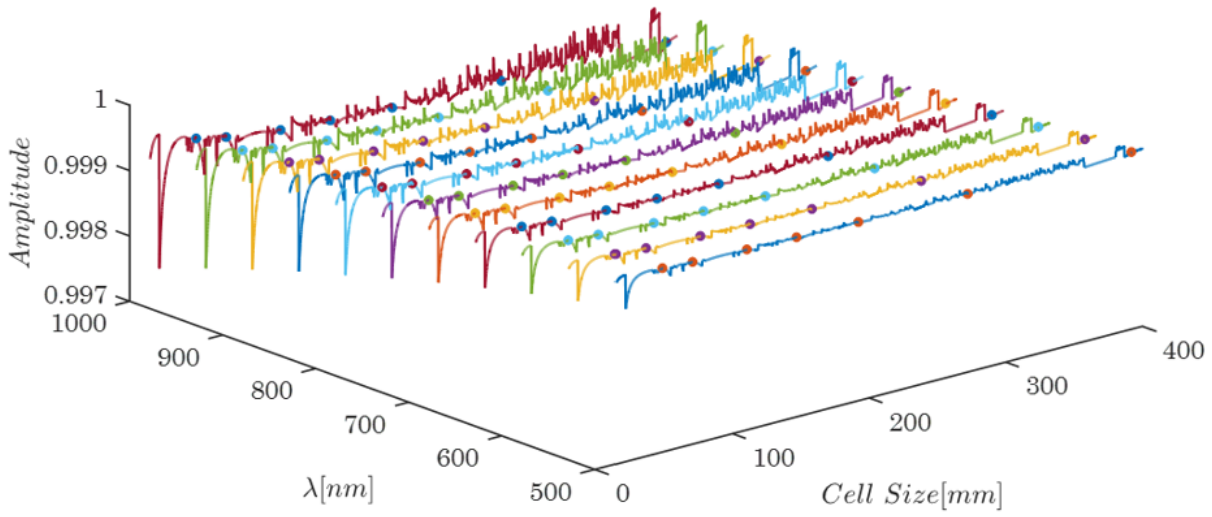

FIGURE C.1: Amplitude of a Herriott cell output beam with respect to the Herriott cell size for Gaussian beams of different wavelengths. The lines represent all possible outputs for a specific set of initial conditions and the dots represent outputs that comply to a specific alignment condition.

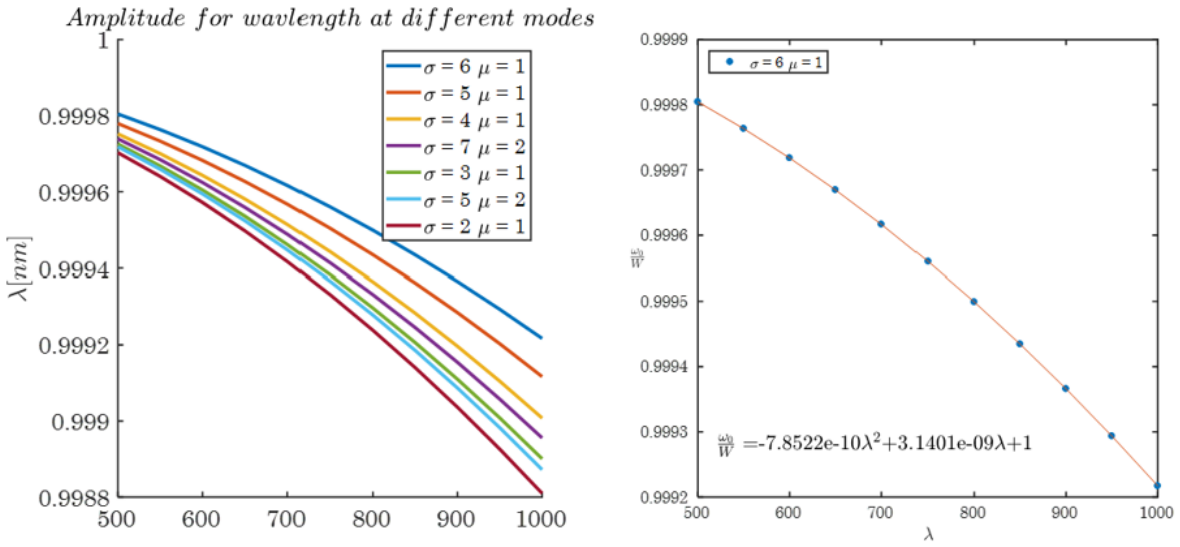

FIGURE C.2

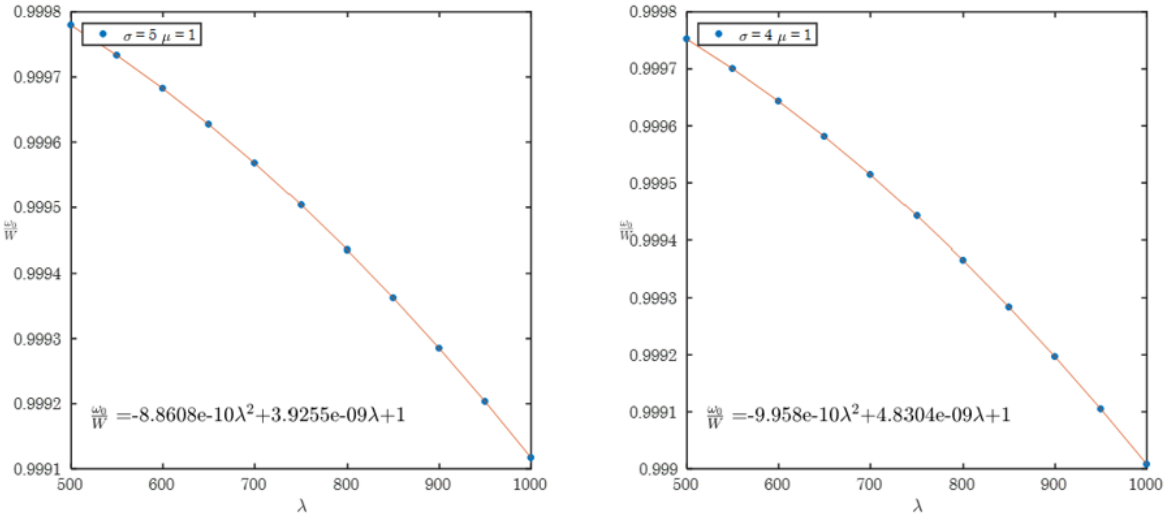

FIGURE C.3

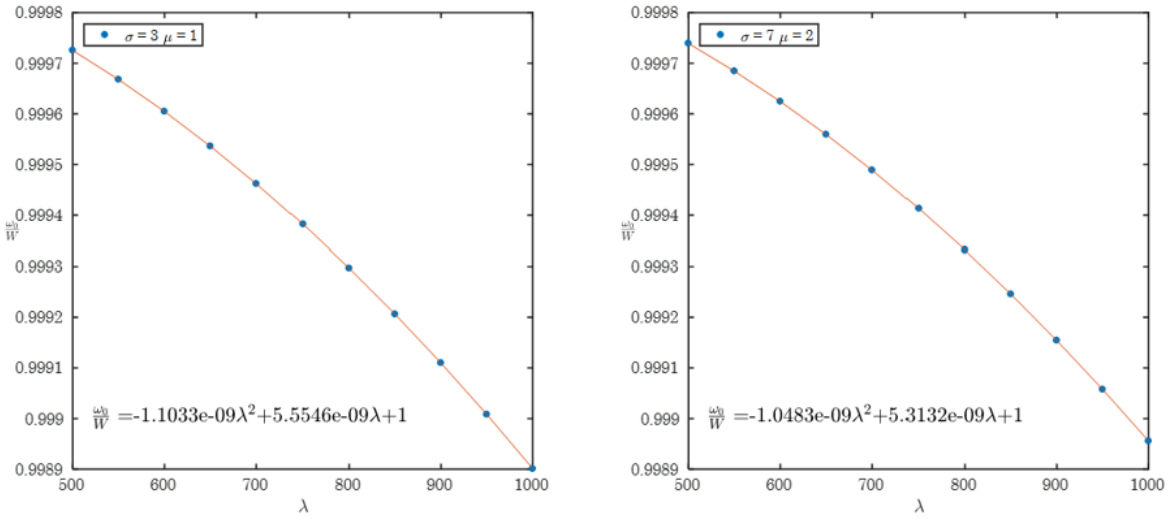

FIGURE C.4

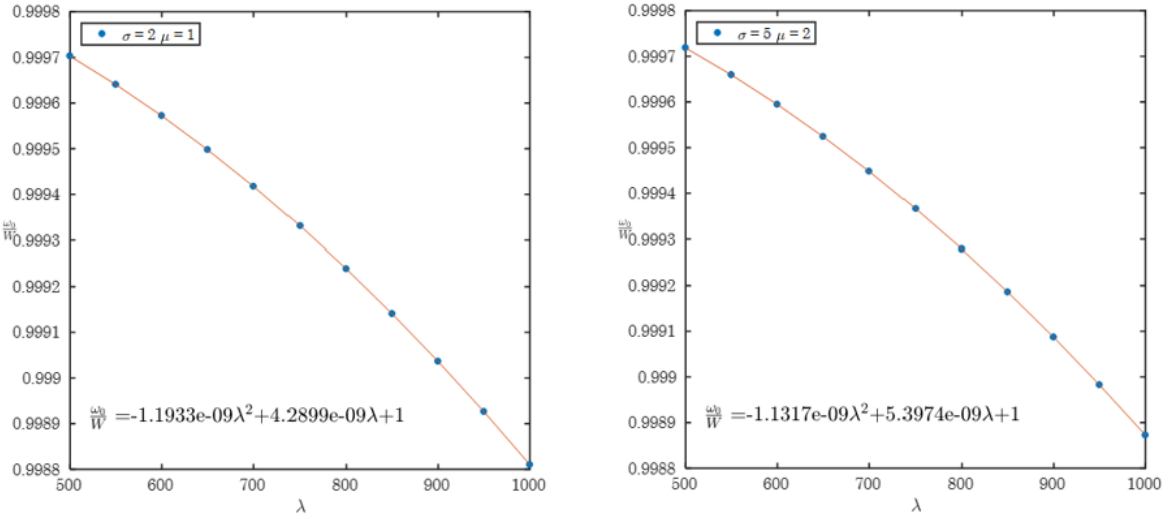

FIGURE C.5

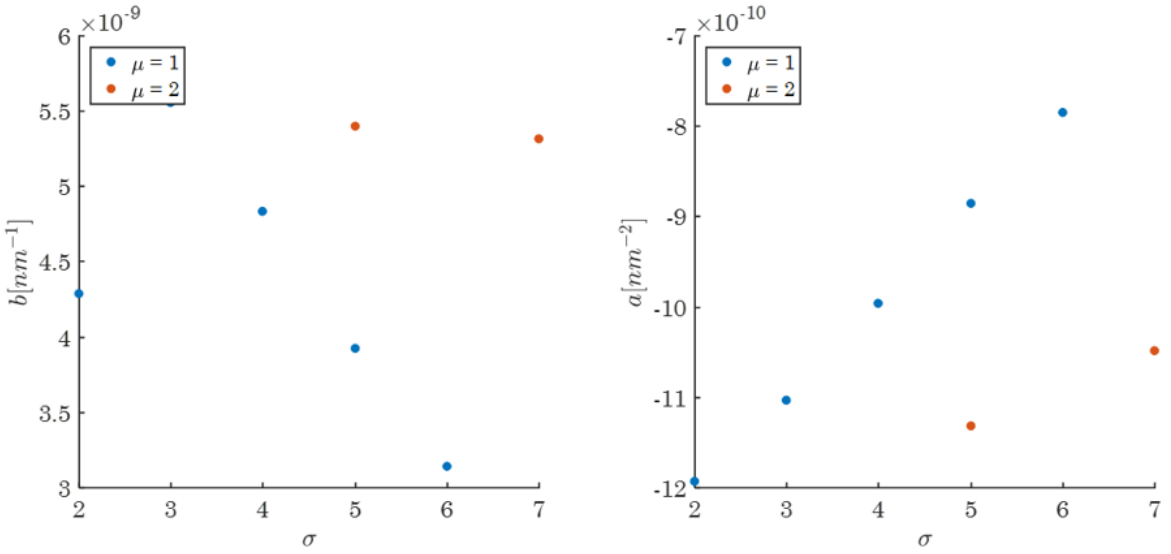

FIGURE C.6

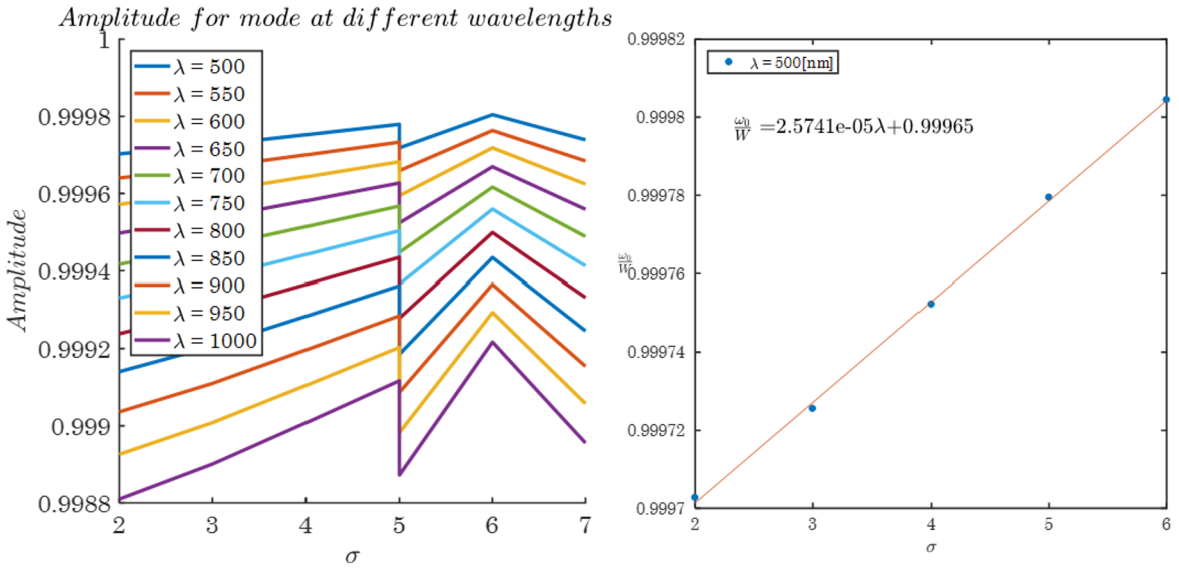

FIGURE C.7

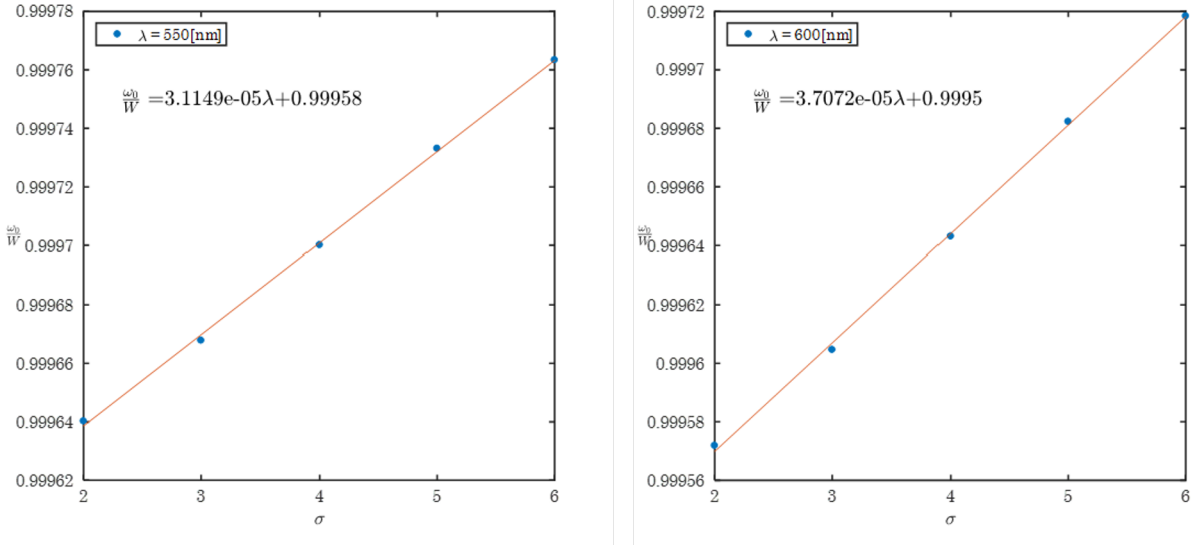

FIGURE C.8

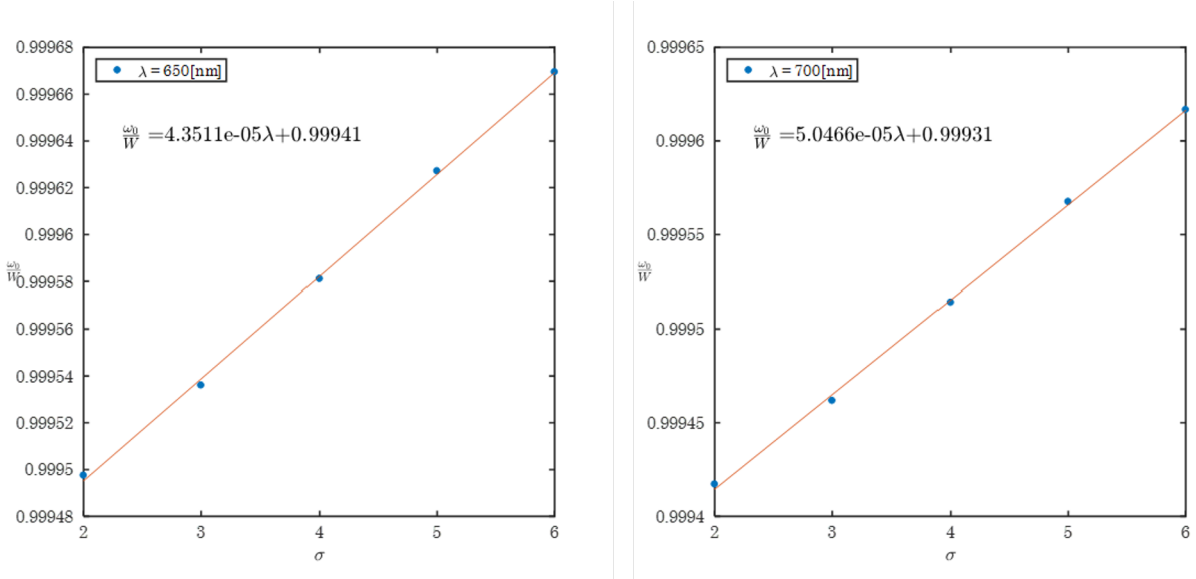

FIGURE C.9

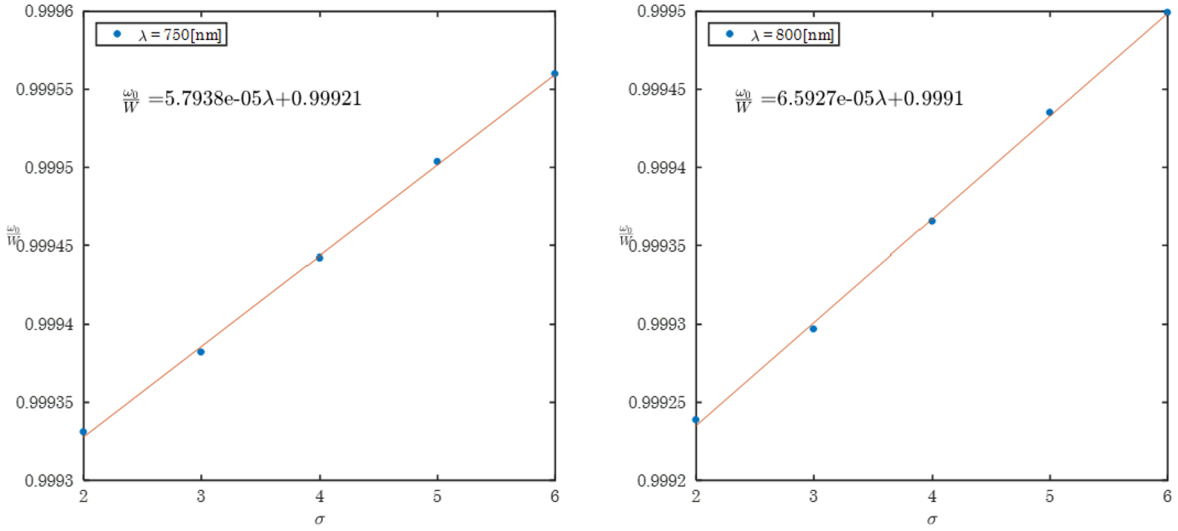

FIGURE C.10

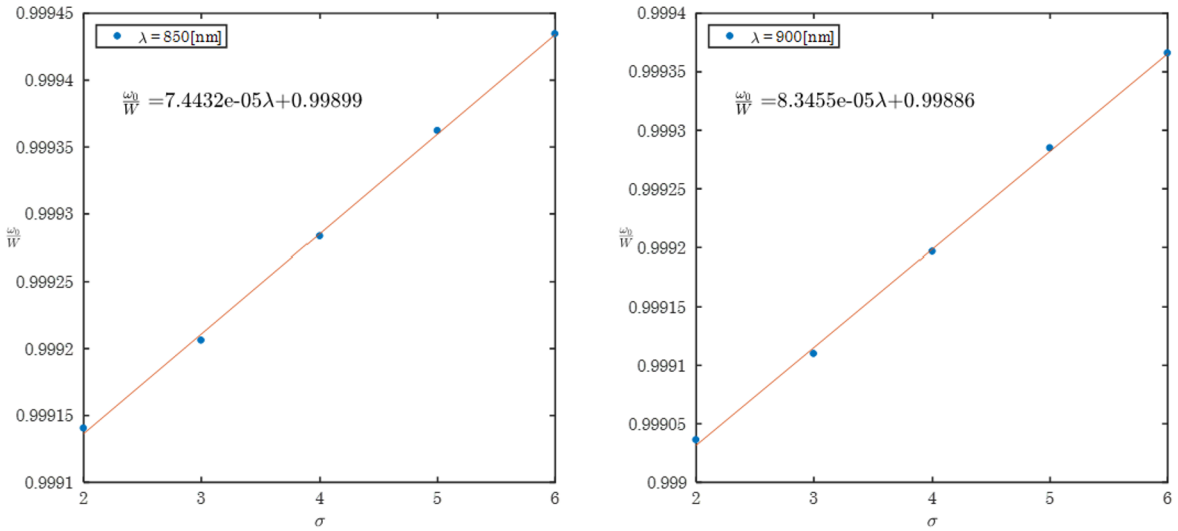

FIGURE C.11

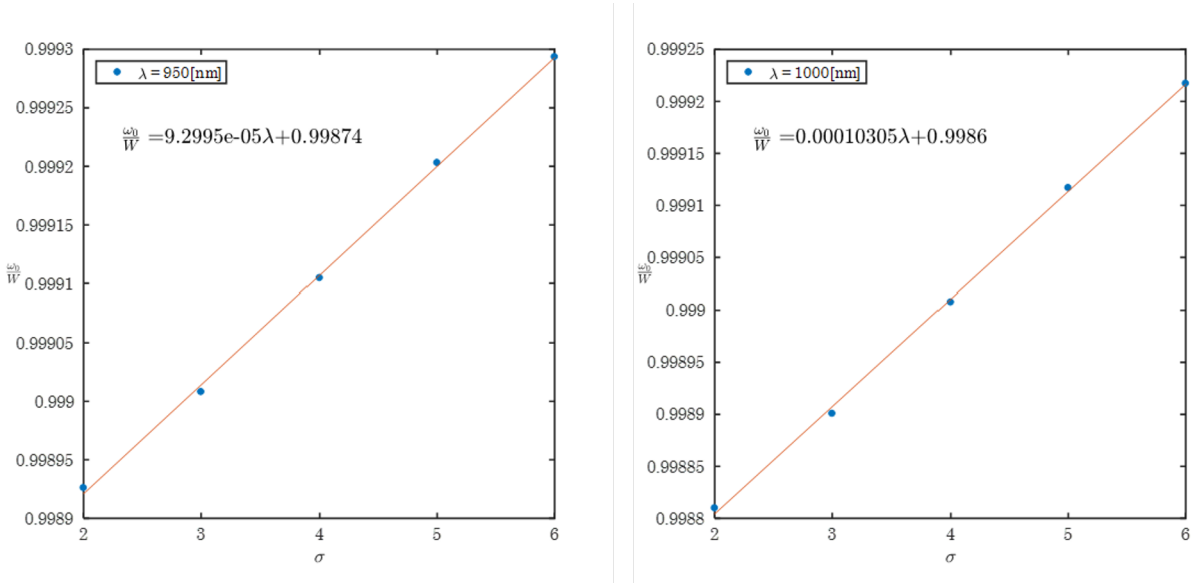

FIGURE C.12

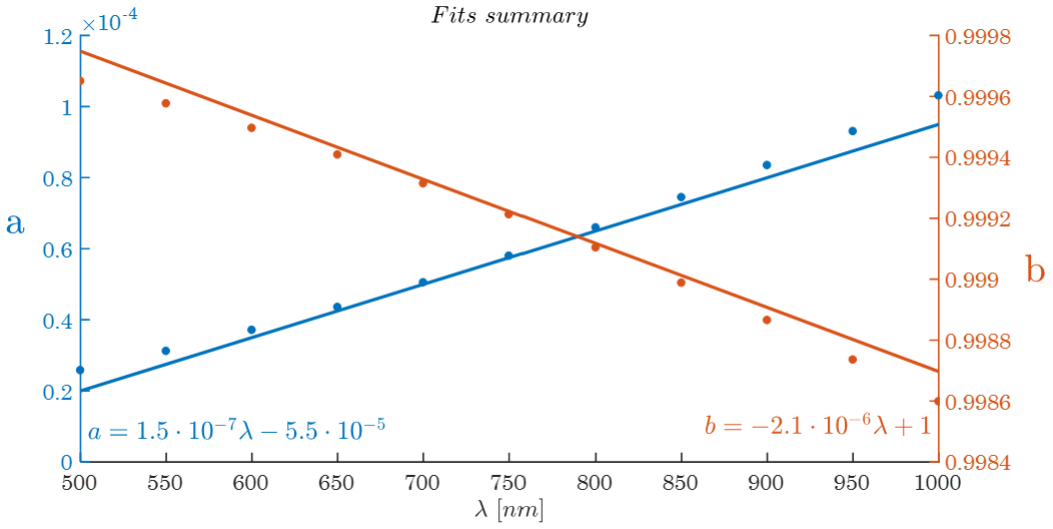

FIGURE C.13

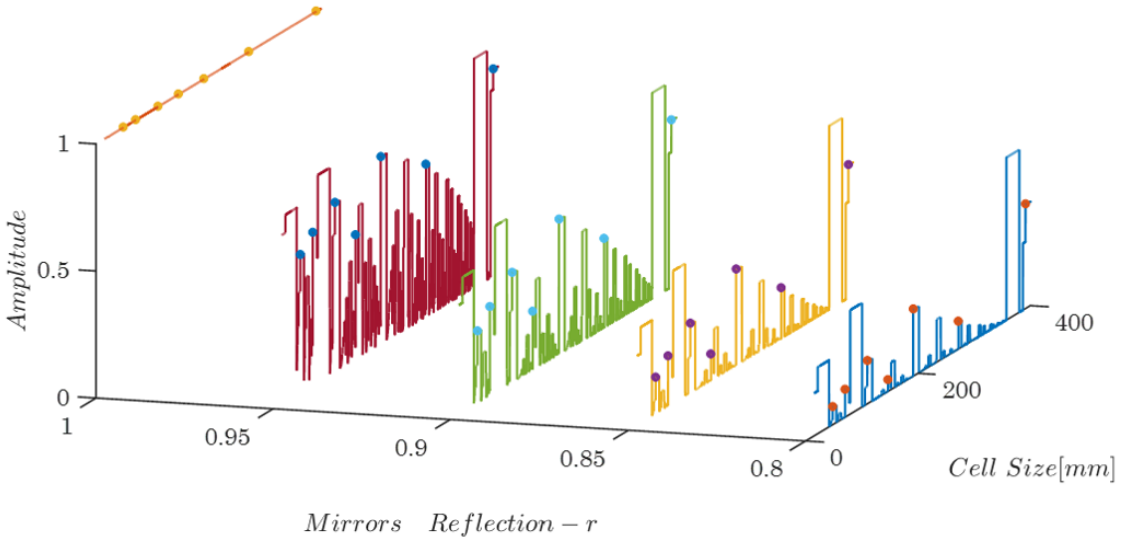

FIGURE C.14: Amplitude of a Herriott cell output beam with respect to the Herriott cell size for Gaussian beam of wavelength $\lambda = 1000\ nm$ for different mirror reflection. The lines represent all possible outputs for a specific set of initial conditions and the dots represent outputs that comply to a specific alignment condition.

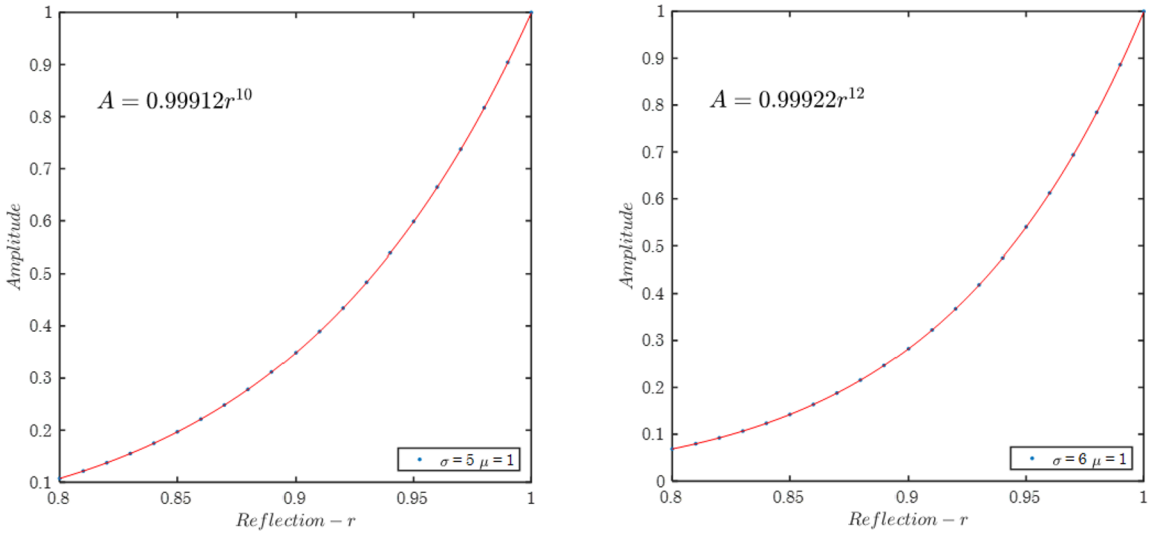

FIGURE C.15

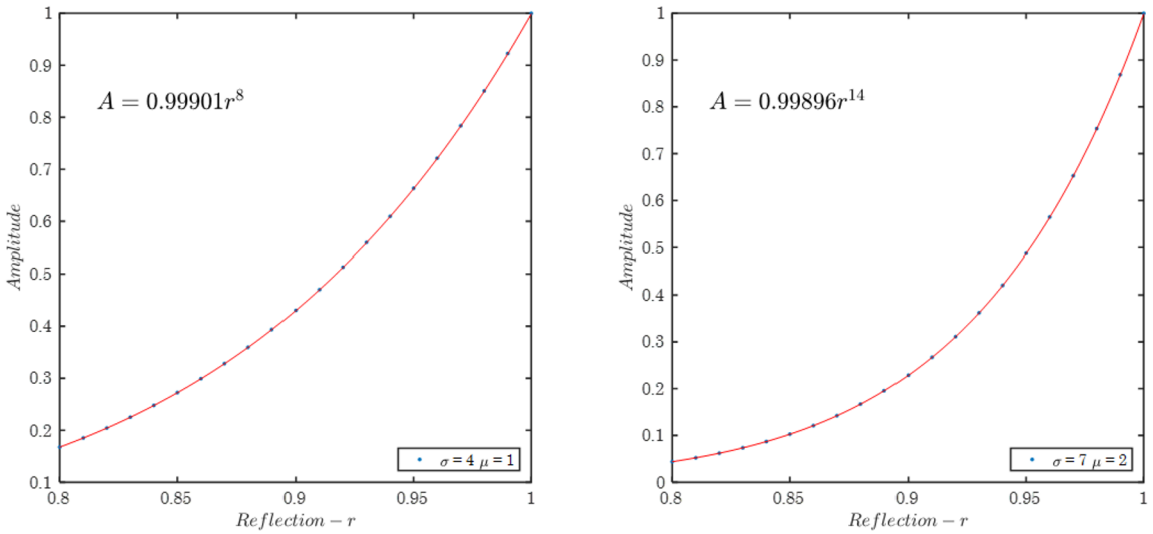

FIGURE C.16

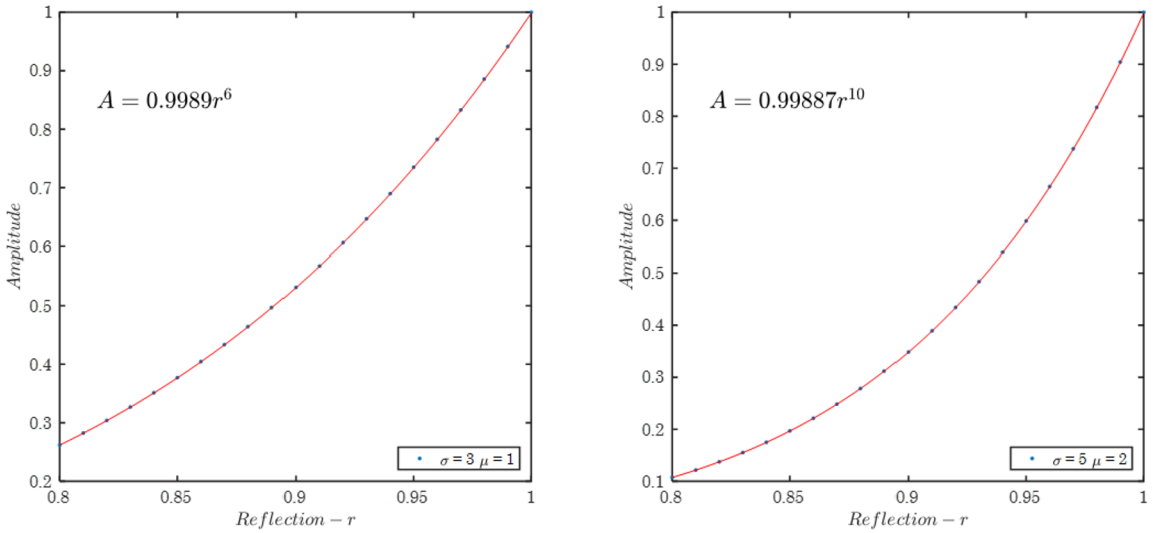

FIGURE C.17

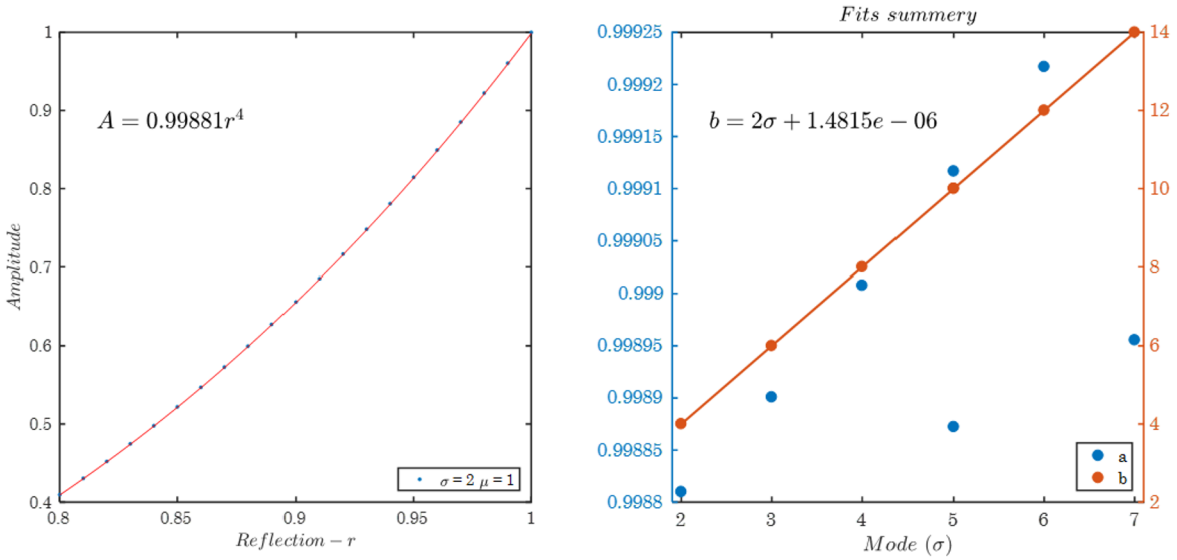
$A = 0.99881r^4$
Amplitude
Reflection − r
σ = 2 μ = 1
Fits summery
$b = 2\sigma + 1.4815e - 06$
Mode (σ)
a
b

FIGURE C.18

Herriott Cell Mirror Generated Phase

In this appendix we present a comparison of the different phases generated by the Herriott cell for different mode numbers at different input wavelengths. We have studied the phases generated by the mirror's complex reflection -χ, the optical path in the Herriott cell $\frac{2*\pi L(\sigma,d)}{\lambda}$ and the total phase of the output EM field $E = E_0 e^{-i\phi}$, ϕ. All phases are in units of π and the optical path phase is calculated only as the reminder of the fraction $\frac{2*\pi L(\sigma,d)}{\lambda}$.

figure C.19 present an example for the optical path phase generated for all input wavelengths at mode number $\sigma = 7$. Due to it's significantly smaller scale then the other phases, the optical path phase appears to be a flat line. This figure demonstrate that it is not so. figures C.20-C.22, present the comparison of all the phases mentioned above, the optical path phase is in blue, the mirror's reflection phase is in red and the total phase is in black.

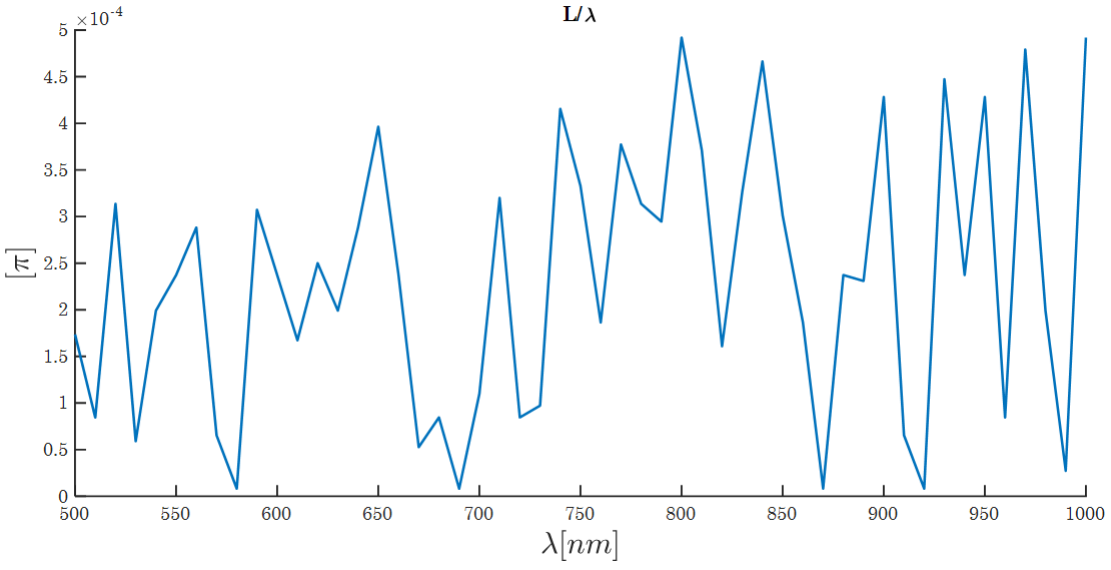

FIGURE C.19

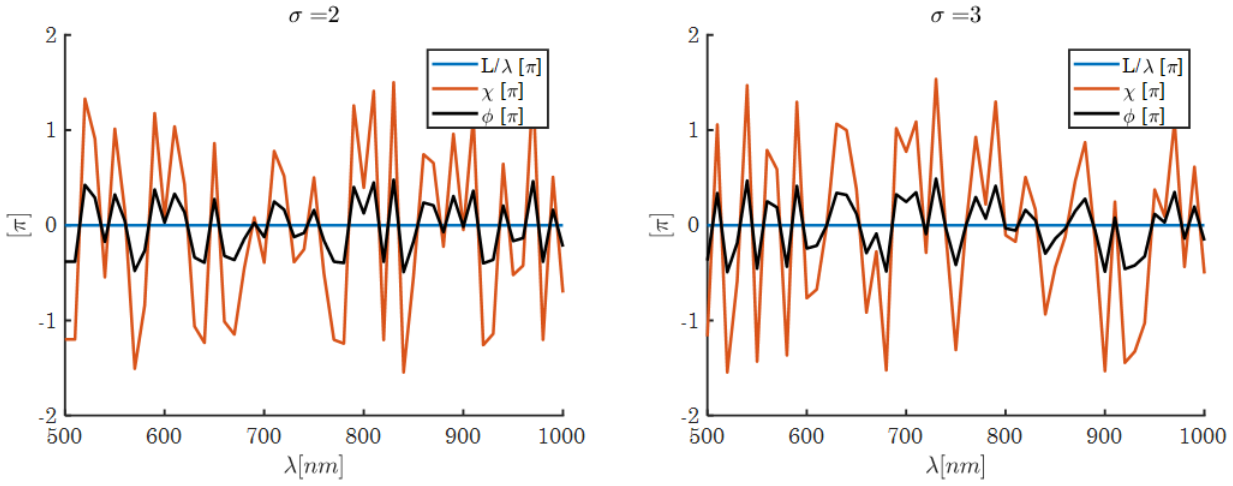

FIGURE C.20

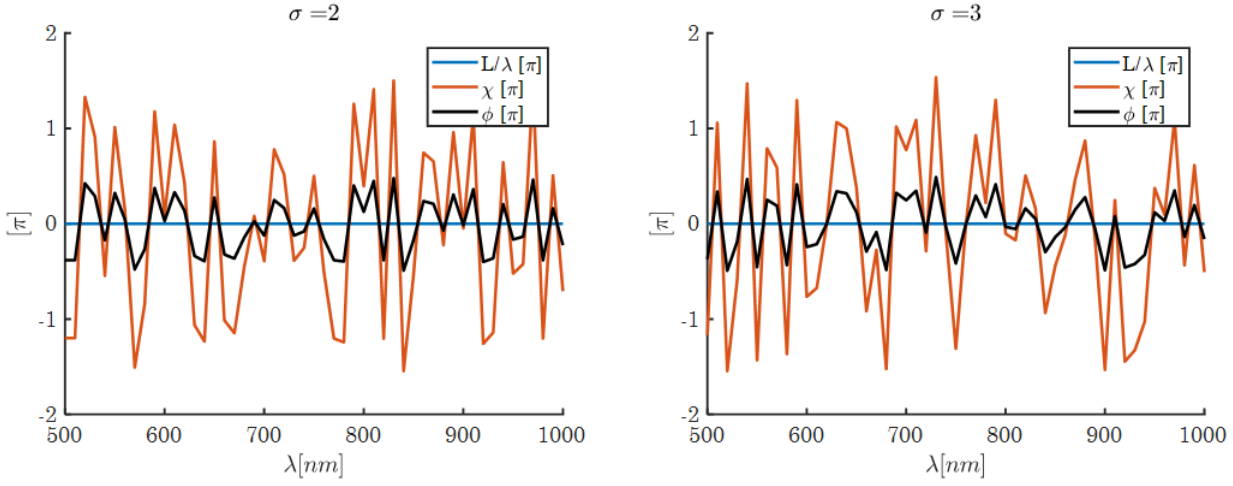

FIGURE C.21

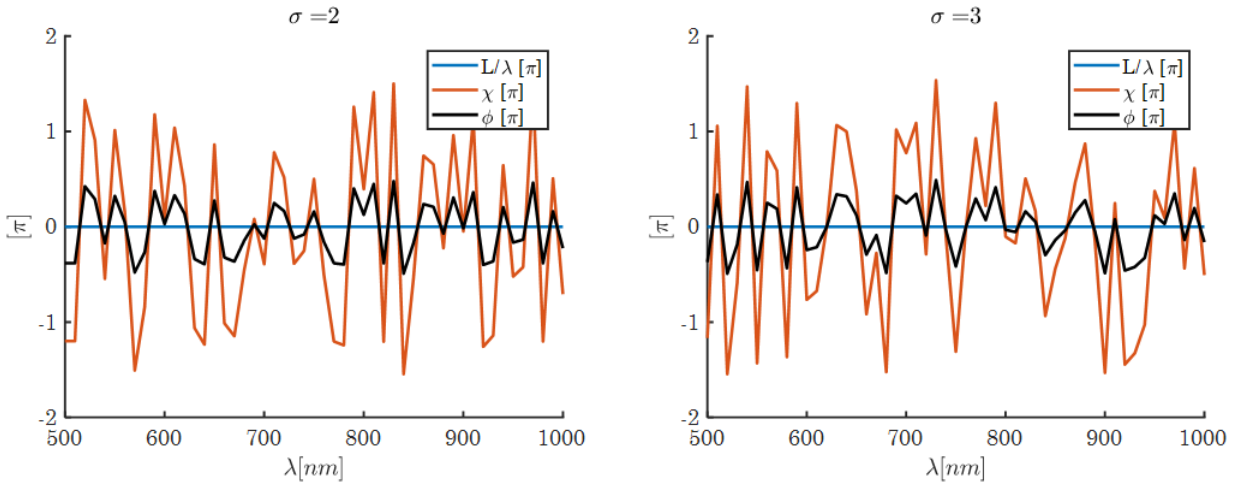

FIGURE C.22

Appendix D. *Supplementary Material for the Herriott FT-IR Simulation*

In this appendix we present the supplementary material for the Herriott FT-IR simulation results. The results presented are for a Herriott FT-IR simulation of a polychromatic light composed of three spectral lines : $\lambda = 800, 900, 1000nm$ sampled with a $180mm$ delay line at three Herriott cell modes. Figures D.1-D.3 present the interferograms taken at each step. The overlapping interferograms, cross correlation signal and corrected interferograms between steps one-two and two-three are showen in figures D.4,D.4. The combined interferogram of the steps and the corrosponding references step are presented in figures D.6 and D.7.

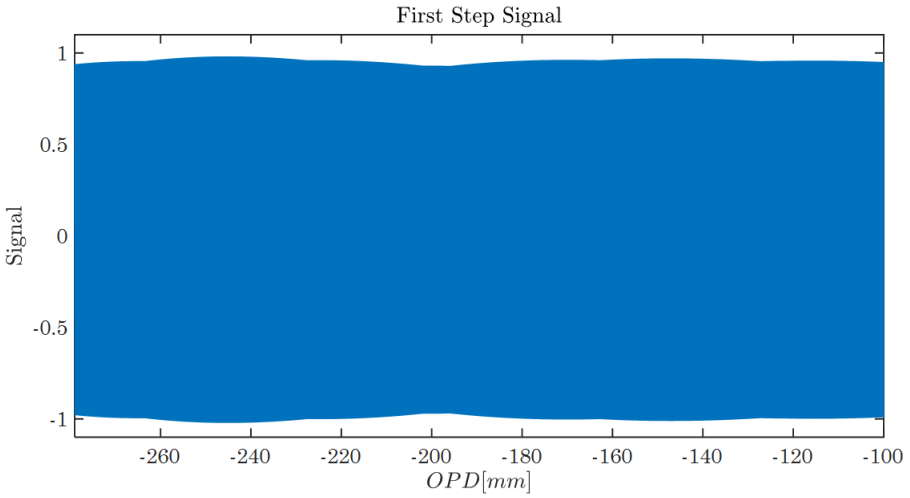

FIGURE D.1

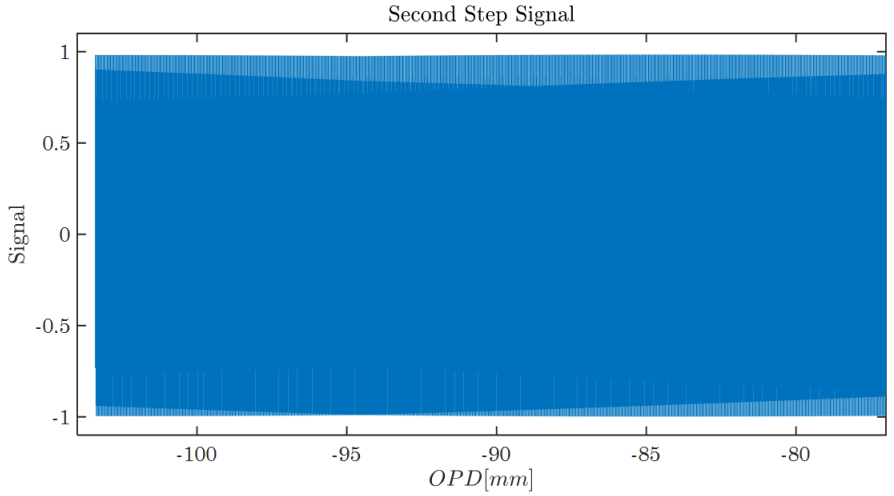

FIGURE D.2

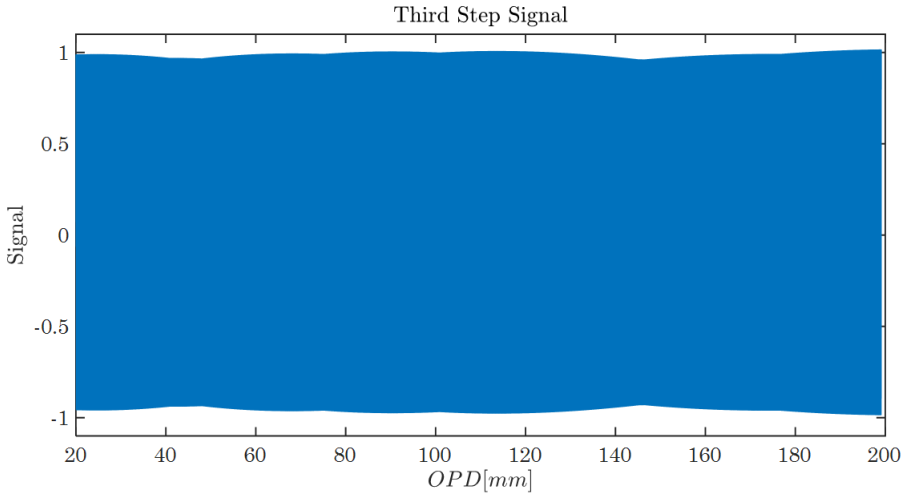

FIGURE D.3

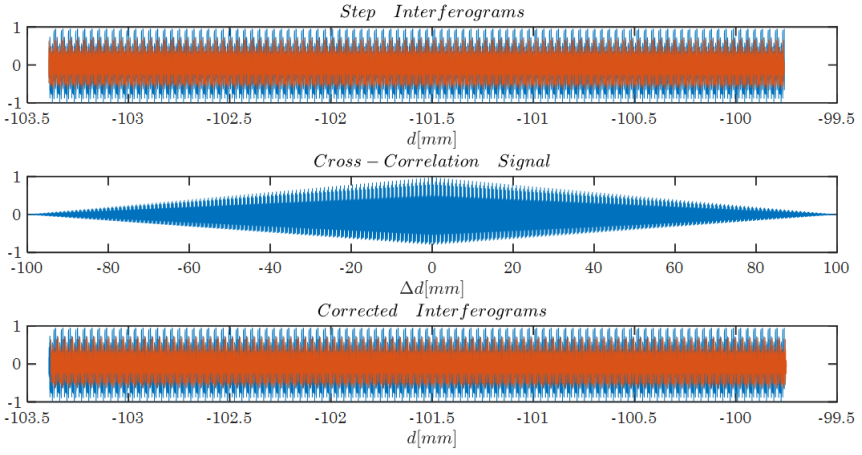

FIGURE D.4

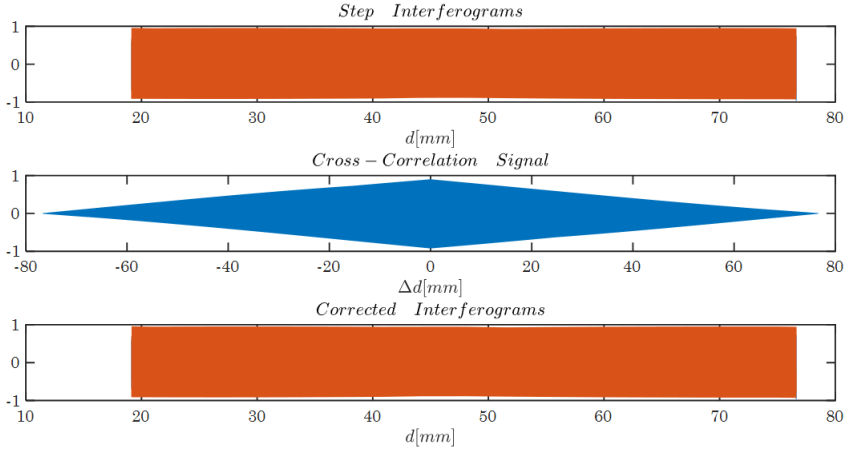

FIGURE D.5

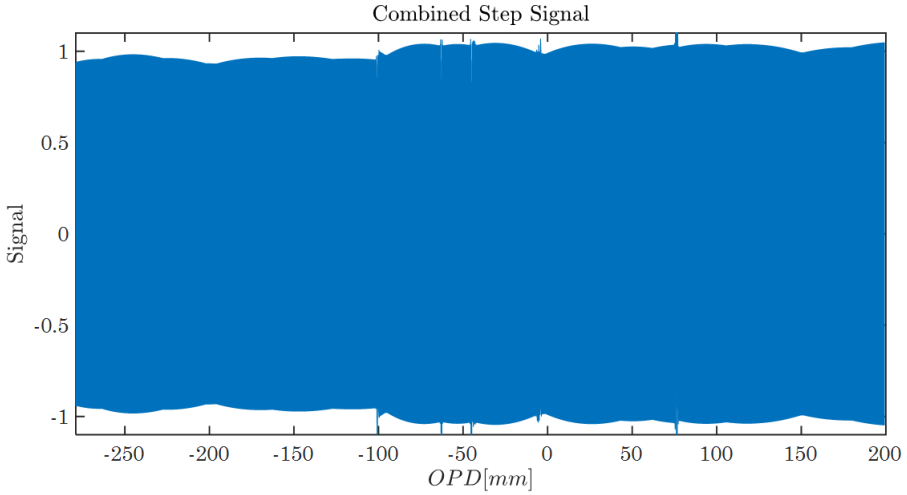

FIGURE D.6

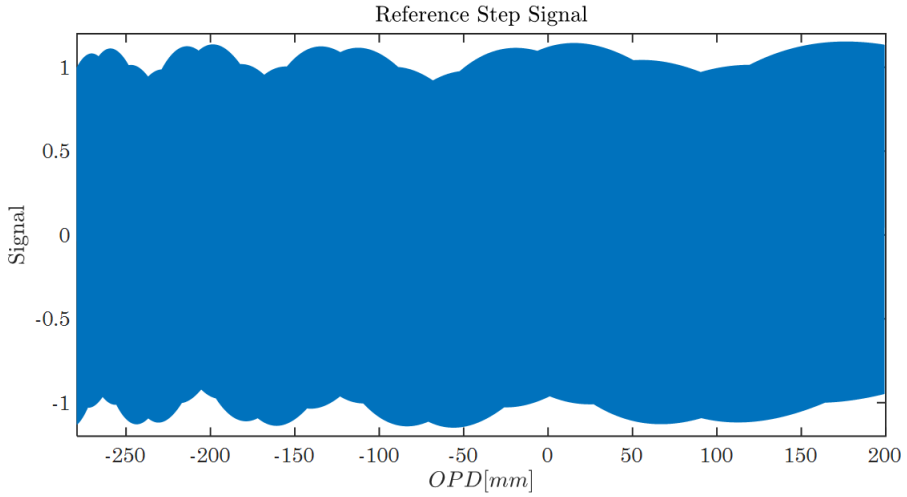

FIGURE D.7

Appendix E. *Supplementary Material for Herriott cell calibration*

In this appendix we present the supplementary material for the for the Herriott cell OPD calibration. The following figures show the calibration process for the mode set in section 3.2. The calibration was made with a short pulse of about $100fs$ temporal width around $780nm$ wavelength and the arm were spectrally separated with $13nm$. The filters separating the arms spectrally were a long-pass above $785nm$ for the delay arm and a short-pass below $775nm$ for the Herriott arm.

Figures E.1- E.3 show the fundamental and SFG signals for OPD at mode numbers $\sigma = 5, 6, 7$. The fundamental spectrum in the figures is shown as two spectral lines with constant amplitude for all OPS's around $\lambda = 780nm$. The nolinear responses are shown as two low spectral lines with constant amplitude for all OPS's around $\lambda = 390nm$ for the SHG and a high spectral pick around a specific OPD for the SFG. The SFG spectral line has a significant width on the spectral axis and the temporal (OPD) axis. Therefore there is a need to fit the fundamental spectrum with respect to the spectral axis in order to find the exact wavelength for the SFG. The Gaussian fits for the fundamental spectrum are presanted at figures E.4-E.6:

$$\begin{cases} S_{Delay}(\lambda) = a_D e^{-\left(\frac{\lambda-\mu_D}{c_D}\right)^2} \\ S_{Herriott}(\lambda) = a_H e^{-\left(\frac{\lambda-\mu_H}{c_H}\right)^2} \end{cases} \tag{E.1}$$

The red trend line mark the Gaussian fit for the delay arm fundamental spectrum and the green trend line is for the Herriott arm. A second spectral line around $767nm$ is noticeable, but it does not support phase matching conditions for the SFG. Therefore it is not part of the calibration. Finally, the spectral intensity of the SFG is fitted for a Gaussian with respect to the OPD:

$$I_{SFG}(OPD) = ae^{-\left(\frac{OPD-\mu}{c}\right)^2} \tag{E.2}$$

The wavelength for the OPD is chosen according to

$$\lambda_{SFG} = \frac{\mu_D + \mu_H}{4} \tag{E.3}$$

The SFG fits are presented in figures E.7-E.9.

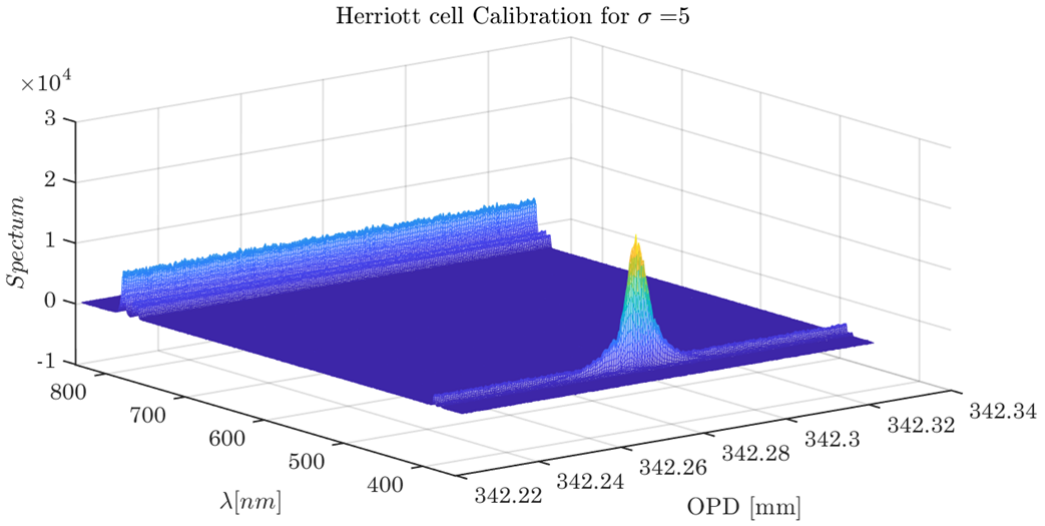

FIGURE E.1

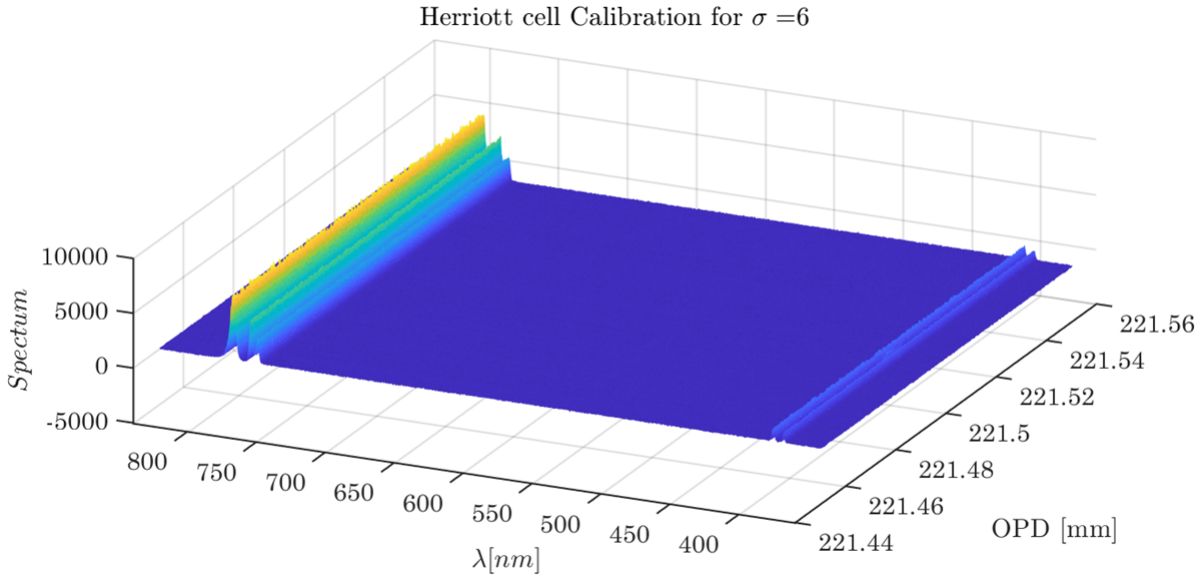

FIGURE E.2

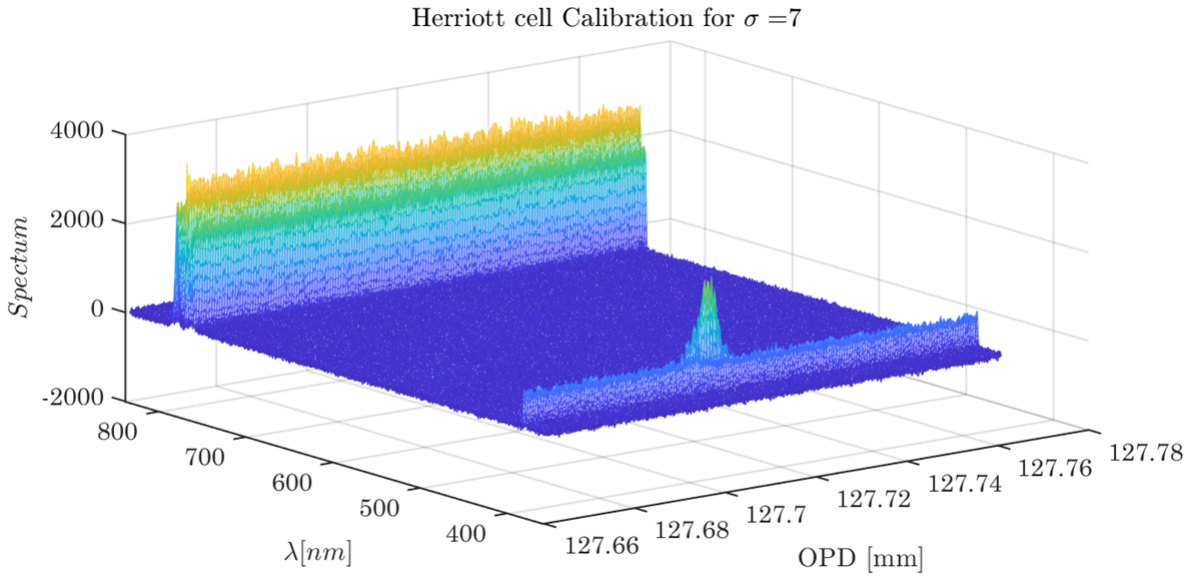

FIGURE E.3

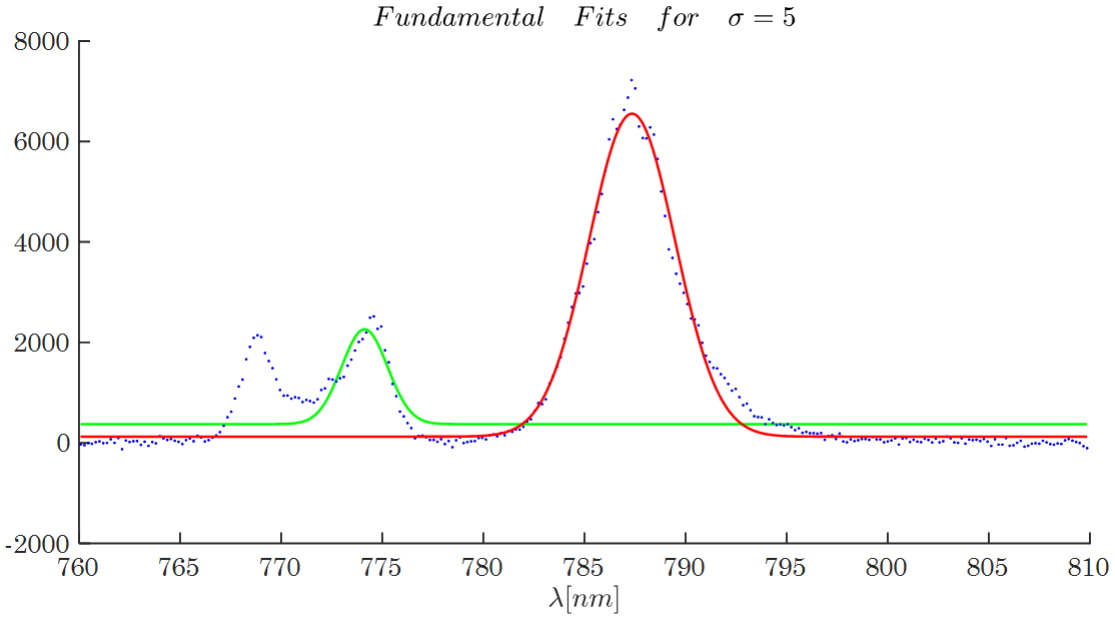

FIGURE E.4

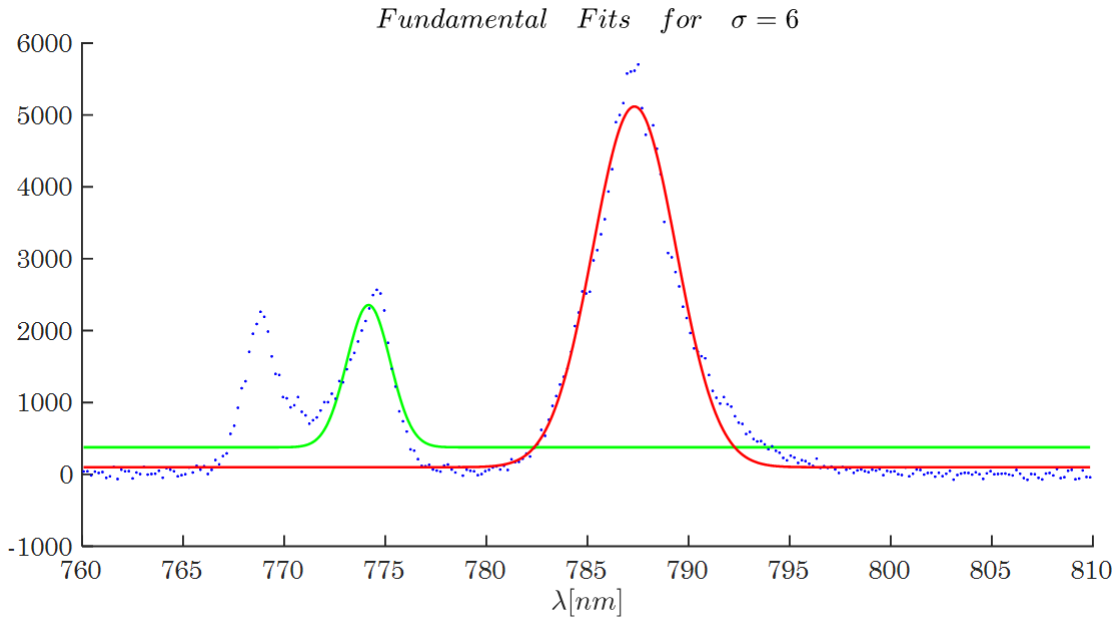

FIGURE E.5

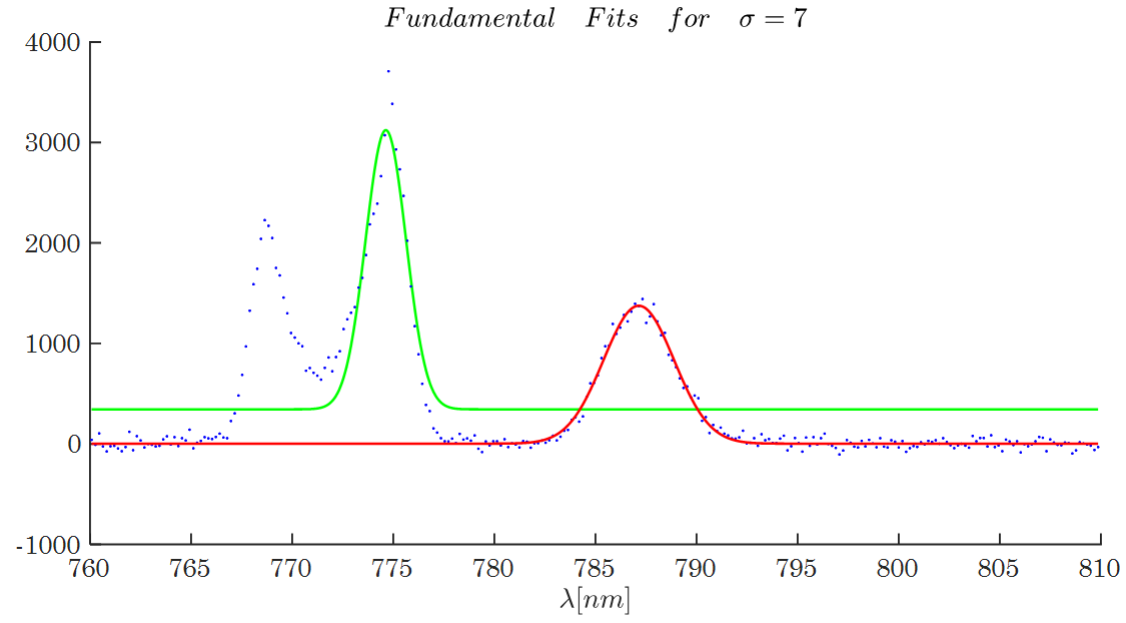

FIGURE E.6

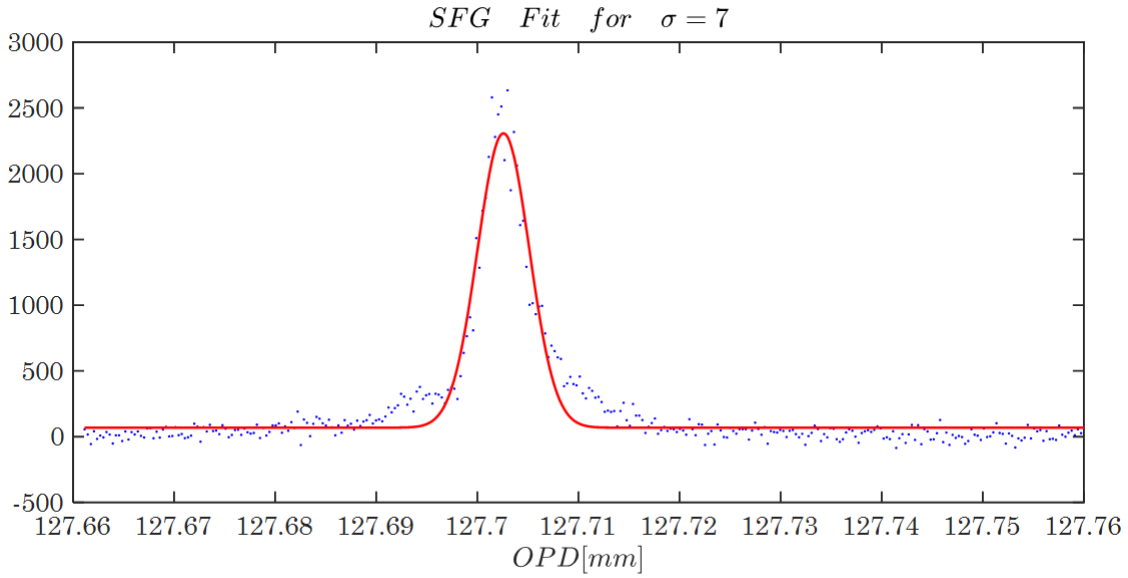

FIGURE E.7

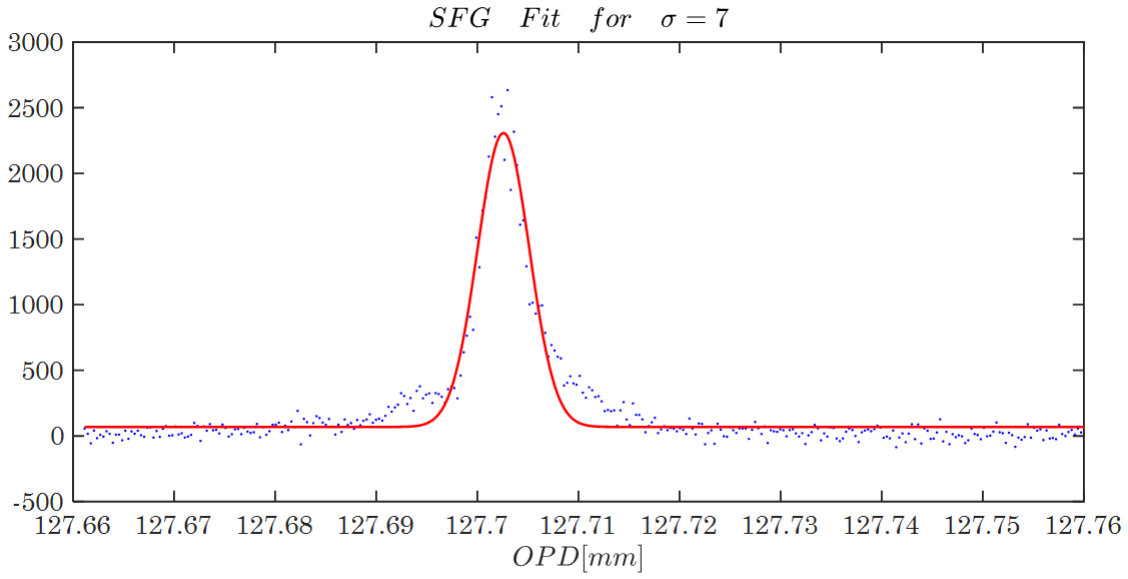

FIGURE E.8

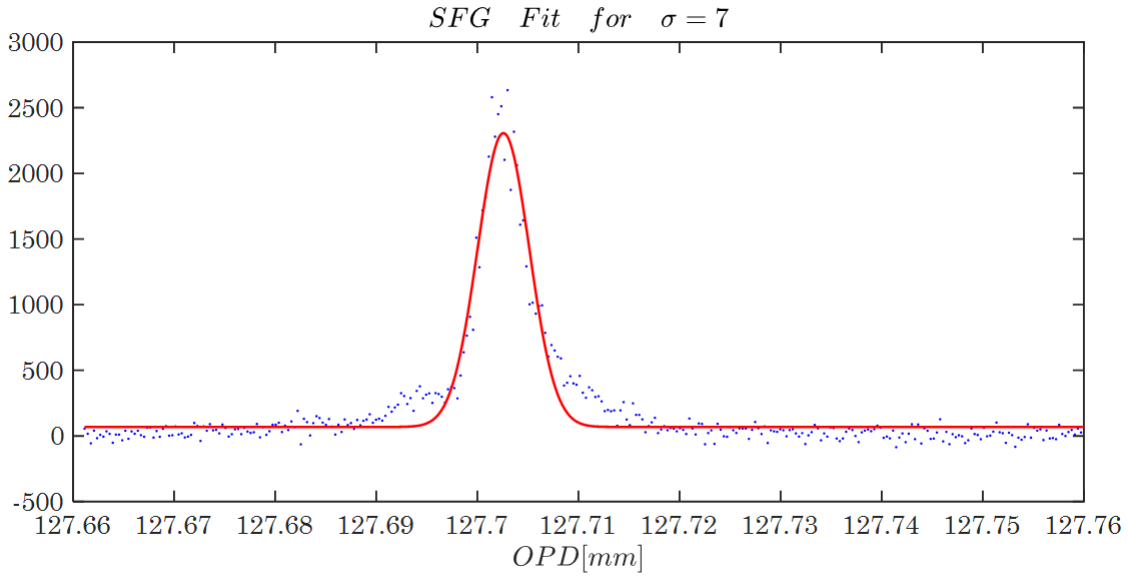
SFG Fit for σ = 7
3000
2500
2000
1500
1000
500
0
-500
127.66
127.67
127.68
127.69
127.7
127.71
127.72
127.73
127.74
127.75
127.76
OPD[mm]

FIGURE E.9

Appendix F. *HeNe Experiment Supplementary Material*

In this appendix we present the supplementary material for the Herriott FT-IR proof-of-concept experiment with a HeNe laser. Figure F.1 present the interference pattern of the Herriott FT-IR, taken from a camera,positioned after the second beam splitter (see figure 3.1). Figures F.2-F.4 present the interferograms taken at each step. The overlapping interferograms, cross correlation signal and corrected interferograms between steps one-two and two-three are showen in figures F.5,F.5. The combined interferogram of the steps and the corrosponding references step are presented in figures F.7 and F.8. The Fourier transforms of the steps combinations and reference are shown with Gaussian fits for their envelops in figures F.9 - one step and two step combination, and F.10 - three steps combination and reference.

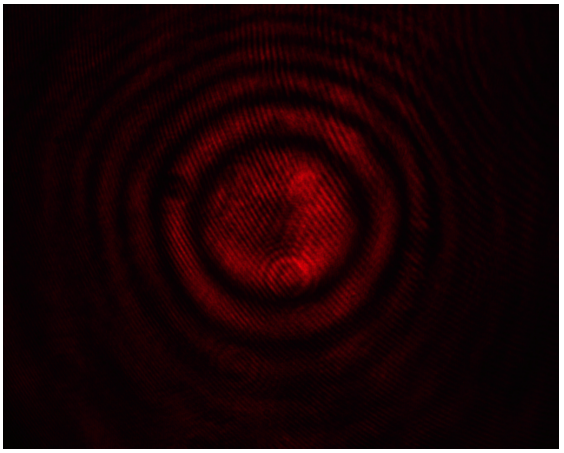

FIGURE F.1

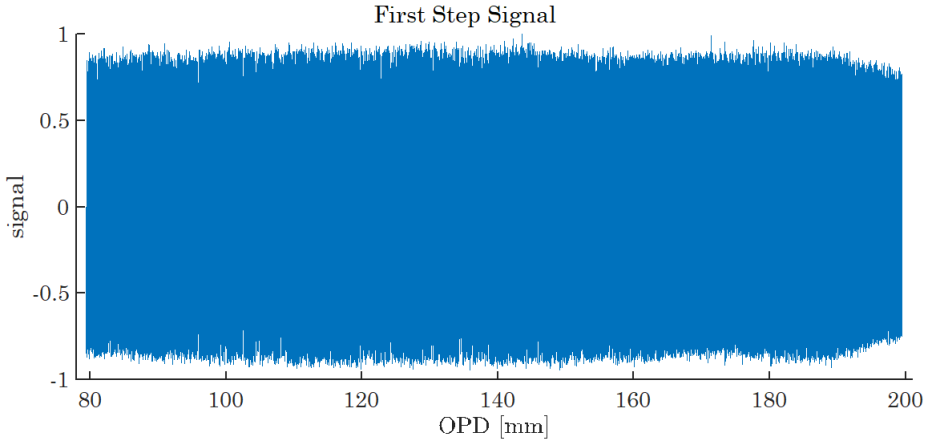

FIGURE F.2

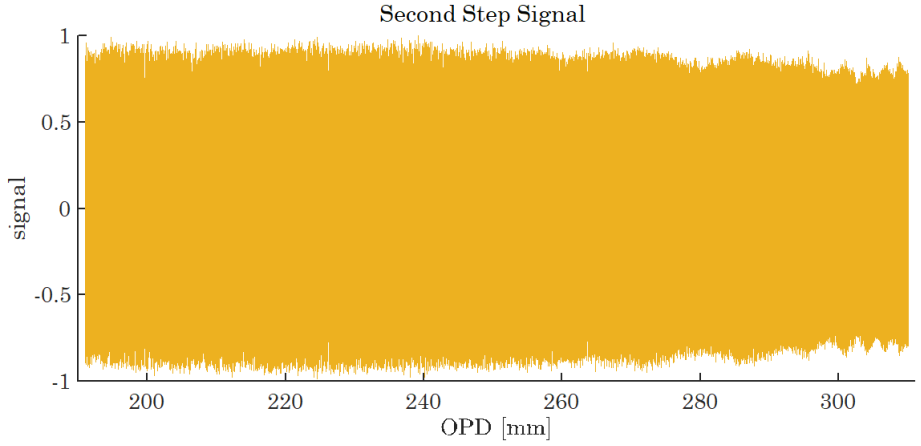

FIGURE F.3

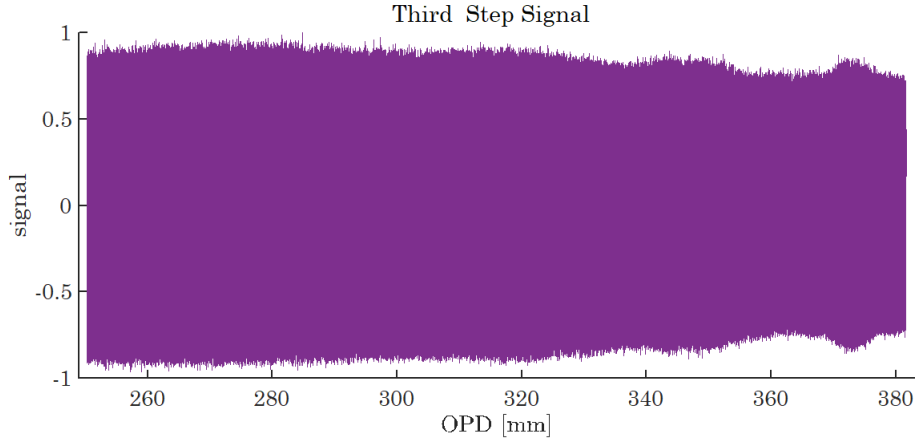

FIGURE F.4

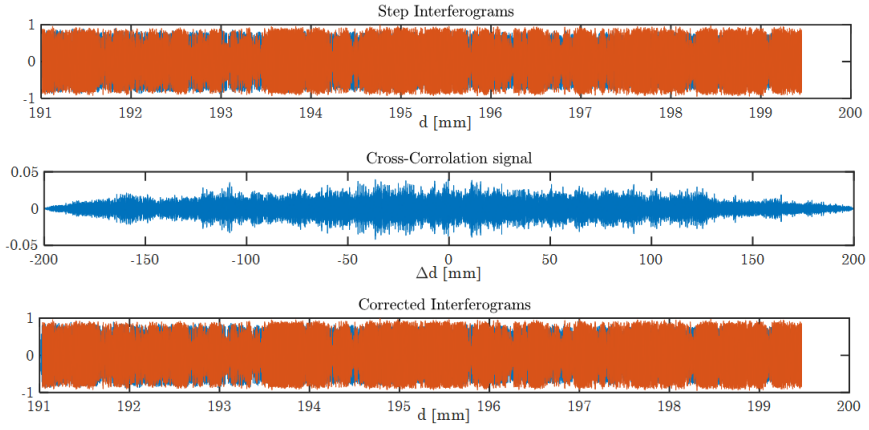

FIGURE F.5

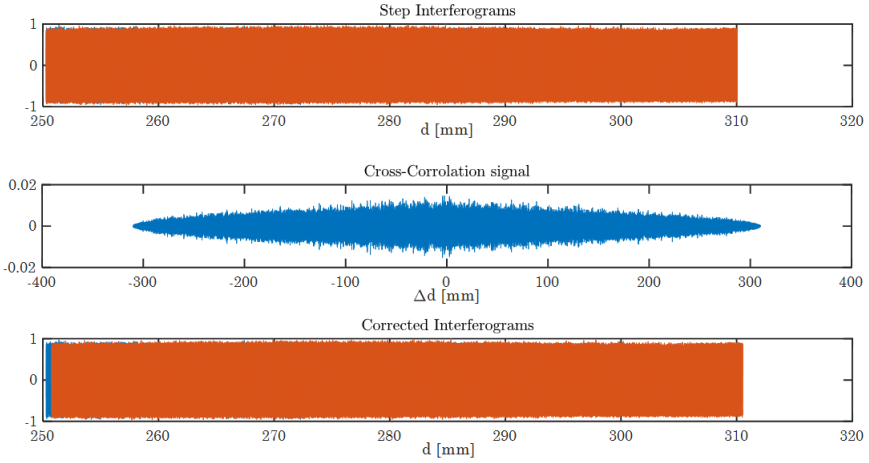

FIGURE F.6

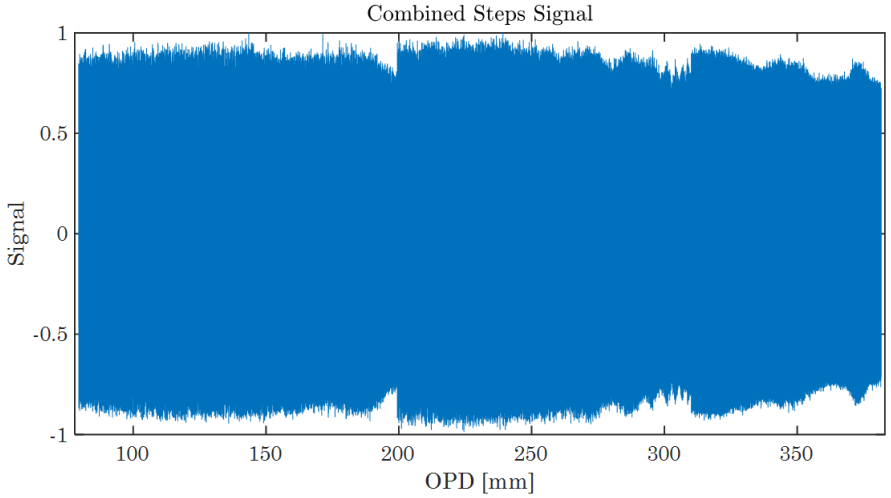

FIGURE F.7

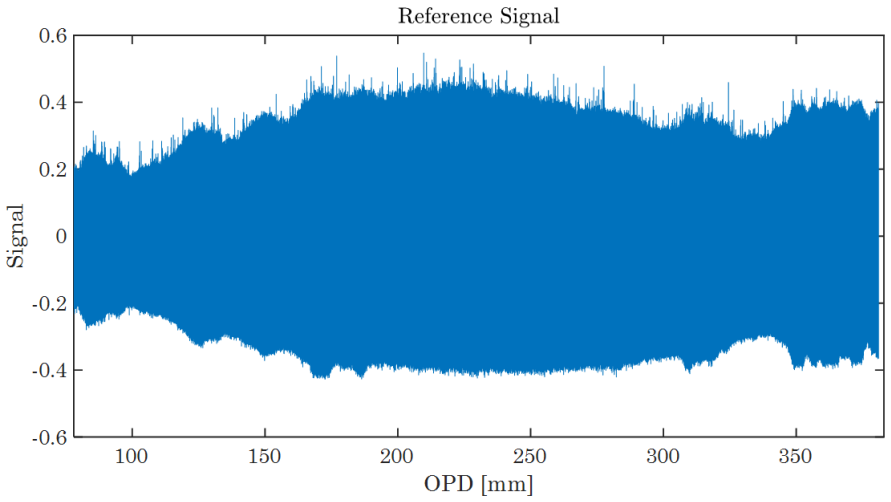

FIGURE F.8

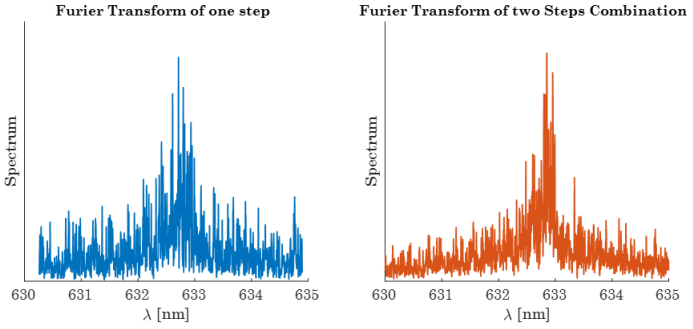

FIGURE F.9

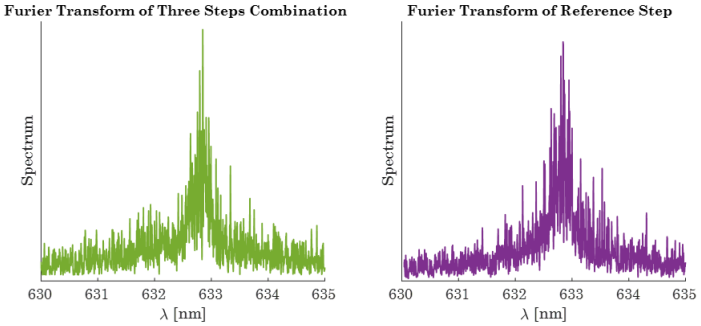

FIGURE F.10

Appendix G. *Experiment Supplementary Material for 780 nm*

In this appendix we present the supplementary material for the Herriott FT-IR proof-of-concept experiment with a 780 nm laser.

Figures G.1-G.3 present the interferograms taken at each step. The overlapping interferograms, cross correlation signal and corrected interferograms between steps one-two and two-three are showen in figures G.4,G.4. The combined interferogram of the steps and the corrosponding references step are presented in figures G.6 and G.7. The Fourier transforms of the steps combinations and reference are shown in figures G.8-G.9.

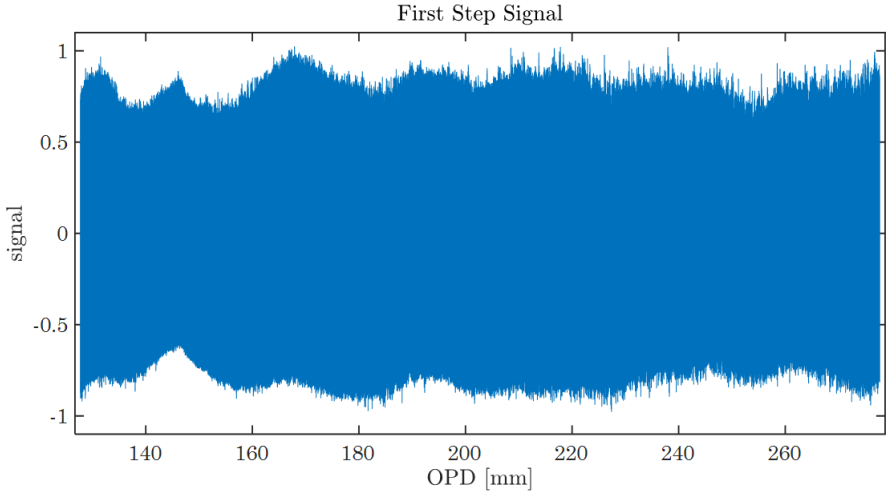

FIGURE G.1

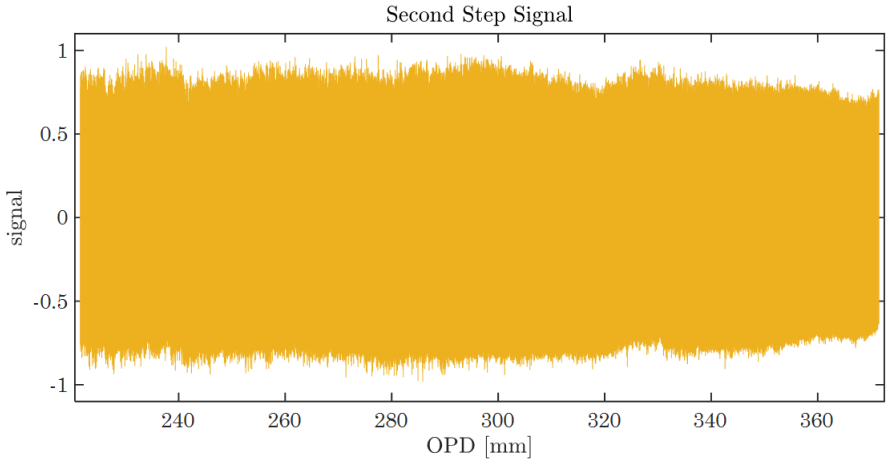

FIGURE G.2

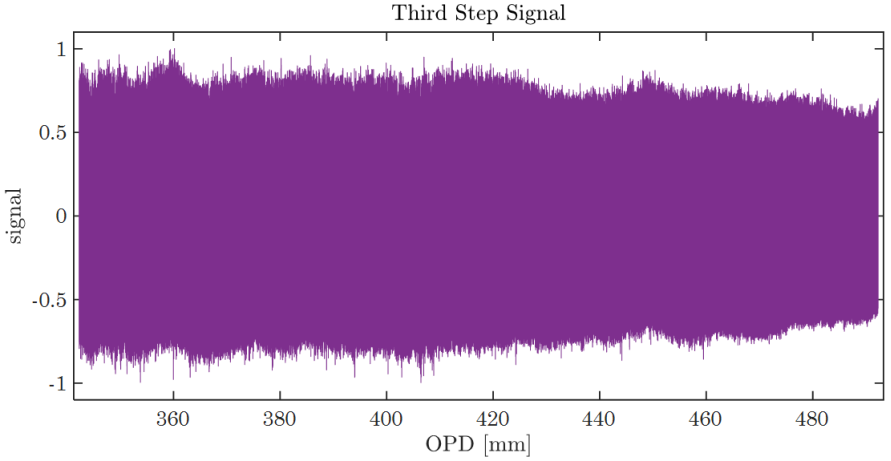

FIGURE G.3

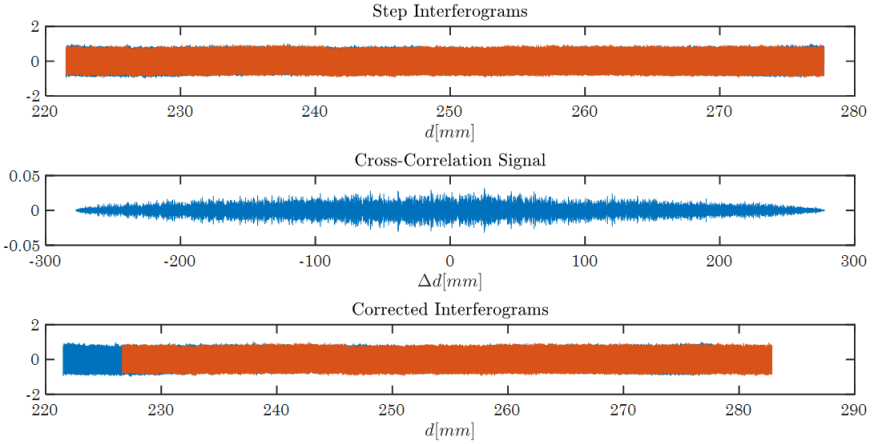

FIGURE G.4

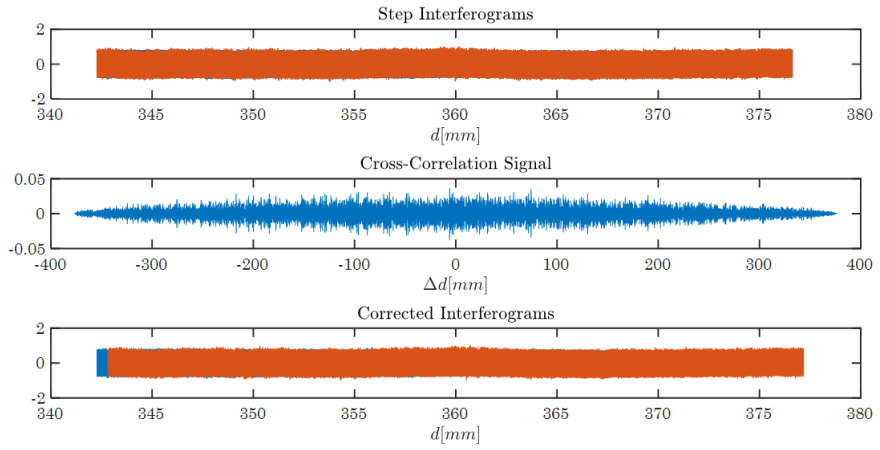

FIGURE G.5

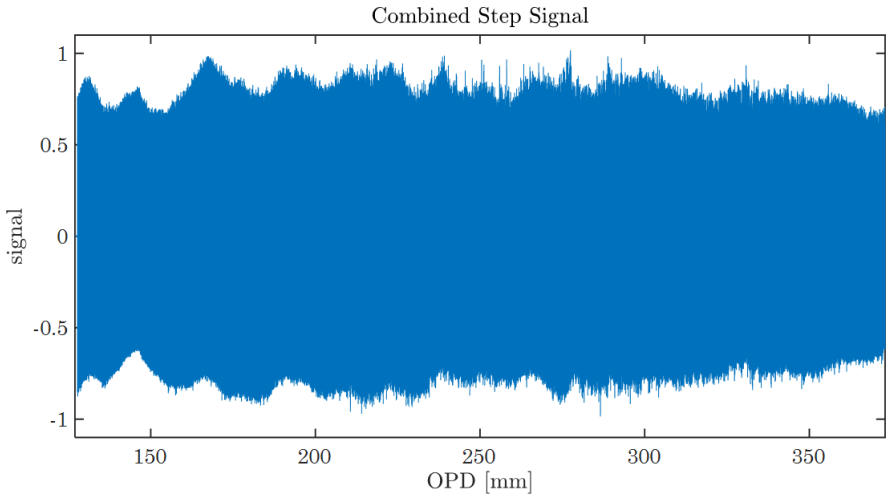

FIGURE G.6

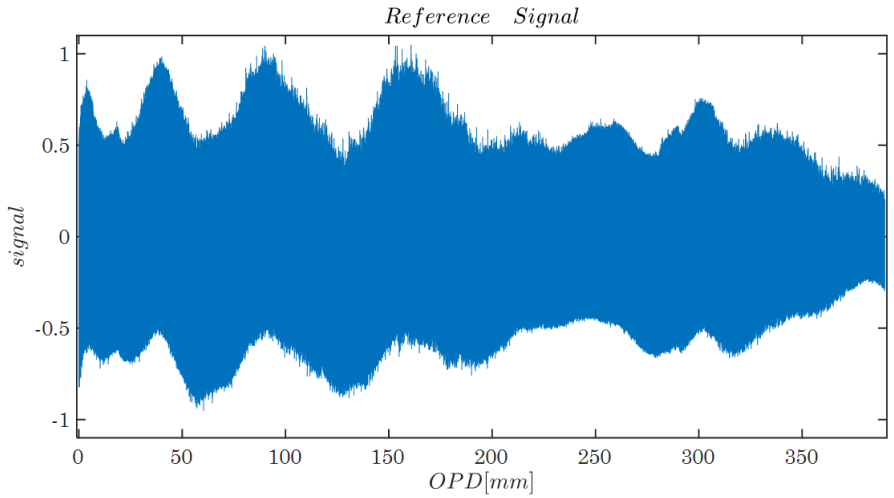

FIGURE G.7

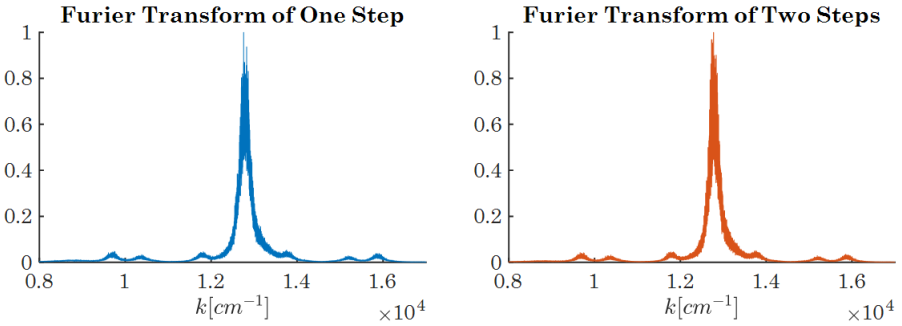

FIGURE G.8

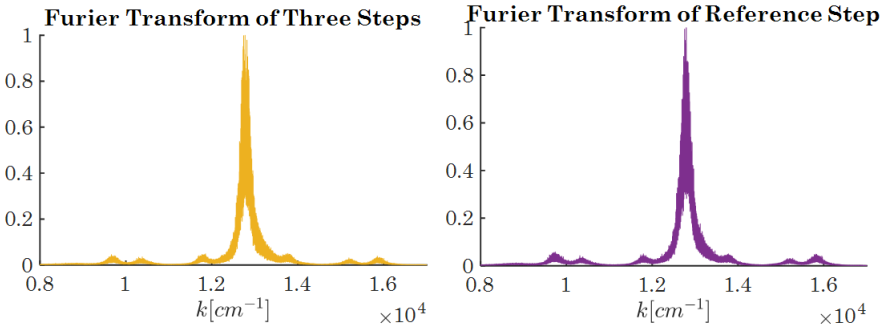

FIGURE G.9

Bibliography

[1] Eric O. Potma and X. Sunney Xie. Cars microscopy for biology and medicine. *Opt. Photon. News*, 15(11):40–45, Nov 2004. doi: 10.1364/OPN.15.11.000040. URL http://www.osa-opn.org/abstract.cfm?URI=opn-15-11-40.

[2] Bhawana Singh, Rekha Gautam, Srividya Kumar, Vinay BN Kumar, Upendra Nongthomba, Dipankar Nandi, Geetashree Mukherjee, Vani Santosh, Kumaravel Somasundaram, and Siva Umapathy. Application of vibrational microspectroscopy to biology and medicine. *Current Science*, 102(2):232–244, January 2012.

[3] Hoan T. Ngo, Elizabeth Freedman, Ren Abelard Odion, Pietro Strobbia, Agampodi Swarnapali De Silva Indrasekara, Priya Vohra, Steve M. Taylor, and Tuan Vo-Dinh. Direct detection of unamplified pathogen rna in blood lysate using an integrated lab-in-a- stick device and ultrabright sers nanorattles. *Scientific Reports*, 2018.

[4] Q. Josso. Culture-free antibiotic-susceptibility determination from single-bacterium raman spectra. *Scientific Reports*, 8(3957), 2018.

[5] H.W. Siesler. Fourier transform infrared (ftir) spectroscopy in polymer research. *Journal of Molecular Structure*, 59:15 – 37, 1980. ISSN 0022-2860. doi: https://doi.org/10.1016/0022-2860(80)85063-0. URL http://www.sciencedirect.com/science/article/pii/0022286080850630.

[6] B.H. Stuart. *Infrared Spectroscopy: Fundamentals and Applications*. Analytical Techniques in the Sciences (AnTs) *. Wiley, 2004. ISBN 9780470011133. URL https://books.google.co.il/books?id=xQVog8RrJKcC.

[7] Claus Jeppesen, Niels Asger Mortensen, and Anders Kristensen. The effect of ti and ito adhesion layers on gold split-ring resonators. *Applied Physics Letters*, 97 (26):263103, 2010. doi: 10.1063/1.3532096. URL https://doi.org/10.1063/1.3532096.

[8] Wei-Shun Chang, Fangfang Wen, Debadi Chakraborty, Man-Nung Su, Yue Zhang, Bo Shuang, Peter Nordlander, John E. Sader, Naomi J. Halas, and Stephan Link.

Tuning the acoustic frequency of a gold nanodisk through its adhesion layer. *Nature Communications*, 6(7022), 2015.

[9] Maxim A. Gorlach, Xiang Ni, Daria A. Smirnova, Dmitry Korobkin, Dmitry Zhirihin, Alexey P. Slobozhanyuk, Pavel A. Belov, Andrea Alù, and Alexander B. Khanikaev. Far-field probing of leaky topological states in all-dielectric metasurfaces. *Nature Communications*, 9(909), 2018.

[10] L. M. Zhang, Z. Q. Li, D. N. Basov, M. M. Fogler, Z. Hao, and M. C. Martin. Determination of the electronic structure of bilayer graphene from infrared spectroscopy. *Phys. Rev. B*, 78:235408, Dec 2008. doi: 10.1103/PhysRevB.78.235408. URL https://link.aps.org/doi/10.1103/PhysRevB.78.235408.

[11] J.F. James and R.S. Sternberg. *The Design of Optical Spectrometers: J.F. James and R.S. Sternberg*. Chapman and Hall, 1989. URL https://books.google.co.il/books?id=FlKTmgEACAAJ.

[12] D. Das and A. C. Wilson. Very long optical path-length from a compact multi-pass cell. *Applied Physics B*, 103(3):749–754, June 2011. ISSN 1432-0649. doi: 10.1007/s00340-010-4337-7. URL https://doi.org/10.1007/s00340-010-4337-7.

[13] E. Hecht. *Optics*. Addison-Wesley, 4th edition, 1998.

[14] Bahaa E A Saleh and Malvin Carl Teich. *Fundamentals of photonics; 2nd ed.* Wiley series in pure and applied optics. Wiley, New York, NY, 2007. URL https://cds.cern.ch/record/1084451.

[15] H. KOGELNIK and T. LI. Laser beams and resonators. *APPLIED OPTICS*, 5 (10), October 1966.

[16] Sumner P. Davis, Mark C. Abrams, and James W. Brault. *Fourier Transform Spectrometry*. Academic Press, San Diego, CA, 2001.

[17] Enrique J. Galvez. Gaussian beams, 2009. URL http://www.colgate.edu/portaldata/imagegallerywww/98c178dc-7e5b-4a04-b0a1-a73abf7f13d5/imagegallery/gaussian-beams.pdf.

[18] Athanasios Papoulis. *The Fourier Integral and its Applications*. McGraw-Hill, New York, 1962. ISBN 0070484473 9780070484474.

[19] D. Herriott, H. Kogelnik, and R. Kompfner. Off-axis paths in spherical mirror interferometers. *Appl. Opt.*, 3(4):523–526, Apr 1964. doi: 10.1364/AO.3.000523. URL http://ao.osa.org/abstract.cfm?URI=ao-3-4-523.

[20] Donald R. Herriott and Harry J. Schulte. Folded optical delay lines. *Appl. Opt.*, 4 (8):883–889, Aug 1965. doi: 10.1364/AO.4.000883. URL http://ao.osa.org/abstract.cfm?URI=ao-4-8-883.

[21] Takuma Doi, Kouji Toyoda, and Yoshihisa Tanimura. Effects of phase changes on reflection and their wavelength dependence in optical profilometry. *Appl. Opt.*, 36 (28):7157–7161, Oct 1997. doi: 10.1364/AO.36.007157. URL http://ao.osa.org/abstract.cfm?URI=ao-36-28-7157.

[22] N.W. Ashcroft and N.D. Mermin. *Solid State Physics*. Saunders College, Philadelphia, 1976.

[23] Robert W. Boyd, editor. *Nonlinear Optics (Second Edition)*. Academic Press, San Diego, second edition edition, 2003. doi: https://doi.org/10.1016/B978-012121682-5/50000-6.

[24] Franz Kärtner. Ultrafast optics. 2005. URL https://ocw.mit.edu/courses/electrical-engineering-and-computer-science/6-977-ultrafast-optics-spring-2005/lecture-notes/chapter10.pdf.

[25] Ellen J. Zeman and George C. Schatz. An accurate electromagnetic theory study of surface enhancement factors for silver, gold, copper, lithium, sodium, aluminum, gallium, indium, zinc, and cadmium. *The Journal of Physical Chemistry*, 91(3):634–643, 1987. doi: 10.1021/j100287a028. URL https://doi.org/10.1021/j100287a028.

[26] D. Kahaner, C.B. Moler, S. Nash, and G.E. Forsythe. *Numerical methods and software*. Prentice-Hall series in computational mathematics. Prentice Hall, 1989. URL https://books.google.co.il/books?id=jipEAQAAIAAJ.

[27] Matthew B Rhudy. Real time implementation of a military impulse classifier. January 2010. URL http://d-scholarship.pitt.edu/9773/.

[28] P. Stoica and R.L. Moses. *Spectral Analysis of Signals*. Pearson Prentice Hall, 2005. ISBN 9780131139565. URL https://books.google.co.il/books?id=h78ZAQAAIAAJ.

אוניברסיטת תל אביב

הפקולטה למדעים מדויקים ע"ש ריימונד ובברלי סאקלר

בית הספר לפיסיקה ואסטרונומיה

המחלקה לחומר מעובה

שילוב מהוד אופטי עם ספקטרומטר פורייה

חיבור זה מוגש כחלק מהדרישות לקבלת תואר 'מוסמך למדעים' באוניברסיטת תל אביב

על ידי

ערגה ליפשיץ

עבודה זו הוכנה בהנחיתו של

ד"ר חיים סוכובסקי

מאי 2018

Tel Aviv University

The Raymond and Beverly Sackler Faculty of Exact Sciences

School of Physics and Astronomy

Multipass FT-IR Spectrometer- Compact High Spectral Resolution

Thesis submitted in partial fulfillment of the requirements for M.Sc. at Tel-Aviv University

by

Erga Lifshitz

This work was carried out under the supervision of

Dr. Haim Suchowski

May 2018